Petrographic and Petrophysical Analysis of Decades-Old Iowa Portland Cement Concretes

Final Report
November 2019

IOWA STATE UNIVERSITY
Institute for Transportation

Sponsored by
Federal Highway Administration
Iowa Department of Transportation
(InTrans Project 18-624)

About the Institute for Transportation

The mission of the Institute for Transportation (InTrans) at Iowa State University is to develop and implement innovative methods, materials, and technologies for improving transportation efficiency, safety, reliability, and sustainability while improving the learning environment of students, faculty, and staff in transportation-related fields.

Iowa State University Nondiscrimination Statement

Iowa State University does not discriminate on the basis of race, color, age, ethnicity, religion, national origin, pregnancy, sexual orientation, gender identity, genetic information, sex, marital status, disability, or status as a US veteran. Inquiries regarding nondiscrimination policies may be directed to Office of Equal Opportunity, 3410 Beardshear Hall, 515 Morrill Road, Ames, Iowa 50011, telephone: 515-294-7612, hotline: 515-294-1222, email: eooffice@iastate.edu.

Disclaimer Notice

The contents of this report reflect the views of the authors, who are responsible for the facts and the accuracy of the information presented herein. The opinions, findings and conclusions expressed in this publication are those of the authors and not necessarily those of the sponsors.

The sponsors assume no liability for the contents or use of the information contained in this document. This report does not constitute a standard, specification, or regulation.

The sponsors do not endorse products or manufacturers. Trademarks or manufacturers' names appear in this report only because they are considered essential to the objective of the document.

Quality Assurance Statement

The Federal Highway Administration (FHWA) provides high-quality information to serve Government, industry, and the public in a manner that promotes public understanding. Standards and policies are used to ensure and maximize the quality, objectivity, utility, and integrity of its information. The FHWA periodically reviews quality issues and adjusts its programs and processes to ensure continuous quality improvement.

Iowa DOT Statements

Federal and state laws prohibit employment and/or public accommodation discrimination on the basis of age, color, creed, disability, gender identity, national origin, pregnancy, race, religion, sex, sexual orientation or veteran's status. If you believe you have been discriminated against, please contact the Iowa Civil Rights Commission at 800-457-4416 or the Iowa Department of Transportation affirmative action officer. If you need accommodations because of a disability to access the Iowa Department of Transportation's services, contact the agency's affirmative action officer at 800-262-0003.

The preparation of this report was financed in part through funds provided by the Iowa Department of Transportation through its "Second Revised Agreement for the Management of Research Conducted by Iowa State University for the Iowa Department of Transportation" and its amendments.

The opinions, findings, and conclusions expressed in this publication are those of the authors and not necessarily those of the Iowa Department of Transportation or the U.S. Department of Transportation Federal Highway Administration.

Technical Report Documentation Page

1. Report No.	2. Government Accession No.	3. Recipient's Catalog No.
InTrans Project 18-624		

4. Title and Subtitle	5. Report Date
Petrographic and Petrophysical Analysis of Decades-Old Iowa Portland Cement Concretes	November 2019
	6. Performing Organization Code

7. Author(s)	8. Performing Organization Report No.
Sergey Ishutov (orcid.org/0000-0002-3204-2171) and Franciszek "Franek" Hasiuk (orcid.org/0000-0002-6531-1710)	InTrans Project 18-624

9. Performing Organization Name and Address	10. Work Unit No. (TRAIS)
Geological and Atmospheric Sciences Iowa State University 253 Science Ames, IA 50011	**11. Contract or Grant No.**

12. Sponsoring Organization Name and Address		13. Type of Report and Period Covered
Iowa Department of Transportation 800 Lincoln Way Ames, IA 50010	Federal Highway Administration 1200 New Jersey Avenue, SE Washington, DC 20590	Final Report
		14. Sponsoring Agency Code 18-SPR0-008

15. Supplementary Notes

Visit https://intrans.iastate.edu/ for color pdfs of this and other research reports.

16. Abstract

In cold climates, the modern method for making durable portland cement concrete (PCC) pavement has been to entrain air in the paste. This method enables the formation of an air void network that permits the drainage of liquid water and accommodates pressure increases during freezing conditions. The Iowa Department of Transportation (DOT) has required air entrainment since the mid-1950s, and yet some pavements constructed before this period show little to no deterioration and remain in service. It remains uncertain which properties have allowed these pavements to last so long and if these properties can be used to increase the durability or reduce the cost of modern pavement designs.

This project aimed to study the evolution of pore networks in pre-1950 and post-1950 Iowa PCC pavements and interpret the deterioration of pavement aggregates. For this study, helium pycnometry was used to examine the total connected porosity of the air void network. Computed tomography (CT) scanning was used to cross-validate the helium porosity results as well as to calculate pore and aggregate size distributions. Mercury porosimetry was used to identify pore-throat size distributions and cross-validate the CT-measured values. Samples were also thin sectioned to characterize the physical state of coarse aggregate particles, determine their lithology, and identify their modes of deterioration. Finally, a script was developed for the coding platform, MATLAB, to provide similar metrics to the RapidAir 457 Air Void Analyzer but for CT images (e.g., porosity, pore size distribution, grain size distribution).

The initial hypothesis motivating this study was that pores forming around and inside deteriorating coarse aggregate particles in some unusually durable pre-air-entrainment PCC pavements are connected through pore throats in the paste serving to create effective air void networks. It was instead found through this study that the porosity of pavements showed strong correlation between decreasing porosity and increasing age. These results indicate that PCC porosity can be predicted from pavement age, at least in Iowa. Petrographic data suggest that this phenomenon is due to a reduction of pore space in the paste, with the reduction in paste porosity having more impact than the increase in porosity due to coarse and fine aggregate deterioration.

17. Key Words	18. Distribution Statement
air entrainment—air void networks—coarse aggregate deterioration—computed tomography—concrete pavement performance—freeze-thaw durability—helium pycnometry—Iowa concrete pavements—mercury porosimetry—pore networks	No restrictions.

19. Security Classification (of this report)	20. Security Classification (of this page)	21. No. of Pages	22. Price
Unclassified.	Unclassified.	121	NA

Form DOT F 1700.7 (8-72) **Reproduction of completed page authorized**

PETROGRAPHIC AND PETROPHYSICAL ANALYSIS OF DECADES-OLD IOWA PORTLAND CEMENT CONCRETES

Final Report
November 2019

Principal Investigator
Franciszek "Franek" Hasiuk, Associate Scientist
Kansas Geological Survey, University of Kansas
Lawrence, Kansas

Research Assistant
Sergey Ishutov

Authors
Sergey Ishutov and Franciszek "Franek" Hasiuk

Sponsored by
Iowa Department of Transportation

Preparation of this report was financed in part
through funds provided by the Iowa Department of Transportation
through its Research Management Agreement with the
Institute for Transportation
(InTrans Project 18-624)

A report from
Institute for Transportation
Iowa State University
2711 South Loop Drive, Suite 4700
Ames, IA 50010-8664
Phone: 515-294-8103 / Fax: 515-294-0467
www.intrans.iastate.edu

TABLE OF CONTENTS

LIST OF FIGURES

LIST OF TABLES

ACKNOWLEDGMENTS

The authors would like to thank the Iowa Department of Transportation (DOT) for sponsoring this research and the Federal Highway Administration (FHWA) for the state planning and research (SPR) funds used for this project (Federal SPR Part II, CFDA 20.205).

The authors also acknowledge the contributions of Andrea Haughton and Conner Adams (Iowa State University) in the areas of thin section description and automated analysis of petrographic images. The authors are also grateful for the guidance of Jacqueline Reber (Iowa State University) with respect to coding in MATLAB

EXECUTIVE SUMMARY

Problem Statement

It has remained uncertain which properties have allowed certain portland cement concrete (PCC) pavements predating Iowa's air entrainment requirements to last so long—and whether these properties can be used to increase the durability or reduce the cost of modern pavement designs.

Background

In cold climates, the modern method for making durable PCC pavement has been to entrain air in the paste. This enables formation of an air void network that accommodates pressure increases during freezing conditions.

The Iowa Department of Transportation (DOT) has required air entrainment since 1952, and yet some Iowa pavements constructed before this time show little to no deterioration and have remained in service decades beyond their originally designed service life.

Objectives

- Study the evolution of pore networks in pre-1950 and post-1950 Iowa PCC pavements
- Interpret the deterioration of pavement aggregates

Research Methodology

To characterize PCC pavement air void networks from both before and after air entrainment became common practice in Iowa, the research team performed an integrated petrographic and petrophysical analysis on samples from 10 pavements using nondestructive and destructive evaluation methods as follows:

- Helium pycnometry to examine the total connected porosity of the air void network
- Computed tomography (CT) scanning to cross-validate the helium pycnometry results as well as to calculate pore and aggregate size distributions
- Mercury porosimetry to identify pore-throat size distributions and cross-validate CT-measured values
- Thin sectioning to characterize the physical state of coarse aggregate particles, determine their lithology, and identify their modes of deterioration

Furthermore, a MATLAB script was developed to provide similar metrics to the RapidAir 457 Air Void Analyzer but for CT and thin section images (e.g., porosity, pore size distribution, grain size distribution).

Key Findings and Discussion

The initial hypothesis motivating this study was that pores forming around and inside deteriorating coarse aggregate particles in some unusually durable pre-air-entrainment PCC pavements are connected through pores in the paste that serve to create effective air void networks.

It was instead found through this study that the porosity of pavements showed strong correlation between decreasing porosity and increasing age. These results indicate that PCC porosity (i.e., the total percentage of air voids in a pavement) can be predicted from pavement age, at least in Iowa.

Petrographic data suggest that this phenomenon is due to a reduction of pore space in the paste, with the reduction in paste porosity having more impact than the increase in porosity due to coarse and fine aggregate deterioration.

The trend of porosity decreasing with age can be explained by the post-1950 samples' multiscale air void networks connected through three pore types:

- Micropores and fractures in the paste
- Pores formed due to coarse aggregate dissolution
- Intraparticle micropores formed due to fine aggregate dissolution

Thin section imaging and mercury porosimetry also indicated that the post-1950 pavements have smaller pore throats than the older samples.

The trend of porosity decreasing with age can likely also be explained by the pre-1950 samples' mineral growth visible in pores and reaction rims in the paste due to dissolution, which may reduce the connectivity of these older samples, decreasing their total connected porosity. Thin section imaging and mercury porosimetry indicate that pores in the older samples are mostly connected through fractures and microporosity in the paste.

While the pre-1950 and post-1950 samples have similar pore types, the deterioration mechanisms for the two groups are different. The pre-1950 samples have complete deterioration of the coarse aggregate, resulting in the formation of large pores that allow water drain through the pavement. Overall, the post-1950 samples have an interconnected air void network through deteriorating aggregate and fractures in the paste, and mineral precipitation may have reduced the connectivity of this pore network even further.

CT and helium analyses had good agreement with the RapidAir 457 Air Void Analyzer (ASTM C457) image analysis on total connected porosity. Unfortunately, although the MATLAB script used to extract PCC samples' three main phases (coarse aggregate, paste, and pores) from their respective CT images was tested with the thin section images in order to customize the

segmentation algorithms to these particular Iowa DOT samples, it remained challenging to identify clear boundaries between each phase.

The main issue was the presence of voxel values that could belong to more than one phase (e.g., fine aggregate can have the same voxel value as paste as indicated by the same grayscale value and the same color in the CT images, making it difficult to differentiate the fine aggregate from the paste).

Nevertheless, the CT images did show a clear trend across grain size and pore size distributions, where the coarse aggregate size distribution coincides with the pore size distribution for all samples. Specifically, the most abundant pore sizes were formed due to the dissolution of fine aggregate and therefore their dominant sizes are similar to that of the fine aggregate grains.

CT and thin section images also showed that pores in the older pavements that are due to the deterioration of fine aggregate and smaller coarse aggregate are largely similar in size, even if somewhat more irregularly shaped, compared to pores created in more modern pavements through the use of air-entraining agents. In addition, it was observed that open pores similar in size and shape to modern air entrainment pores were visible even in PCC manufactured pre-1950 (in addition to the larger pores observed to derive from the deterioration of coarse aggregate).

This suggests that either air-entraining agents were being used before they were widely acknowledged (a “secret sauce”) or that the fine aggregate has deteriorated to the extent that the resulting pores mimic the function of pores introduced via air-entraining agents.

Implementation Readiness and Benefits

This study found that some coarse aggregate pebbles are currently undergoing dissolution or have completely dissolved away, which suggests another way of creating an air void network in concrete: the inclusion of dissolvable materials. The solubility of these materials could be tailored to specific design goals.

In addition, this study suggests that—at least in Iowa—pavement age can be used as a strong predictor of PCC porosity.

Recommendations for Future Research

Future work should involve scanning-electron microscopy and geochemical analyses in order to identify the mineralogy of the dissolution rims in pores and paste to track how they can change over time in ways that are not related to fracturing.

Also, if the pore networks of PCC pavements mature over time, the researchers propose that it is necessary to monitor this evolution by regular sampling and petrographic analysis of pavements. By better understanding the evolution of the air void network and coarse aggregates in PCC,

pavement engineers and materials geologists will be able to make more informed decisions when designing pavements to ensure maximum longevity and durability and thus reduce the life-cycle costs of pavements to Iowa taxpayers.

INTRODUCTION

A governmental department of transportation (DOT) is typically tasked with the construction and maintenance of public roads for the security and economic well-being of its jurisdiction. Pavement has a finite lifespan determined by numerous factors both within and beyond the control of road builders, such as the quality of materials and construction, traffic volume and type, local topography, and local climate (Hanson 2009, Obla 2015, Poole and Sims 2016).

Climate is recognized as a major cause of portland cement concrete (PCC) deterioration in Iowa due to the numerous freeze-thaw cycles that the state experiences in a given winter (Hanson 2009). Therefore, resistance to freeze-thaw processes has been one of the most important parameters in designing Iowa highway pavements.

One common method to build freeze-thaw resistance into PCC pavements is to entrain air as the PCC is mixed (Gonnerman 1944, Powers 1954, Torrans and Ivey 1968). The resulting air voids are thought to better tolerate the accumulation of ice during the freezing season. While air entrainment in PCC started to be required in Iowa only in 1952 (Hanson 2009), it has since become the standard procedure for a PCC pavement to be approximately 8% ± 2% air voids by volume (Hanson 2007, 2009).

Evidence exists for intentional air entrainment in PCC as early as the 1840s in the UK (Idorn and Thaulow 1983, Blezard 1984). However, the modern practice of air entrainment stems from an observation in the 1930s in upstate New York that an air void system inhibited surface scaling of PCC (Torrans and Ivey 1968). This air void system had been unintentionally introduced into the paste when beef tallow was used as a grinding aid during cement production.

Beyond the practice of air entrainment, the parameters that can be modified during pavement formulation have multiplied since the early days of paving roads in Iowa approximately 100 years ago (Hanson 2007, 2009). These modifications are meant to prolong service life—since the construction of extremely long-lasting pavements has the potential to reduce the cost of road construction and maintenance—but modifications can also complicate the ability to predict pavement performance. A better understanding of the relevant material properties and associated chemical and physical processes can lead to the building of more long-lasting pavements.

Extant Pre-Air-Entrainment PCC Pavements

Interestingly, some pavements remain in service today from before air entrainment became standard practice. These decades-old pavements can potentially provide illuminating case studies into the factors promoting long PCC service life. While other case studies have examined old concretes (e.g., Hearn and Hooton 1992, Choi and Chan 2004, Hellebois et al. 2013), these have been for PCC structures (i.e., bridges) rather than pavements.

The first concrete pavement in the US was laid in Bellefontaine, Ohio, in 1891 (Davenport et al. 2014). A subsequent pavement laid in 1894 was still in use as of 2014; it used a two-layer system

where the base layer had 1½-inch coarse aggregate (CA), while the upper layer had ½-inch CA (Davenport et al. 2014). The PCC was mixed by hand, which seems to have entrained approximately 8% air voids by volume (Davenport et al. 2014). Recent coring showed the pavement had a strength of 5,000 psi (Snell and Snell 2002) to 8,000 psi (ASCE 2019).

The oldest PCC reported in the literature (a precast concrete wall made with limestone CA) is from Gravesend, Kent (UK). It was constructed in 1847 (Idorn and Thaulow 1983), though a later author contends it was more likely poured in the years 1850–51 (Blezard 1984). Idorn and Thaulow concluded, "It is possible to make concrete of several hundred years' durability." The CA was Kentish ragstone (Blezard 1984). This PCC showed evidence of air entrainment, although it has been suggested that this may be accidental from the fats used as release agents in the PCC molds (Blezard 1984). This PCC was designed with portland cement from Aspdin's Norfleet cement plant, which has been shown by electron microprobe chemical analysis to be similar in composition to modern portland cements (Rayment 1986).

In 1906, a PCC pavement (known by the trade name "granitoid") was laid down in Calumet, Michigan, which is now claimed to be the oldest PCC pavement in that state (Mailloux et al. 2008). Another author claims a rural road near Detroit in Wayne County, Michigan, was that state's first concrete pavement (Koster 1997). Four blocks of the Calumet pavement still exist (47.245277°N, 88.455785°W). A core was taken from the pavement in 2006 for petrographic examination (Mailloux et al. 2008). Records indicated that the PCC mix was composed of one part portland cement, three parts fine aggregate, and four parts CA that was then topped with a layer of mortar containing one part portland cement and 1½ parts granite screenings (Mailloux et al. 2008). The CA and fine aggregates came from local "trap rock" (i.e., Late Precambrian Keeweenawan basalt in the Calumet and Hecla Lode, a basalt pebble and cobble conglomerate) (Mailloux et al. 2008). The PCC's compressive strength was reported as 5,480 psi in 1956. In the 2006 study, petrographic examination found abundant entrapped air in the paste of the lower PCC layer but none in the surface mortar (Mailloux et al. 2008). The authors indicated that the lack of pore space in the surface mortar resembled modern ultra-high-performance concrete and that this surface layer had prevented the lower layer from deteriorating.

One of the oldest PCC pavements in Texas was poured in San Antonio in 1914 (Prusinski and Taubert 2013). This was also a "granitoid" pavement with a surface layer of mortar over a lower layer of PCC. The pavement runs from Dewey Place to Agarita Avenue for 0.7 miles (29.453731°N, 98.49735°W). The lower layer was one part portland cement, two parts fine aggregate, and three parts CA (pit-run gravel); the surface layer used trap rock from Knippa, Texas (Cement Council of Texas 2019).

Another well-documented surviving granitoid pavement exists in Grand Forks, North Dakota (Hoffbeck 1990). It was laid in 1911. No information was found concerning the makeup of its lower concrete layer (other than that the McNicol sand pit near Crookston, Minnesota, supplied the CA), but the wearing surface was two parts granite screenings (from the Upper Peninsula of Michigan) and one part cement.

The oldest concrete road in Minnesota is a granitoid pavement constructed in Duluth in 1909–10 (Kneer 2012). The CA in the surface course was gabbro (Kneer 2012). Its lower layer was not PCC but rather compressed CA (Kneer 2012). A granitoid pavement was also laid in 1909 (Hoffbeck 1990) in Grand Rapids, Minnesota. The earliest pavements in Illinois (1903) and Wisconsin (1909) were likely granitoids as well (Hoffbeck 1990).

The oldest concrete road in Missouri was a three-mile stretch from Independence to Kansas City. However, it is no longer extant; the oldest pavement in use today in Missouri was constructed in 1919–21 (Baughn 2009).

Nebraska's oldest pavement may be a section of the Lincoln Highway in Douglas County that was paved with one course in 1908 (Nebraska Concrete Paving Association 2019). The first significant concrete paving project was laying for about 6 miles on the Lincoln Highway (now US Highway 30) from Fremont to Ames, Nebraska, in Dodge County, in 1919 (Koster 1997). This project used pit-run gravel for CA.

The first annual report of the Iowa State Highway Commission (Holden et al. 1915) indicates that 1.37 miles of PCC were laid on the Great White Way and Blue Grass route (i.e., Columbus Junction-Fredonia Road). The report also indicated that on September 1, 1914, Engineer J. S. Morrison performed a survey for the grading of a concrete road near Eddyville. In addition, one mile of PCC was built in 1913 between Mason City and Clear Lake.

The second annual report of the Iowa State Highway Commission (Holden et al. 1916) indicated that two miles of PCC pavement were laid in 1915: one in Mason City (Mason City-Clear Lake Road) and one in Burlington. In the same report, they advised against using "soft native limestone," favoring "trap, quartzite, or granite."

Nondestructive Evaluation

Nondestructive evaluation of pavement specimens is becoming widely used to preserve samples that are costly to acquire and also as a prelude for numerical simulation of material and air void properties.

Helium pycnometry is a nondestructive method for obtaining the material density of a solid specimen using Boyle's Law (Boyle 1662). When the material density is combined with the bulk density of the specimen, effective porosity can be calculated (Vitton et al. 1999, Hedenblad 1997).

CT imaging has also been shown to be a reliable source of nondestructive evaluation of pavement materials. Previous work (Wong and Chau 2005) has shown that air voids are distinguishable in CT images in large specimens of PCC (10 x 20 cm) at a coarse resolution (250 x 250 x 3000 μm voxels). More recent work (Kim et al. 2012, Yun et al. 2012) has shown that the parameters of a PCC air void system (e.g., the specific surface) can be measured using higher resolution CT (11 x 11 x 9 μm). However, these studies have investigated only small samples

(1.0 x 1.2 cm), which may not be representative of the larger pore networks characterized in ASTM C457.

The combination of nondestructive methods (helium pycnometry and CT) and destructive methods (mercury porosimetry and thin sectioning) is promising as a means of characterizing the relative abundance of major components (paste, CA, fine aggregate, and air voids) as well as measuring their size distributions and textural characteristics (e.g., sorting or angularity).

In this study, an integrated workflow was used to characterize the lithology and/or mineralogy of CA and fine aggregates and to assess the extent of alteration of these materials as well as of the paste. In addition, a script was developed for the coding platform, MATLAB, to cross-validate the results of the CT measurements and destructive analyses of Iowa pavements constructed before and after the introduction of entrained air systems (1952).

METHODS

Characterization of pavement samples involved the integration of nondestructive (helium pycnometry and CT imagery) and destructive (mercury porosimetry and thin section petrography) analyses. Each method added unique data regarding the 3D distribution of the samples' air void networks and their connectivity as well as regarding their solid PCC components.

Nomenclature

In this study, "concrete" refers to hardened PCC, which is volumetrically and financially the most important pavement system to the Iowa DOT. Typically, over 99% of concrete is composed of coarse aggregate (CA) and fine aggregate (FA), cement paste, and air. As the cement paste and FA (grains <9.5 mm in diameter) have similar densities, these two components are treated as one material: "paste." The term "grains" refers to CA particles and "pores" to air voids.

The term "voxel" refers to the 3D elements that compose CT volumes. Voxel stands for "volume element" and is analogous to its two-dimensional (2D) "picture element" counterpart, namely the pixels that compose images. Voxels are cubic, but their size is usually described by the length of one side rather than their volume. Thus, a "59-µm voxel" in a three-dimensional CT dataset has a volume of $(59.2\ \mu m)^3$, which is equivalent to $2.07\times10^5\ \mu m^3$ or 0.02% of a cubic millimeter.

Sample Selection

The Iowa DOT collected 13 samples of PCC pavement, ten of which were used in this project (Tables 1 and 2). These samples had been in service from 10 years to over 100 years around Iowa. Two sample sizes were analyzed for each pavement (Figure 1): one puck-sized (4 in. diameter and 2 in. tall) and one plug-sized (drilled from the puck; 1 in. diameter and 2 in. tall). Both sample sizes were analyzed to establish what size of sample was needed to be representative of the whole cores' air void network. Mercury porosimetry was performed on only half of each plug due to the restricted capacity of the mercury porosimeter cell that limited samples to a diameter and length of up to only 1 in. each. Thin sections were cut from the other half of the plug.

Table 1. Samples' location and mix design

Year	County	District	Location*	Mix #	Proportion of Cement:Sand: Coarse	Cement	Basic Water	Water Max	Fine	Coarse	Interm.	Cement Content		Air Content (fraction)
												Barrels/yd^3	lbs/yd^3	
1914	Mahaska	5	Eddyville Cemetery Rd	—	Pit-run gravel	—	**	—	—	—	—	1.8	677	—
1921	Woodbury	3	Old US 20 E of Sioux City	—	Pit-run gravel	—	**	—	—	—	—	1.68	632	—
1929	Wapello	5	Old US 63 S of Ottumwa	2	1:1.946:2.929	—	—	—	—	—	—	1.71	643	—
1938	Monona	3	IA 175 MP 8.70 to 14.37	3	—	0.126	0.185	5.5 gal./bag	0.310	0.379	—	—	669	—
1946	Pocahontas	3	IA 15	3	—	0.126	0.185	5.5 gal./bag	0.310	0.379	—	—	669	—
1955	Greene	1	US 30 MP 94.59 to 99.10	C-3AX	—	0.114	0.154	5.25 gal./bag	0.312	0.381	—	—	602	0.04
1963	Marshall	1	US 30 MP 168.77 to 172.59	C-3	—	0.114	0.164	5.5 gal./bag	0.297	0.365	—	—	604	0.06
1976	Hamilton	1	US 20 MP 141.50 to 149.50	C-4WR	—	0.118	0.160	5.5 gal./bag	0.331	0.331	—	—	593	0.06
1980	Boone	1	IA 17 MP 21.63 to 32.76	Contr. Special Mix	—	0.098	0.500	0.550	0.337	0.337	—	—	517	0.06
1992	Story	1	US 30 MP 151.92 to 156.80 westbound	C-3WR-C15	—	0.108	0.146	0.489	0.309	0.377	—	—	571	0.06
1997	Linn	6	US 151 MP 33.60 to 36.68	C-3WR-C10	—	0.108	0.146	0.489	0.309	0.377	—	—	571	0.06
1999	Story	1	I-35 Station 155	—	—	—	—	—	—	—	—	—	—	—
2002	Jones	6	US 151 Monticello bypass	QMC	—	0.106	0.133	0.450	0.330	0.287	0.0826	—	553	0.07

*MP = milepost
*Only enough so that water will flush to surface with slight tamping

Table 2. Samples' coarse and fine aggregate information

Sample	Water:Cement Ratio (mean)	Coarse Aggregate Source	Fine Aggregate Source	Cement Source	Fly Ash Source	Fly Ash Type
1914-Mahaska	–	Eddyville Gravel	Eddyville	Unknown	None	None
1921-Woodbury	–	Correctionville Gravel	Correctionville	Marquette, Hawkeye, Northwestern	None	None
1929-Wapello	0.438	Dewey Limestone	Eddyville	Marquette, Atlas	None	None
1938-Monona	0.417	Correctionville Gravel	Correctionville	Ash Grove	None	None
1946-Pocahontas	0.448	Sioux Rapids Gravel	Sioux Rapids	Hawkeye	None	None
1955-Greene	0.467	Sprague Gravel	Ralston	Northwestern, Hawkeye	None	None
1963-Marshall	0.459	Ferguson Limestone	Clemons	Penn Dixie, Lehigh	None	None
1976-Hamilton	0.430	Moberly Limestone	Sturtz	Marquette, Lehigh	None	None
1980-Boone	0.520	Sturtz Gravel	Christensen	Penn Dixie, Lehigh	None	None
1992-Story	0.418	Ames Limestone	Christensen	Ash Grove	Chillicothe	15% Class C
1997-Linn	0.418	Bowser Dolomite	Unknown	Holcim Type IS (35%)	Chillicothe	35% GGBFS 10% Class C
1999-Story	–	Ames Mine	Unknown	Unknown	Council Bluffs #3	Not Available
2002-Jones	0.378	Behrends	Stephens	Lafarge IS (20%)	Louisa	Type I(SM), 15% Class C

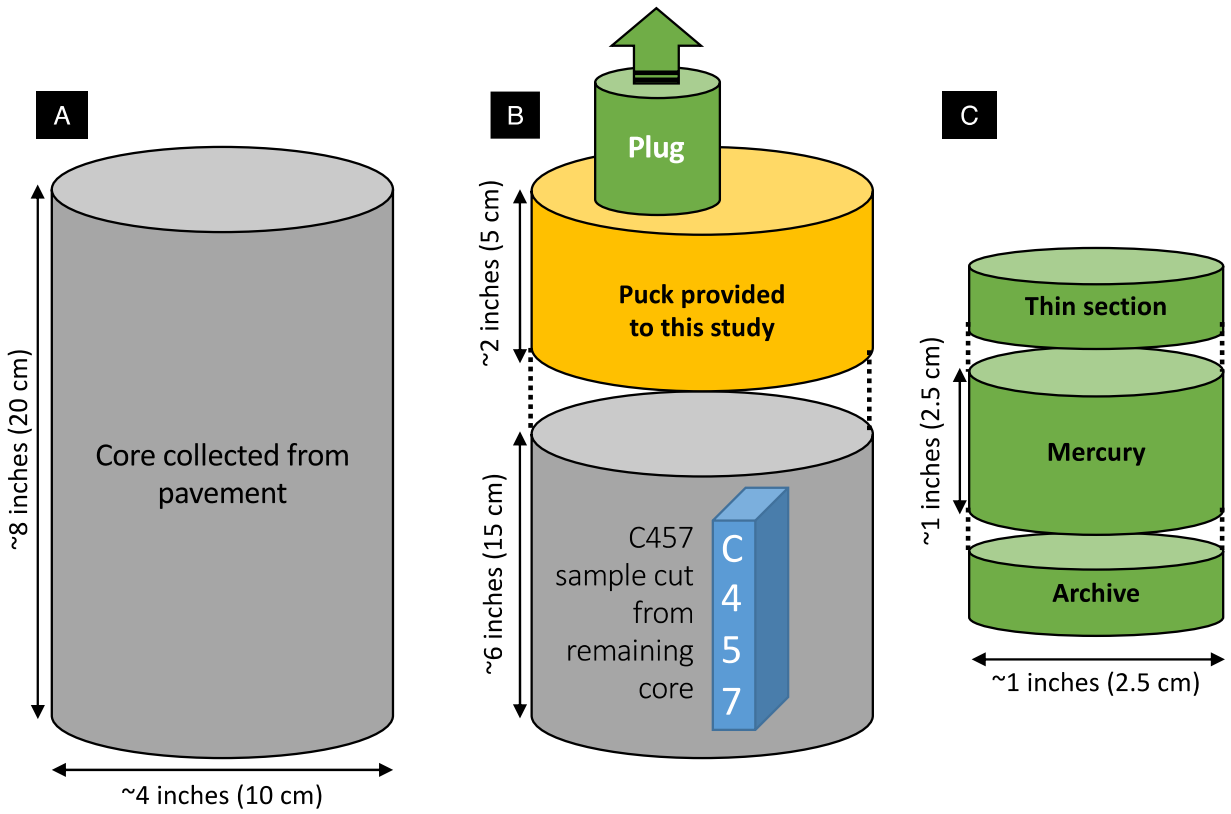

Figure 1. Schematic diagram showing orientation of original specimen (A) in relation to the 10-cm-diameter (4-inch) puck used for helium and CT porosity measurements (B) and 2.5-cm-diameter (1-inch) plug used for helium and CT porosity measurements as well as mercury porosimetry and thin sections (C)

Nondestructive Analyses

Two nondestructive analysis methods were used to characterize pavement samples in this study, namely helium pycnometry and computed tomography (CT).

Helium Pycnometry

Helium pycnometry was carried out at the Department of Geological and Atmospheric Sciences, Iowa State University, using a Micromeritics AccuPyc II 1340. This nondestructive analysis provided the total connected air void volume of each sample (both pucks and plugs). Samples were oven-dried for 24 hours at 80°C and allowed to return to room temperature (~23°C) in a desiccator. The bulk volume (or envelope volume) of each puck was calculated geometrically from its mean diameter and height, with each measured six times using digital calipers (Mitutoyo, precision ± 0.1 mm). Helium pycnometry uses Boyle's Law ($P_1V_1 = P_2V_2$) to measure the total grain volume of the sample. Equation 1 is then used to calculate sample porosity:

$$Porosity\ (\%) = \frac{Bulk\ Volume - Grain\ Volume}{Bulk\ Volume} = \frac{Pore\ Volume}{Bulk\ Volume} \quad \textbf{(1)}$$

Helium was used as a measurement gas because it is inert, so no reaction could occur with the sample materials. In addition, its small molecular size enables penetration into the smallest pores that might be present in the sample. One caveat of this method is that only pores connected to the external surface of the sample (i.e., effective pores) are measured. Isolated pores are unmeasured and if present would result in a larger total (or "true") porosity.

Computed Tomography (CT)

Computed tomography (CT) is another nondestructive analytical method that can provide additional useful information about the air void network in PCC, namely measurement of the isolated pores that helium pycnometry may miss. CT data were acquired at two locations: pucks were scanned at the University of Texas Center for Computed Tomography (UTCT); plugs were scanned at the Iowa State University Center for Nondestructive Evaluation. CT images of pucks were acquired with the following parameters: fan-beam X-rays, 80 kV voltage; sample bulk volume of 2000x1000x2000 voxels, 59.2 µm per voxel; and 720 raw images converted to 4-GB volume. CT images of plugs were acquired with the following parameters: fan-beam X-rays, 80 kV voltage; sample bulk volume of 1000x800x1000 voxels, 35 µm per voxel; and 360 raw images converted to 3-GB volume. Reconstruction of CT volumes from individual images and removal of CT acquisition artifacts (e.g., bad pixels and beam hardening) were also performed at UTCT. Two brass filters were used to reduce beam-hardening artifacts. The CT images were used to map and calculate 3D features (e.g., fractures and pore connectivity) and as source data for statistical computations (Figure 2).

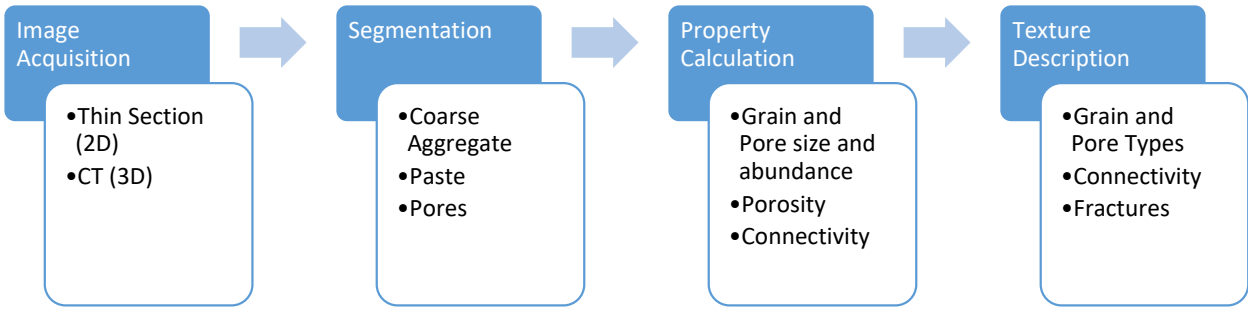

Figure 2. Workflow for analysis of CT and thin section images

MATLAB was used to calculate 2D and 3D components in both puck and plug CT images. The first step in CT volume analysis involved segmentation via MATLAB of the voxel values in each CT image into three phases: pores, paste, and CA. Voxels were assigned to each phase based on a grayscale histogram containing the values from 0 to 255. Each phase represented a peak in the histogram, so the boundary between phases was selected between the peaks. Then the relative abundance of each PCC phase was calculated (e.g., the relative abundance of pores is porosity). The pore phase was used to measure porosity, pore-throat sizes, and pore connectivity.

Aggregate phase measurements included aggregate volume and aggregate sizes. Paste volume was also calculated from the total number of voxels in the paste phase.

Helium-porosity measurements can provide valuable calibration information when attempting to segment a CT volume into relevant phases. Helium porosity should be larger than CT porosity because the diameter of a helium atom (0.06 nm) allows it to reach pores much smaller than the resolution of CT (in this study, voxels with edge lengths of 59.2 or 35 μm). The only caveat is that helium porosity will not intrude pores that are unconnected to the surface of the sample. Though such pores can be seen via CT if they are above the image resolution, the drawback of CT is that it cannot be used to discern pores below the voxel size. These pores may represent either natural pores in CA or pores formed by the entrainment of air in paste. The goal of segmenting was not to "match" helium porosity but rather to use the helium porosity as a general guide to the maximum porosity present in the sample. CT resolution limitations, especially when applied to materials with fine-scale pores (like PCC), mean that CT characteristically returns less porosity than a helium measurement.

Destructive Analyses

Due to limitations in the cell size of the mercury porosimeter (23 mm in diameter and 30 mm in length), the full size of pucks and plugs could not be analyzed with mercury porosimetry. As mentioned earlier, mercury porosimetry was therefore performed on one half of the plug and thin sections were cut from the remaining half.

Mercury Porosimetry

Mercury porosimetry was used to characterize the size heterogeneity of the connections between air voids in the size range of 6 nm to 500 μm, a crucial range for water percolation. The pore-throat size distribution was measured with a Quantachrome PoreMaster 33 from 0 to 33 kpsi (207 MPa), a 140° contact angle, a 480 dynes/cm^2 interfacial tension, and a 23°C mercury temperature at the Department of Geological and Atmospheric Sciences, Iowa State University.

Thin Section Analysis

Thin section images were acquired using an Olympus BX53 petrographic microscope with transmitted light at the Department of Geological and Atmospheric Sciences, Iowa State University. This thin section analysis was twofold. First, thin sections provide higher resolution imaging of PCC samples as well as allow better discrimination of minerals and sample texture (e.g., fractures), enabling detailed visual description of image components. Photomosaics of each thin section were created as well as higher-resolution snapshots of specific features. Second, the photomosaics were used to compute porosity using the MATLAB code described above. The resulting "thin section porosity" could then be compared to the porosity derived from helium and CT measurement.

RapidAir 457 Air Void Analyzer Analysis

The RapidAir 457 Air Void Analyzer ("RapidAir") measures the air void content as well as one-dimensional (linear) shape statistics for the air-void system in paste as represented by a two-dimensional polished slab of PCC that is ~16 $in.^2$ (4 in. x 4 in.; 100 mm x 100 mm). The slab is painted black and then barium sulfate powder is pressed into the slab to highlight the pores. Finally, any pores in the CA are colored black with an indelible marker.

RESULTS

Helium Porosity and Chloride Permeability

Porosity was measured in four different ways for the samples in this study. First, helium gas was used to measure each sample's total pore volume for pores connected to the sample's exterior surface. This method can analyze pores down to the size of a helium atom (0.06 nm), but it cannot analyze pores that are completely isolated from the external surface. Second, CT was used to measure total pore volume. Due to the penetrative nature of CT, it can measure isolated pores, but it is limited to the resolution of the CT detector (60 µm for pucks and 35 µm for plugs). Thin section and rapid-air techniques are image-based like CT, but they analyze a two-dimensional specimen rather than CT's three dimensions. Thin sections offer higher resolution but work on a smaller specimen (a 1-in. diameter circle) compared to RapidAir (able to analyze a square with 4-in. sides).

Both C457 porosity and helium porosity show strong negative correlations with the age of a sample ($R^2 \approx 0.8$ for both methods), as seen in Table 3 for pucks, Table 4 for plugs and Figure 3A for pucks only (since plugs show similar behavior). These correlations can be described using the following models:

$$\Phi_{C457} = -0.10 \times Age + 10.53, \; R^2 = 0.80 \quad \textbf{(2)}$$

$$\Phi_{helium} = -0.09 \times Age + 15.58, \; R^2 = 0.81 \quad \textbf{(3)}$$

where Φ_{C457} is porosity measured by ASTM C457 (in percentage points), Φ_{helium} is porosity measured by helium (in percentage points), and age is in years. Helium porosity is consistently higher than C457 porosity by approximately five percentage points. When cross-plotted (Figure 3B), C457 porosity and helium porosity's strongly correlation ($R^2 = 0.70$) can be described using the following models:

$$\Phi_{457} = 0.93 \times \Phi_{helium} - 4.78, \; R^2 = 0.70 \quad \textbf{(4)}$$

$$\Phi_{helium} = 0.76 \times \Phi_{C457} + 6.82, \; R^2 = 0.70 \quad \textbf{(5)}$$

As shown in Figure 3B, C457 and helium porosity are most divergent at lower porosities (older samples).

Table 3. PCC puck property measurements*

Sample	Diameter (Mean) (mm)	Height (Mean) (mm)	Bulk Volume (cm^3)	Mass (g)	Bulk Density (g/cm^3)	Helium Grain Volume (cm^3)	Helium Grain Volume (1s SD, cm^3)	Helium Grain Density (g/cm^3)	Helium Porosity (%BV)
1914-Mahaska	101.40	52.43	423.34	970.5	2.29	389.40	0.6055	2.49	8.0
1921-Woodbury	101.03	50.42	404.20	950.4	2.35	381.30	0.9874	2.49	5.7
1929-Wapello	101.37	51.45	415.18	984.4	2.37	387.85	0.6726	2.54	6.6
1938-Monona	100.66	51.70	411.48	959.9	2.33	375.12	0.8855	2.56	8.8
1946-Pocahontas	100.43	51.98	411.71	977.8	2.37	379.21	0.5679	2.58	7.9
1955-Greene	100.35	51.33	406.03	922.6	2.27	359.53	0.6874	2.57	11.5
1963-Marshall	100.51	51.85	411.34	946.0	2.30	367.5	0.4422	2.57	10.7
1976-Hamilton	100.30	51.58	407.57	895.9	2.20	351.61	0.5879	2.55	13.7
1980-Boone	100.35	51.12	404.31	891.8	2.21	352.88	0.3141	2.53	12.7
1992-Story	100.35	51.04	403.68	877.8	2.17	347.37	0.5651	2.53	14.0
1997-Linn	101.42	51.76	418.09	894.8	2.14	344.52	0.3596	2.60	17.6
1999-Story	100.24	51.84	409.11	912.8	2.23	354.70	0.1884	2.57	13.3
2002-Jones	100.92	51.40	411.13	942.1	2.29	360.56	0.9810	2.61	12.3

*Bulk volume was calculated geometrically from caliper measurements. Helium porosity was measured using a helium pycnometer.

Table 4. PCC plug property measurements*

Sample	Diameter (Mean) (mm)	Height (Mean) (mm)	Bulk Volume (cm^3)	Mass (g)	Bulk Density (g/cm^3)	Helium Grain Volume (cm^3)	(1s SD, cm^3)	Helium Grain Density (g/cm^3)	Helium Porosity (%BV)
1914-Mahaska-1	25.28	48.03	24.11	55.307	2.29	21.4644		2.5767	10.96
1914-Mahaska-2	25.37	45.98	23.24	53.328	2.29	20.8155		2.5619	10.45
1914-Mahaska-3	25.38	46.38	23.46	53.898	2.30	20.9334		2.5747	10.79
1921-Woodbury-1	25.31	44.78	22.53	52.012	2.31	20.1777		2.5777	10.44
1921-Woodbury-2	25.26	44.91	22.51	53.12	2.36	20.4100		2.6027	9.31
1921-Woodbury-3	25.30	45.31	22.78	51.889	2.28	20.2845		2.5580	10.95
1929-Wapello	25.52	52.05	26.63	61.699	2.32	23.927		2.5786	10.15
1938-Monona	25.50	51.78	26.44	58.869	2.23	22.909		2.5697	13.34
1946-Pocahontas	25.61	52.30	26.93	62.117	2.31	23.5190		2.6411	12.68
1955-Greene	25.68	51.27	26.56	58.459	2.20	22.606		2.5860	14.90
1963-Marshall	25.63	51.62	26.64	59.624	2.24	22.506		2.6492	15.51
1976-Hamilton	25.50	51.50	26.31	56.513	2.15	21.886		2.5822	16.81
1980-Boone	25.56	51.27	26.31	61.211	2.33	22.843		2.6796	13.19
1992-Story									
1997-Linn	25.54	51.84	26.57	55.952	2.11	21.51		2.6012	19.03
1999-Story-1	25.25	46.96	23.51	52.367	2.23	20.145		2.5995	14.33
1999-Story-2	25.29	46.07	23.14	50.752	2.19	19.622		2.5865	15.21
1999-Story-3	25.27	48.17	24.16	54.89	2.27	20.878		2.6290	13.58
2002-Jones	25.60	51.55	26.54	59.2054	2.23	22.129		2.6755	16.62

*Bulk volume was calculated geometrically from caliper measurements. Helium porosity was measured using a helium pycnometer.

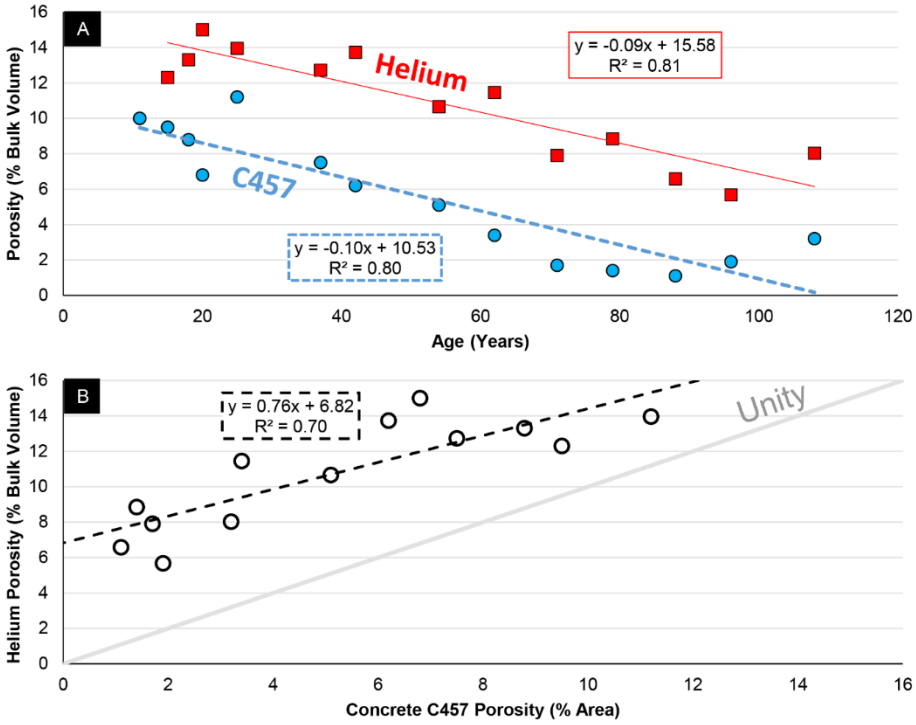

Figure 3. A) Comparison of puck porosity measured by ASTM C457 image analysis vs. helium porosity and B) the correlation between pucks' C457 porosity and helium porosity

Rapid chloride permeability data (Table 5) for the same samples show a convex pattern with respect to age (Figure 4A), with both the oldest and youngest samples returning the lowest permeability and intermediate-age samples (40–70 years) giving the highest values (~3000 coulombs).

In sedimentary rocks, porosity and permeability are often correlated (Lucia, 2007) because as porosity increases so generally do the sizes of the permeability-controlling pore throats that connect the pores. When the rapid chloride permeability of the samples is plotted against helium porosity (Figure 4B), a convex correlation similar to the permeability-age plot is observed: low permeability is correlated with both the highest and lowest helium porosity. Maximum rapid chloride permeability is associated with intermediate porosity (12–14%).

Table 5. Engineering test data including air void data from image analysis (ASTM C457) and rapid chloride permeability data (AASHTO T 277)

Sample	Air in Mortar (%Area)	Air in Concrete (%Area)	Diameter (Mean) (microns)	Specific Surface (mm^{-1})	Spacing Factor (mm)	Spacing Factor (in)	Rapid Chloride Permeability Test 1 (Coulombs)	Rapid Chloride Permeability Test 2 (Coulombs)	Rapid Chloride Permeability Mean (Coulombs)
1914-Mahaska	5.2%	3.2%	0.032	30.7	0.17	0.007	478	816	647
1921-Woodbury	3.2%	1.9%	0.019	18.1	0.38	0.015	546	223	385
1929-Wapello	1.9%	1.1%	0.011	32.0	0.27	0.011	796	611	704
1938-Monona	2.3%	1.4%	0.014	16.5	0.49	0.019	1277	1215	1246
1946-Pocahontas	2.8%	1.7%	0.017	21.4	0.38	0.015	1453	1089	1271
1955-Greene	5.0%	3.4%	0.034	21.6	0.25	0.010	2283	3296	2790
1963-Marshall	8.3%	5.1%	0.051	34.0	0.12	0.005	1483	2361	1922
1976-Hamilton	10.1%	6.2%	0.062	29.7	0.12	0.005	1742	1285	1514
1980-Boone	12.1%	7.5%	0.075	23.5	0.10	0.004	2877	3553	3215
1992-Story	17.7%	11.2%	0.112	26.0	0.09	0.004	702	1279	991
1997-Linn	11.0%	6.8%	0.068	25.3	0.13	0.005	262	252	257
1999-Story	8.8%	8.8%	0.088	58.1	0.05	0.002			
2002-Jones	14.4%	9.5%	0.095	25.1	0.11	0.004	1173	938	1056
2004-Jefferson	14.4%	9.5%	0.095	25.1	0.11	0.004	880	734	807
2006-Fremont	15.2%	10.0%	0.100	24.9	0.10	0.004	437	342	390

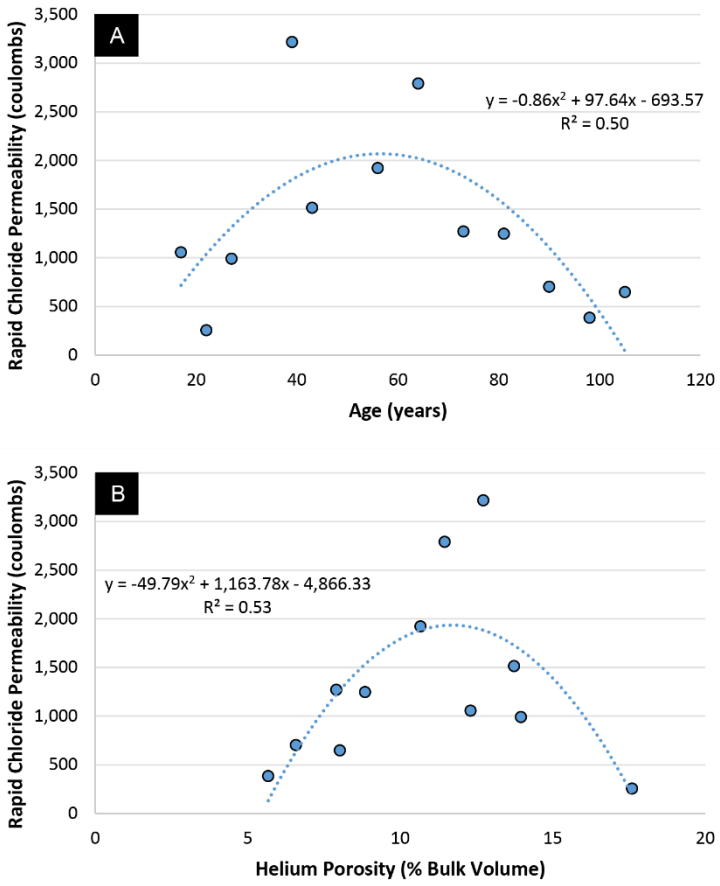

Figure 4. Rapid chloride permeability relative to A) age and B) helium porosity

Mercury Porosimetry and Pore-Throat Size Distribution

In porous media, permeability is thought to be controlled by the connections between pores (i.e., pore throats). Mercury intrusion porosimetry was used to determine the size distribution of pore throats (SDPT) for all samples (Figures 5 and 6). These SDPTs all show multiple modes across the full range of intrusion (50 µm to 6 nm), suggesting that the PCC samples analyzed contain complex pore networks. For pre-air-entrainment samples (Figure 5), SDPT modes occurred at ~15 nm, ~55 nm, ~350 nm, and ~6 µm. Post-air-entrainment samples showed modes at ~15 nm, ~65 nm, ~200 nm, and ~10 µm. Most intrusion occurred at pore-throat sizes smaller than 1 µm.

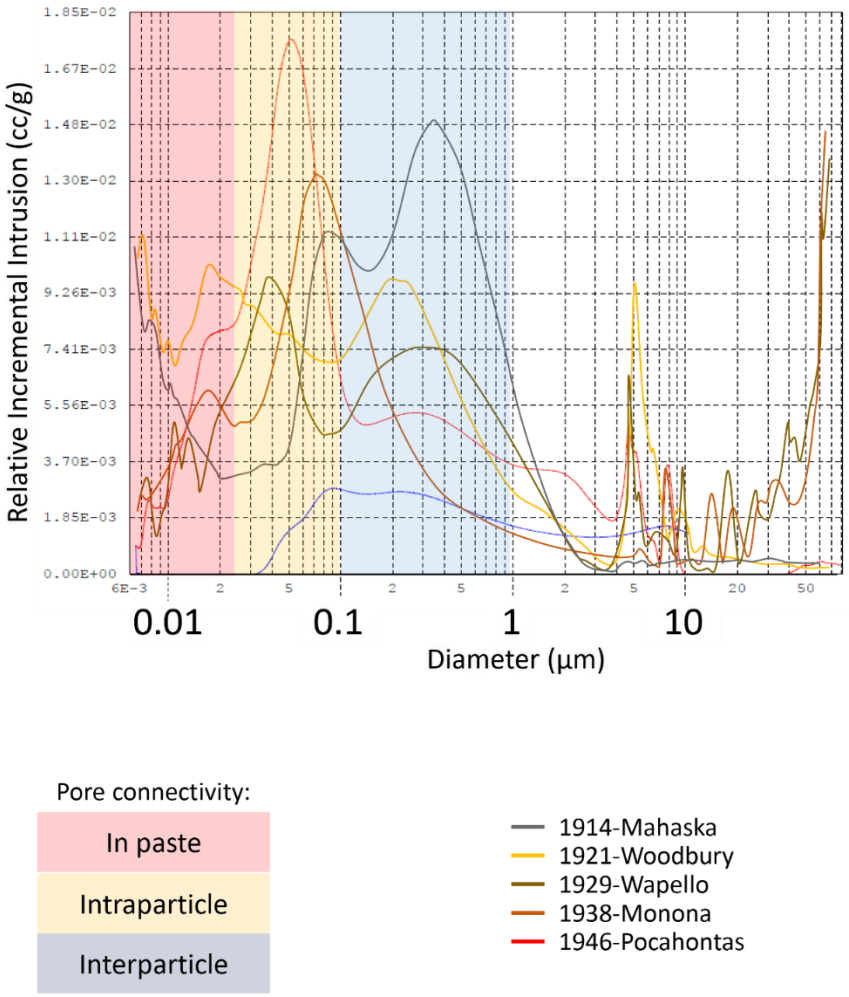

Figure 5. Pore-throat size distribution calculated from mercury porosimetry for pavements constructed *before* 1950

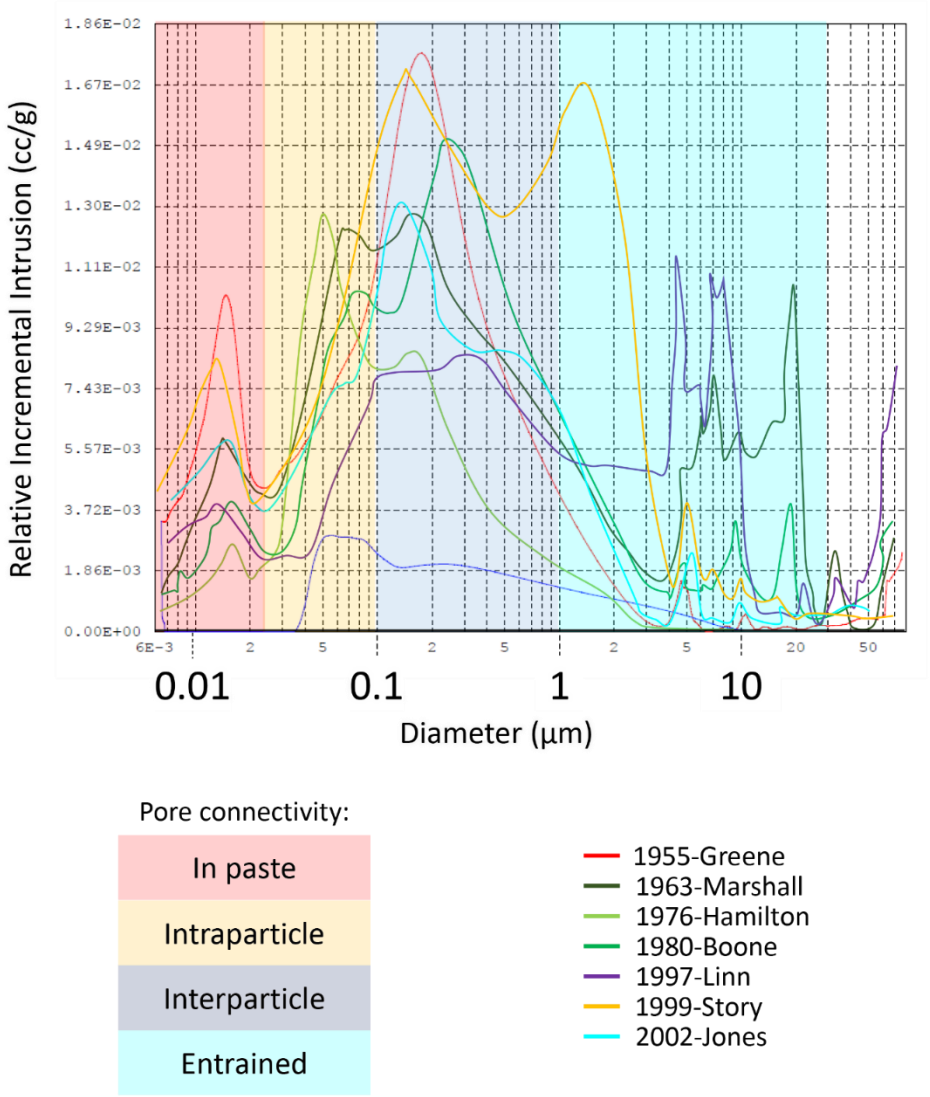

Figure 6. Pore-throat size distribution calculated from mercury porosimetry for pavements constructed *after* 1950

CT Imaging

Three samples (1914-Mahaska, 1921-Woodbury, and 1999-Story) were used to develop a methodology for segmenting the CT images into their component phases: paste, pores, and CA (Table 6). Components identified in natural-light images of the sample surface (Figure 7i, noting approximate core plug locations) were followed into the subsurface via grayscale CT images (Figure 7ii, taken a few mm below the surface shown in Figure 7i). This method enabled segmentation of the puck's grayscale CT volume shown in Figure 7ii into its three major phases (Figure 7iii).

Table 6. CT pore/grain metrics for pucks

				Pores		Grains	
Sample	Total Porosity (%BV)	Grain Volume (%BV)	Paste Volume (%BV)	Diameter (Mean) (µm)	Area (Mean) (µm^2)	Diameter (Mean) (µm)	Area (Mean) (µm^2)
1914-Mahaska	7.70	72.30	20.00	204	1.10E+08	276	2.21E+10
1921-Woodbury	5.47	81.36	13.17	110	1.21E+07	105	3.99E+08
1929-Wapello	4.40	59.33	36.27	28	7.85E+08	106	2.21E+08
1938-Monona	6.02	70.05	23.93	32	8.97E+07	69	1.02E+10
1946-Pocahontas	6.80	69.83	23.37	73	1.43E+07	93	1.58E+08
1955-Greene	9.05	72.18	18.77	110	2.30E+07	102	2.14E+08
1963-Marshall	8.61	56.37	35.02	79	1.64E+08	99	1.85E+08
1976-Hamilton	9.31	61.06	29.63	49	1.01E+09	116	2.65E+09
1980-Boone	11.38	55.57	33.05	59	1.25E+07	124	2.78E+09
1992-Story	11.08	63.09	25.83	39	9.57E+09	84	1.46E+09
1997-Linn	14.72	69.00	16.28	114	1.07E+07	131	2.92E+08
1999-Story	11.70	65.00	23.30	100	5.55E+07	107	1.17E+08
2002-Jones	9.54	62.50	27.96	40	9.88E+07	105	1.95E+08

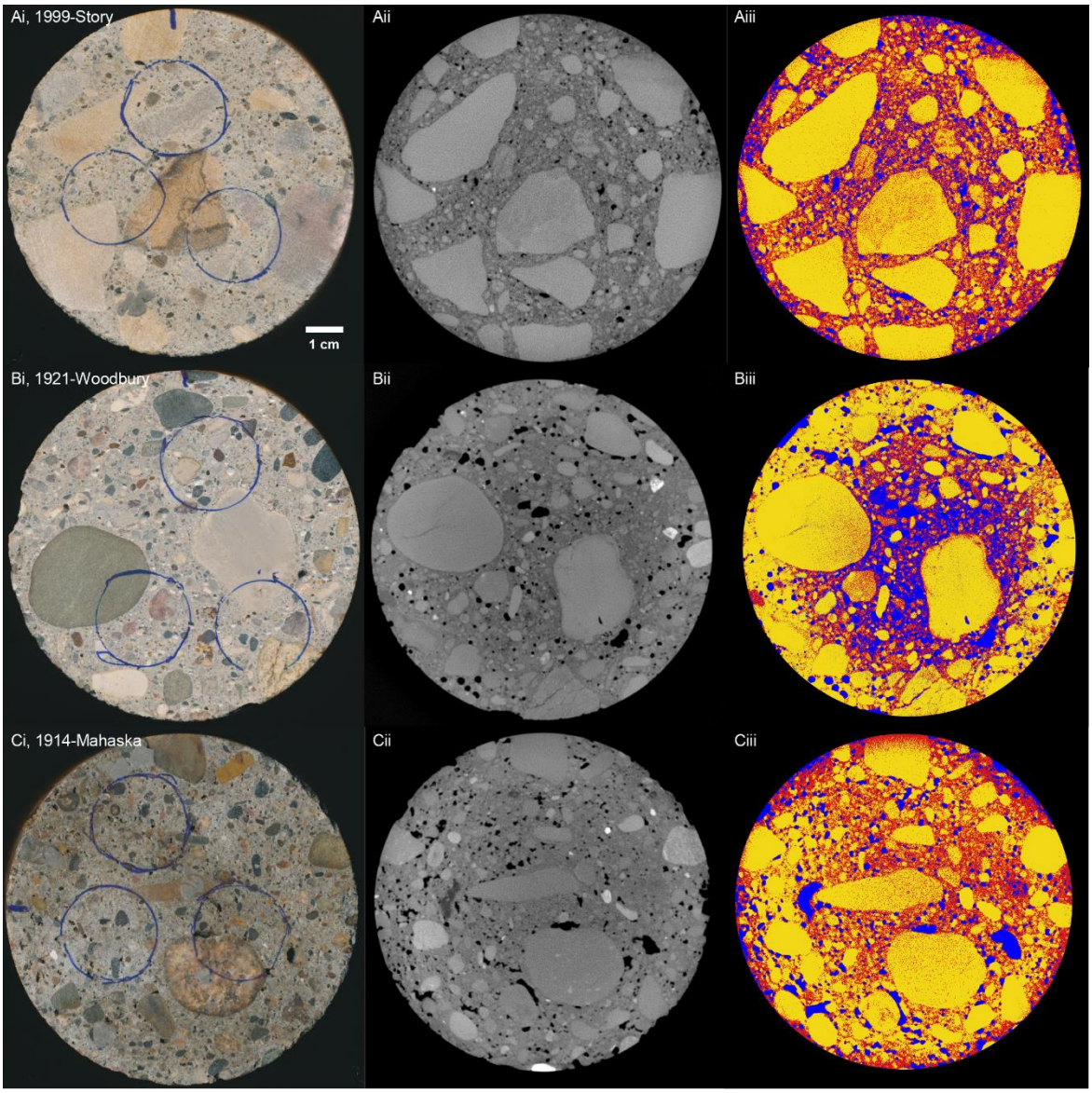

Figure 7. Comparison of natural-light photograph (i), CT tomograph (ii), and CT tomographs (iii) segmented into grains (yellow), pores (blue), and paste (red) for three samples: 1999-Story (A), 1921-Woodbury (B), and 1914-Mahaska (C)

1914-Mahaska has the clearest distinction among the three components compared to the other PCC samples (Figure 8A-C). This is evidenced by the tri-modal CT intensity histogram (Figure 8D) with grains at ~115, paste at ~45, and pores at ~32 grayscale values (No intensities for this sample were recorded below ~10 or above ~150.) Compared to 1999-Story and 1921-Woodbury, 1914-Mahaska peaks are narrower and rise to higher total counts and the sample's pore and paste peaks are also better separated.

Pores in 1914-Mahaska are large and found throughout the sample (Figure 8A). (The abundance of pores around the edges of the sample is likely related to plucking during sample acquisition as well as to ring artifacts introduced during CT scanning.) Some pores have approximately the same size and shape as grains. Paste is present between grains and pores as well as has some domains with the size and shape of grains (Figure 8B). Grains are rounded and have a wide size distribution (Figure 8C). They are composed of multiple lithologies, as observed by the difference in CT intensities within individual grains (suggesting mostly igneous or metamorphic textures) or between grains (suggesting different lithologies).

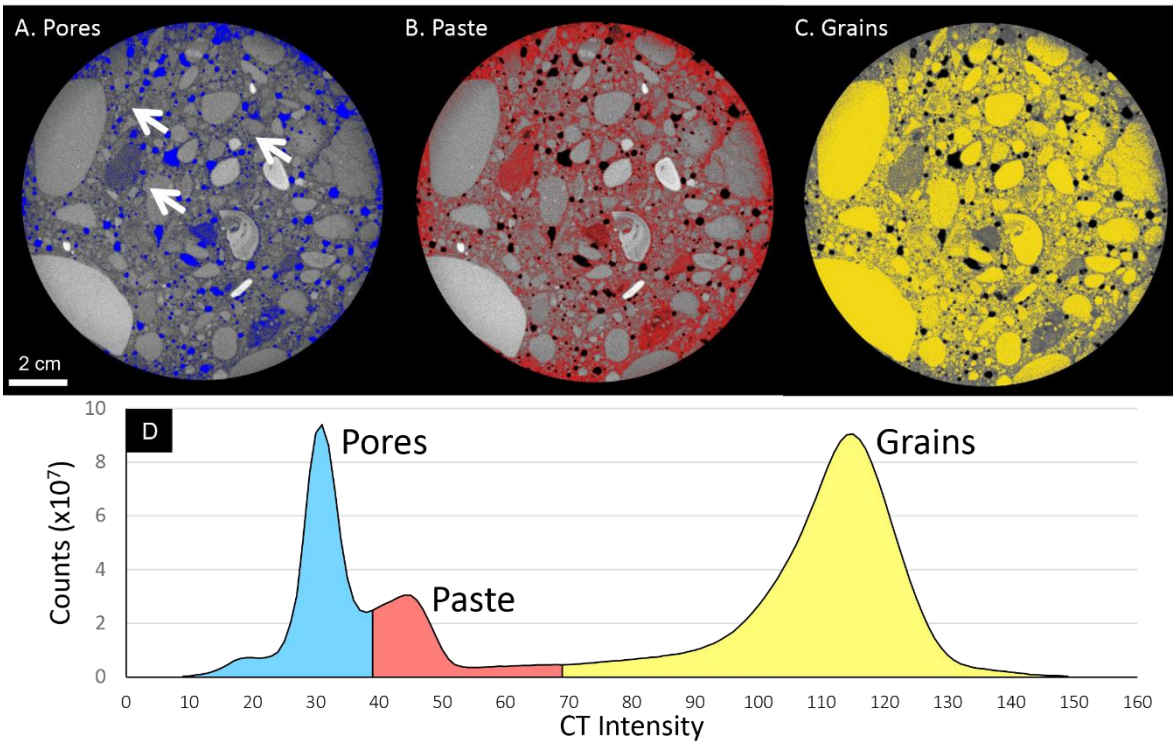

Figure 8. Segmented CT tomographs for 1914-Mahaska showing pores (A), paste (B), and grains (C) compared to the histogram of intensities for the entire puck with regions distinguished according to phase (D)

In 1921-Woodbury, the distinction between pores and grains is as large as in 1914-Mahaska, but the distinction between pores and paste is diminished (Figure 9D). (No intensities for this sample were recorded below ~10 or above ~160.) Compared to 1999-Story, 1921-Woodbury peaks are narrower and rise to higher total counts. Also, in contrast to 1999-Story, the pore and paste peaks for 1921-Woodbury are separated by a "valley" of low counts.

Pores in 1921-Woodbury are large and evenly distributed throughout the sample (Figure 9A). The abundance of pores around the edges of the sample again is likely an artifact of data acquisition. Some pores have approximately the same size and shape as fine aggregate, which is especially noticeable for three pores (Figure 9A). Paste (Figure 9B) occurs only between grains and pores, unlike for 1914-Mahaska in which some paste retained the size and shape of CA grains. Grains (Figure 9C) are rounded and have a more uniform size distribution than in 1914-Mahaska. This textural variation suggests lithological variation between grains and within grains (Figure 9C).

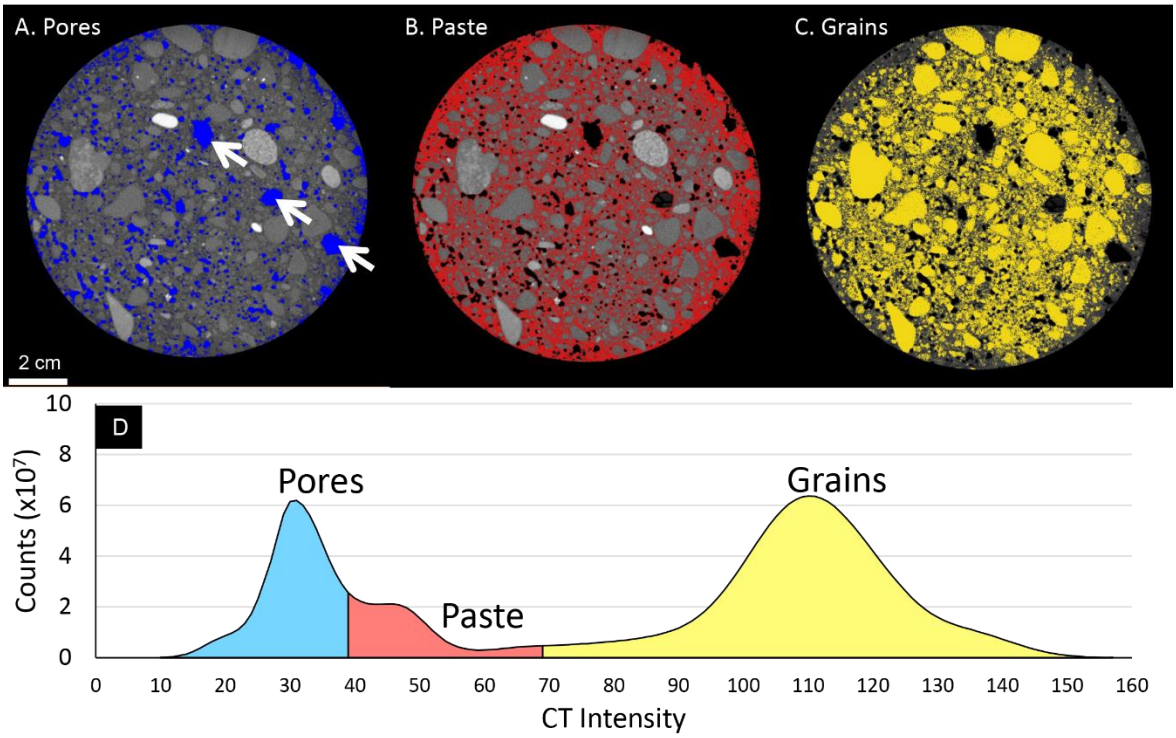

Figure 9. Segmented CT tomographs for 1921-Woodbury showing pores (A), paste (B), and grains (C) compared to the histogram of intensities for the entire puck with regions distinguished according to phase (D)

In 1999-Story, the distinction between pores and paste is even less (Figure 10) and its grains are angular (representative of crushed rock). (No intensities for this sample were recorded below ~10 or above ~145.)

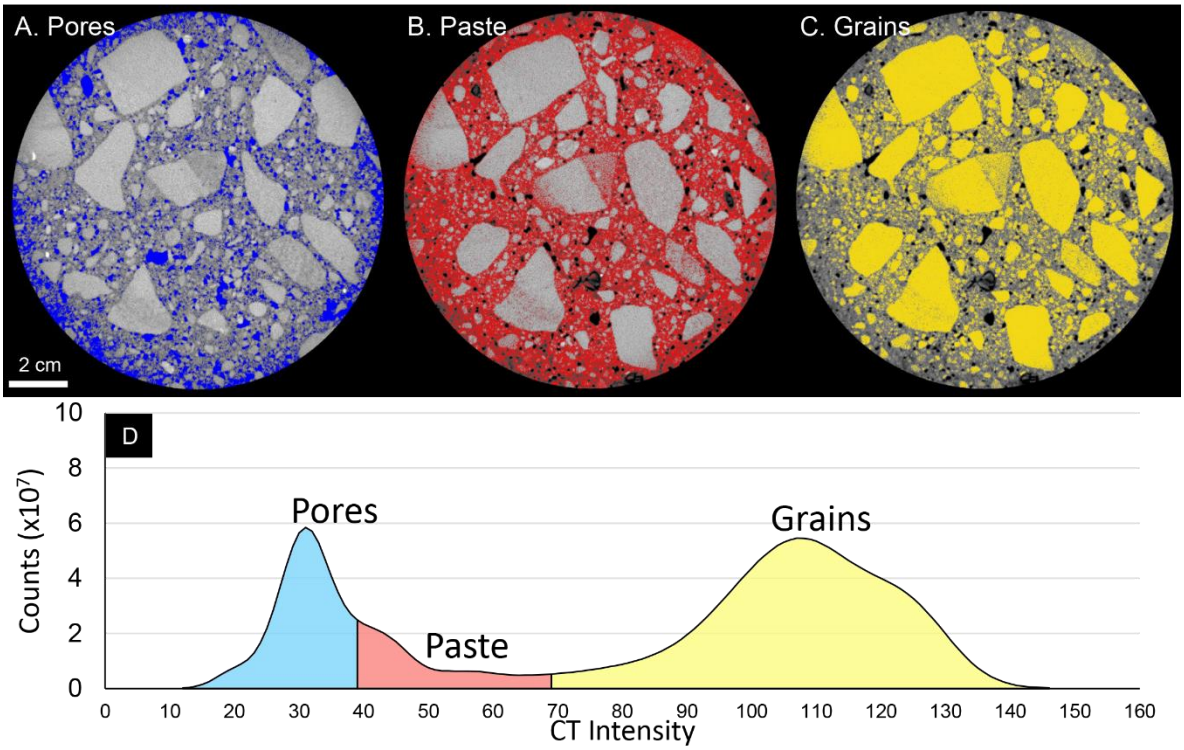

Figure 10. Segmented CT tomographs for 1999-Story showing pores (A), paste (B), and grains (C) compared to the histogram of intensities for the entire puck with regions distinguished according to phase (D)

The character of the CT intensity distribution for 1999-Story is between that of 1914-Mahaska and 1921-Woodbury (Figure 11). 1999-Story shows minor lithological variation between grains and within grains but not as high as in 1914-Mahaska or 1921-Woodbury.

Through the process of segmentation (the classification of voxels into discrete categories or phases), CT analysis identified the amount and geometric properties of the components in the three preliminary PCC samples (Figure 2). The intensity histogram peaks for pores is at the same intensity for all samples (Figure 11) because this peak represents the density of air (that across samples indeed should be identical). The peaks for paste and grains (Figure 11) are more variable in their shape and location, representing differences in the bulk density of the materials used in constructing the concrete. For example, 1999-Story was constructed using crushed limestone (density ≈ 2.71 g/cm^3), whereas the older samples were constructed with "pit-run" river gravels composed mostly of igneous and metamorphic rocks (density > 3 g/cm^3). The peaks for grains in the 1914-Mahaska and 1921-Woodbury are shifted to higher intensities representing these higher densities (Figure 11).

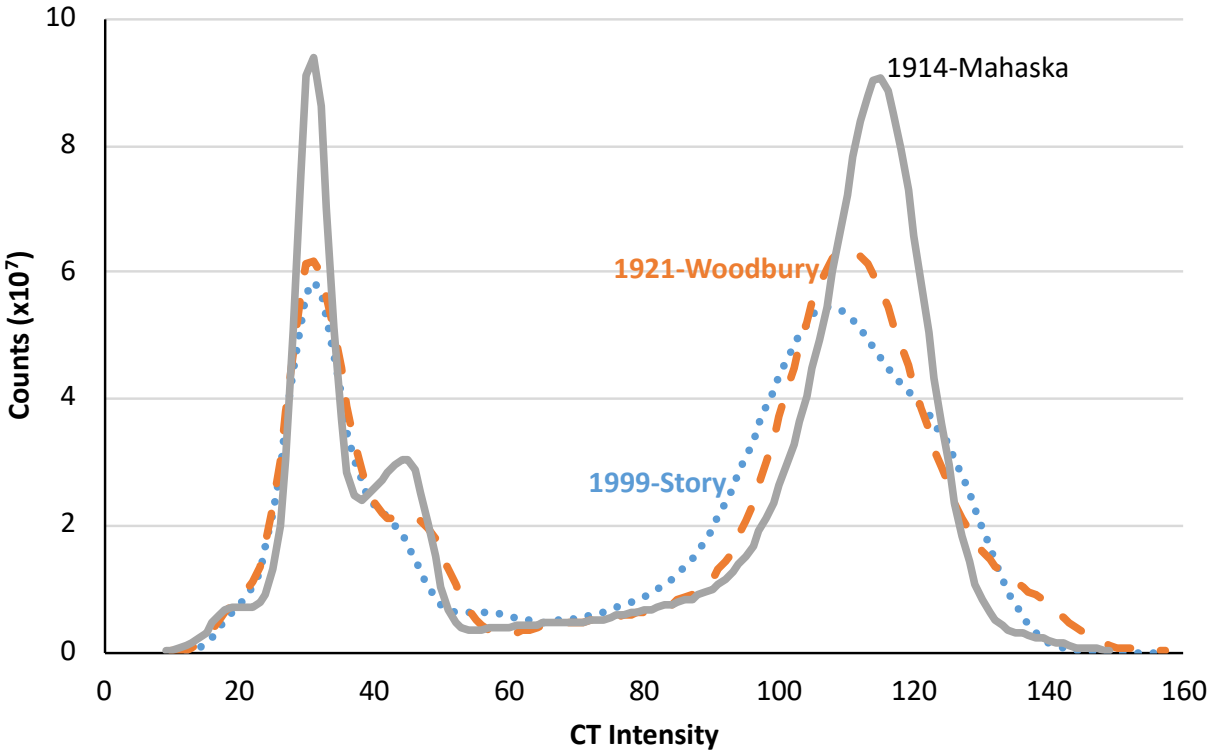

Figure 11. Comparison plot of CT intensity histograms

CT Pore Types

Ideally, all voxels can be assigned to one of the three major components of hardened concrete: grains, paste, or pores. Unfortunately, two factors conspired against such a purely tri-modal histogram of CT intensities. First, the cement paste had a relatively uniform size distribution (due to its rather homogenous composition of di- and tri-calc-silicates), but grains (coarse and fine aggregates) and pores (air voids) occurred across a range of sizes. Second, CT scanning produced a raster of voxels to represent the sample, with each voxel holding the average CT intensity of the material in that space. For space inside a CA pebble with zero porosity and uniform mineralogy, an average CT intensity will accurately represent that space. However, if that voxel spans a grain/pore/paste boundary, its intensity will be an average of the CT intensities from the three phases based on their relative abundance. This averaging can also yield "speckled" data if that voxel spans an area within a grain that contains density variations (e.g., those caused by metamorphic fabrics or by pores within CA particles). This phenomenon is called the "partial volume effect."

Two dominant pore types were identified in the CT data from the three test samples. The first dominant pore type is called "circumgranular" (A in Figures 12–14) because these pores often occur around the margins of CA grains. This pore type likely forms when air is entrained during PCC mixing. In some cases, circumgranular pores have coalesced into larger irregular pores (labeled C in Figures 12–13), likely through dissolution.

The second dominant pore type was of the same size and shape as CA or fine aggregate grains (B in Figures 12–14). This pore type has likely formed due to the dissolution of CA or fine aggregate grains. These are called "moldic" pores because they are molds left behind by the dissolution of grains and perhaps some paste. In some cases, portions of the dissolving grain are still visible on the CT data or through visual examination (labeled D in Figures 12–14).

These two dominant pore types show a clear difference in abundances between the modern control pavement (1999-Story) and the two older pavements (1914-Mahaska and 1921-Woodbury). In 1999-Story, circumgranular pores (A) are abundant, while they are rare in 1914-Mahaska and 1921-Woodbury. Conversely, moldic pores (B) are rare in 1999-Story, while they are abundant in 1914-Mahaska and 1921-Woodbury.

This finding suggests that the pore system in the youngest sample (1999-Story) is dominated by pores formed by the entrainment of air during PCC construction (E). On the other hand, the pore systems of the two older samples are dominated by pores created through the dissolution of aggregate (D).

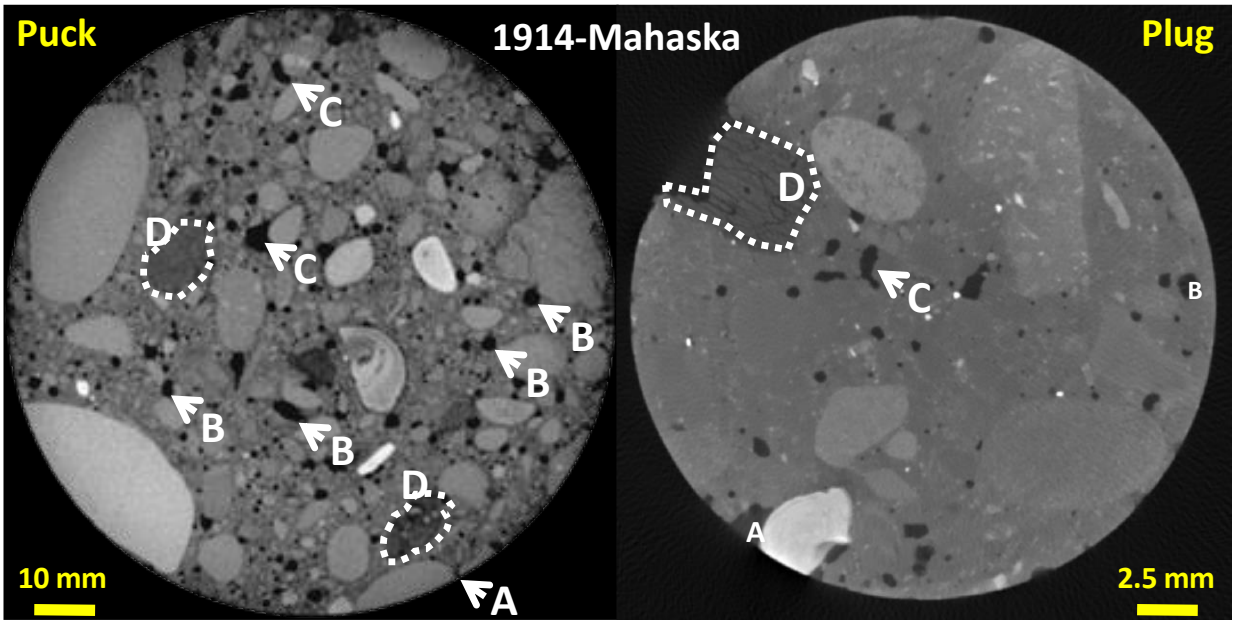

Representative puck (59.2 microns/voxel) and plug (35 microns/voxel) CT images for 1914-Mahaska—Images show the pores are interparticle, often grouped around coarse aggregate grains ("circumgranular" pores, A). There are rare occurrences of what appear to be pores formed by the dissolution of grains ("moldic" pores, B) and some coalesce into larger, irregularly shaped pores (C). In addition, some large coarse aggregate grains are deteriorating (D).

Figure 12. Representative puck and plug CT images for 1914-Mahaska

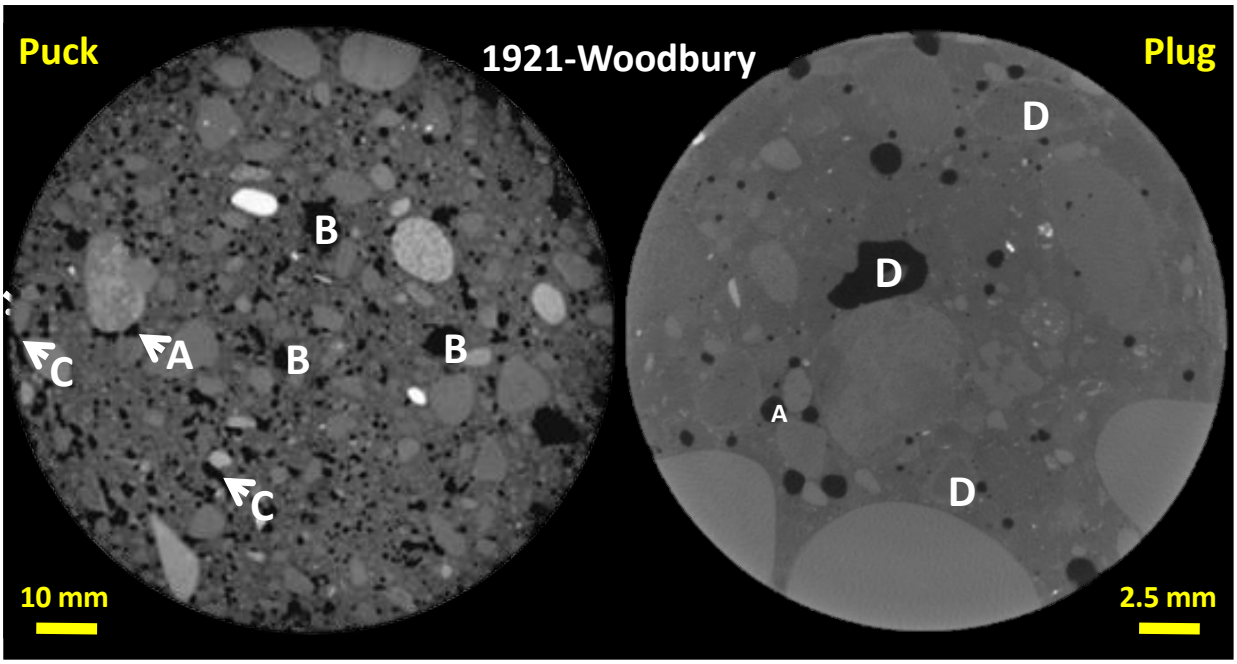

Representative puck (59.2 microns/voxel) and plug (35 microns/voxel) CT images for 1921-Woodbury—Images show the pores are interparticle, often grouped around coarse aggregate grains ("circumgranular" pores, A). There are rare occurrences of what appear to be pores formed by the dissolution of grains ("moldic" pores, B) and some coalesce into larger, irregularly shaped pores (C). In addition, some large coarse aggregate grains are deteriorating (D).

Figure 13. Representative puck and plug CT images for 1921-Woodbury

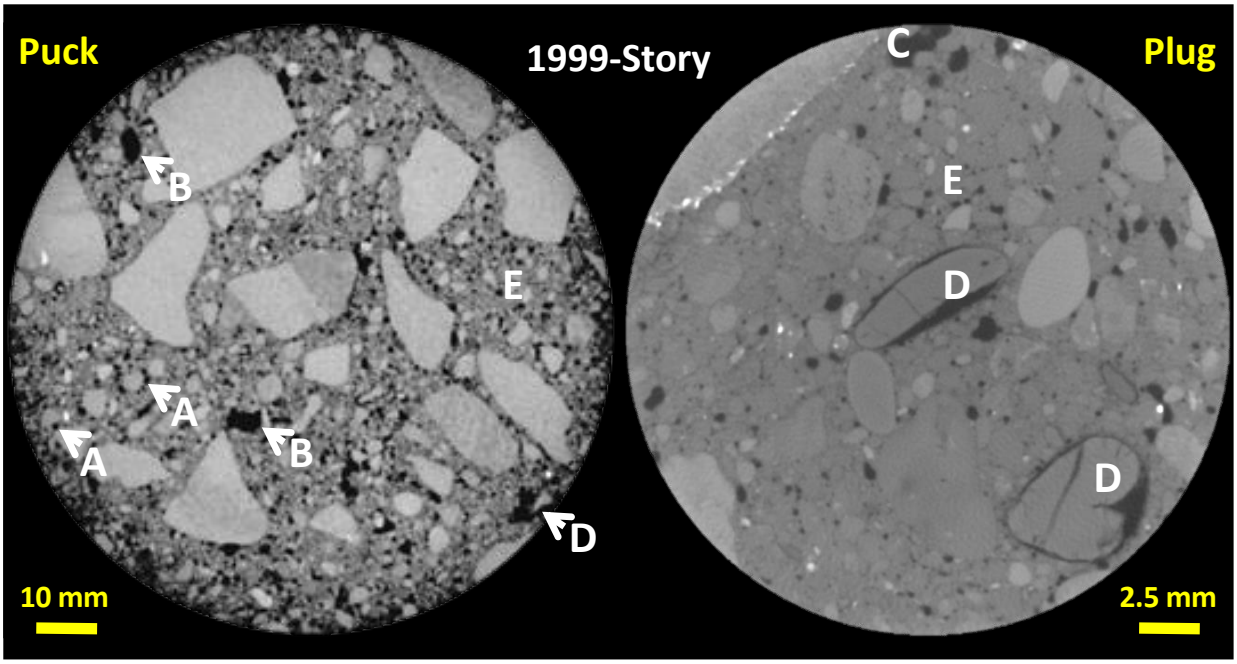

Representative puck (59.2 microns/voxel) and plug (35 microns/voxel) CT images for 1999-Story—Images show the pores are interparticle, often grouped around coarse aggregate grains ("circumgranular" pores, A). There are rare occurrences of what appear to be pores formed by the dissolution of grains ("moldic" pores, B). Some large coarse aggregate grains are deteriorating (D). Entrained air pores (E) are also visible.

Figure 14. Representative puck and plug CT images for 1999-Story

This preliminary analysis of pore types from our first three test samples' CT data allowed us to classify the air void networks according to whether they were naturally formed (for three pre-1950 samples) or entrained (for seven post-1950samples). All samples' CT images for pucks were scanned at 59.2 microns/voxel and for plugs at 35 microns/voxel.

1929-Wapello

1929-Wapello's CT images of puck and plug (Figure 15) show abundant circumgranular pores that coalesce (C) into an air void network. Moldic pores (B) are less evident and likely formed due to FA dissolution. Coalescent pores (C) caused by the deterioration (D) of the FA and paste are common.

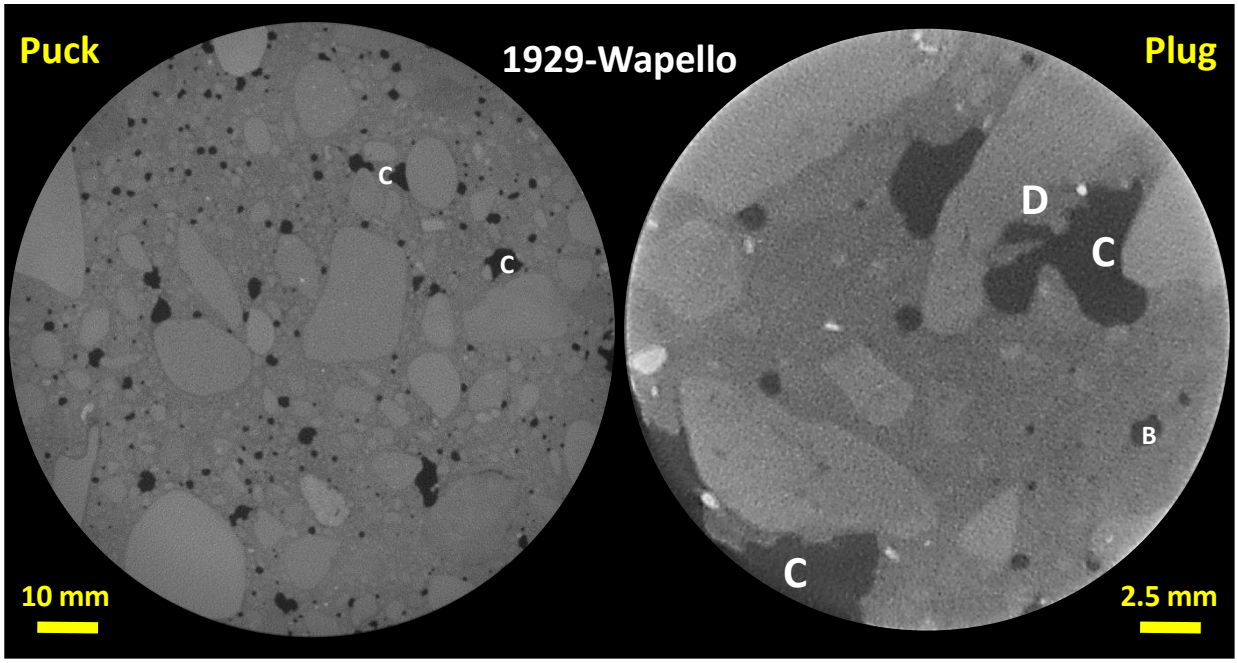

*Representative puck (59.2 microns/voxel) and plug (35 microns/voxel) CT images for pavement constructed **before 1950**:1929-Wapello—Images show abundant moldic (B) and coalescent (C) pores are evident. Little deterioration of coarse aggregate (D) is evident.*

Figure 15. Representative puck and plug CT images for pavement constructed *before* 1950: 1929-Wapello

It is difficult to identify the parent mineralogy/lithology of the FA in 1929-Wapello because of the advanced nature of its deterioration. Carbonate material is one possibility; however, the basic nature of the PCC microenvironments suggests it is an igneous or metamorphic lithology that is more soluble under such conditions. Deterioration (D) of the CA was rare but present. The sample's coarse subrounded limestone aggregate had similar CT intensities throughout and did not have visible lithological differences. The FA was visible, but sometimes individual grains were below CT resolution, causing variation in CT intensity.

1938-Monona

The CT images of 1938-Monona's puck and plug (Figure 16) show large, but less abundant, circumgranular pores (A) that coalesce (C) into a larger void network compared to 1929-Wapello. The CA grains in 1938-Monona have similar CT intensities, suggesting uniform mineralogy; however, its FA shows different CT intensities. Both its CA and FA are subangular. The plug image of 1938-Monona also shows the remnant of a grain in the pore formed due to deterioration (D). Fracturing (F) of some CA grains is present.

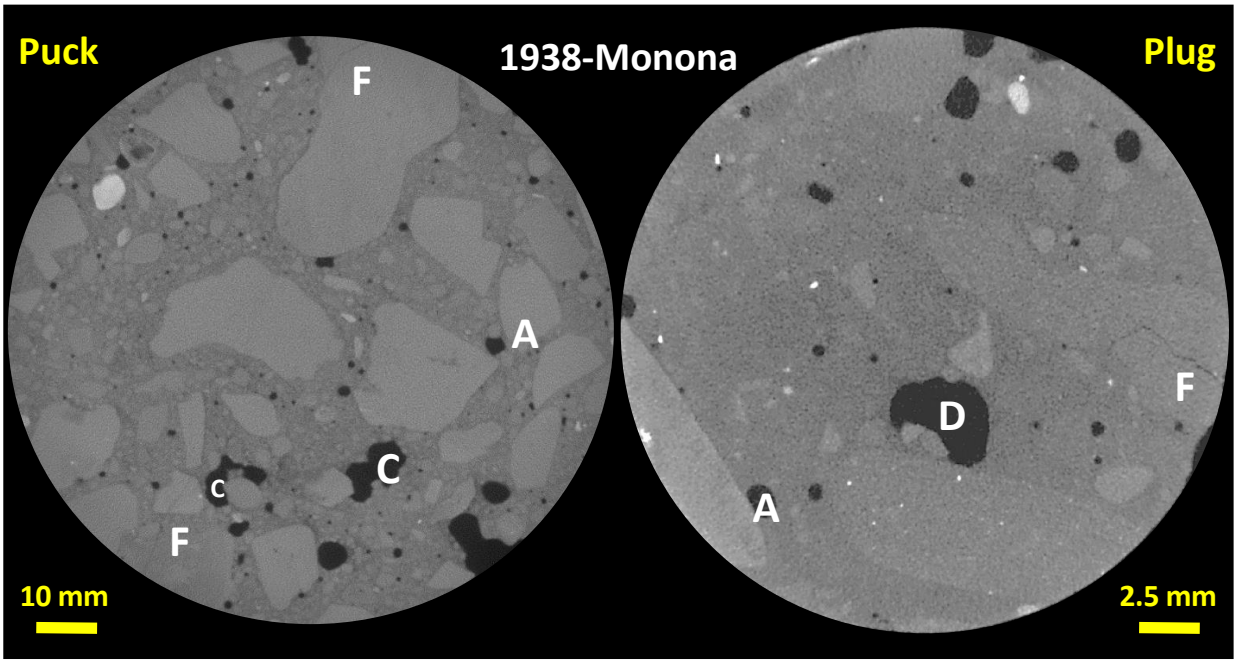

*Representative puck (59.2 microns/voxel) and plug (35 microns/voxel) CT images for pavement constructed **before 1950**: 1938-Monona.—Images show abundant circumgranular pores (A) are evident and some coalesce into larger irregularly shaped pores (C). Little deterioration of coarse aggregate (D) is evident, but some fracturing is present (F).*

Figure 16. Representative puck and plug CT images for pavement constructed *before* 1950: 1938-Monona

1946-Pocahontas

1946-Pocahontas puck and plug images (Figure 17) also show abundant circumgranular pores (A) formed around CA. These pores coalesce (C) into a larger pore network through the paste. Moldic pores are also evident.

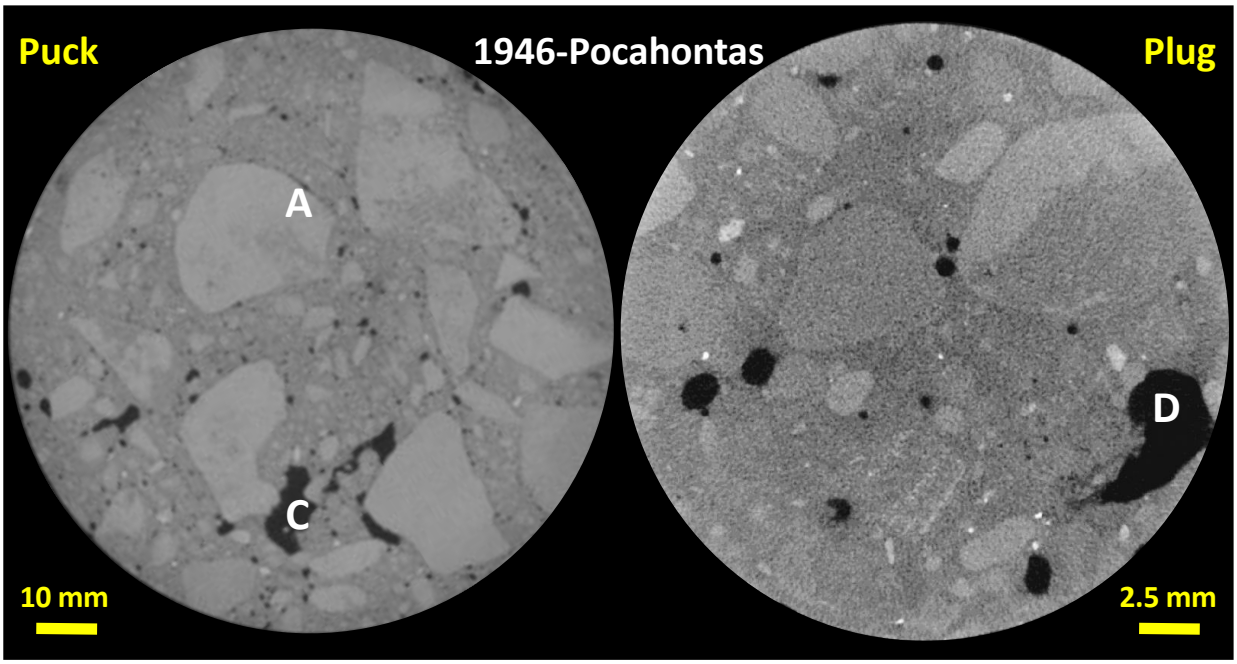

*Representative puck (59.2 microns/voxel) and plug (35 microns/voxel) CT images for pavement constructed **before 1950**: 1946-Pocahontas—Images show abundant circumgranular pores (A) are evident and some coalesce into larger irregularly shaped pores (C). Little deterioration of paste (D) is evident. The speckled nature of some of the coarse aggregate suggests density (i.e., mineralogical) variation.*

Figure 17. Representative puck and plug CT images for pavement constructed *before* 1950: 1946-Pocahontas

While deterioration (D) is evident in the paste in 1946-Pocahontas, no evidence of CA deterioration was observed. The CT intensities associated with its CA do vary, revealing a sometimes speckled nature that shows zonation and suggests different densities (i.e., spatial variation in mineralogy or porosity). The FA for 1946-Pocahontas has bright CT intensities, indicating denser grains that are distinguishable from the paste. Both the CA and FA for 1946-Pocahontas are subangular to angular.

1955-Greene

The oldest sample showing clear evidence of entrained air is 1955-Greene (Figure 18). The entrained air void pore type is rounded and has a more uniform shape (circular) and size (~2 mm in diameter) than other pore types. 1955-Greene also shows more pore type variation than the older samples. Circumgranular pores (A) remain evident in its CT images. Its moldic pores (B) likely formed due to FA dissolution. Both the circumgranular and moldic pores in 1955-Greene have coalesced (C) into larger, irregular void networks. In addition, the sample's plug image shows the detachment of a CA grain from the surrounding paste matrix. The CA grains in 1955-Greene have non-uniform grayscale intensities, indicating differences in grain densities (likely from intraparticle pores), though the CT intensities for its FA grains are similar to that of its paste, making the identification of boundaries between paste and grains challenging. Evidence of fracturing (F) is observable in some CA. The CA in 1955-Greene is more angular than in the pre-1950 samples.

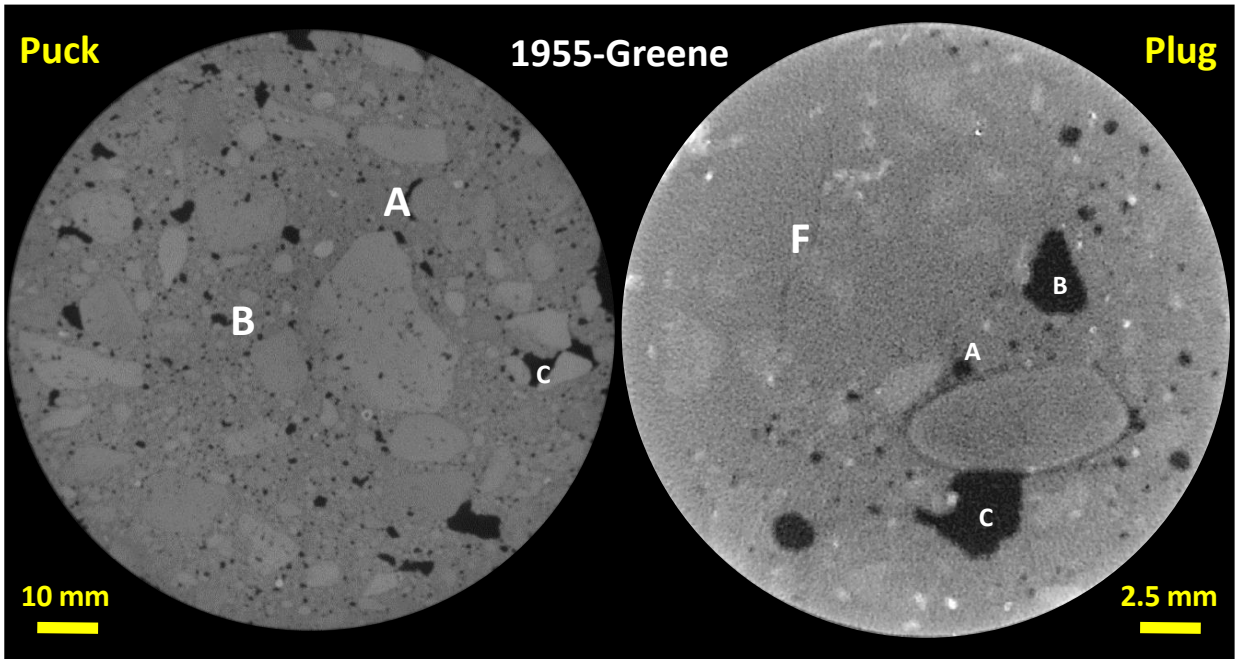

*Representative puck (59.2 microns/voxel) and plug (35 microns/voxel) CT images for pavements constructed **after 1950**: 1955-Greene—Images show circumgranular (A), moldic (B), and coalescent (C) pores as well as fractured coarse aggregate (F).*

Figure 18. Representative puck and plug CT images for pavement constructed *after* 1950: 1955-Greene

1963-Marshall

The CT images for 1963-Marshall show abundant circumgranular pores (Figure 19). These pores have coalesced (C) into an elongated air void network in the paste. The plug image shows intraparticle micropores in the CA grains as well as evidence of air voids not discernable on the puck scan. The sample's entrained air voids (E) are rounded and range between 0.5 and 2 mm in diameter. Its CA has varying intensities due to its intraparticle microporosity. Its grains also vary from subrounded to subangular. The FA is not distinguishable from the paste in 1963-Marshall except when its high density provides sufficient contrast.

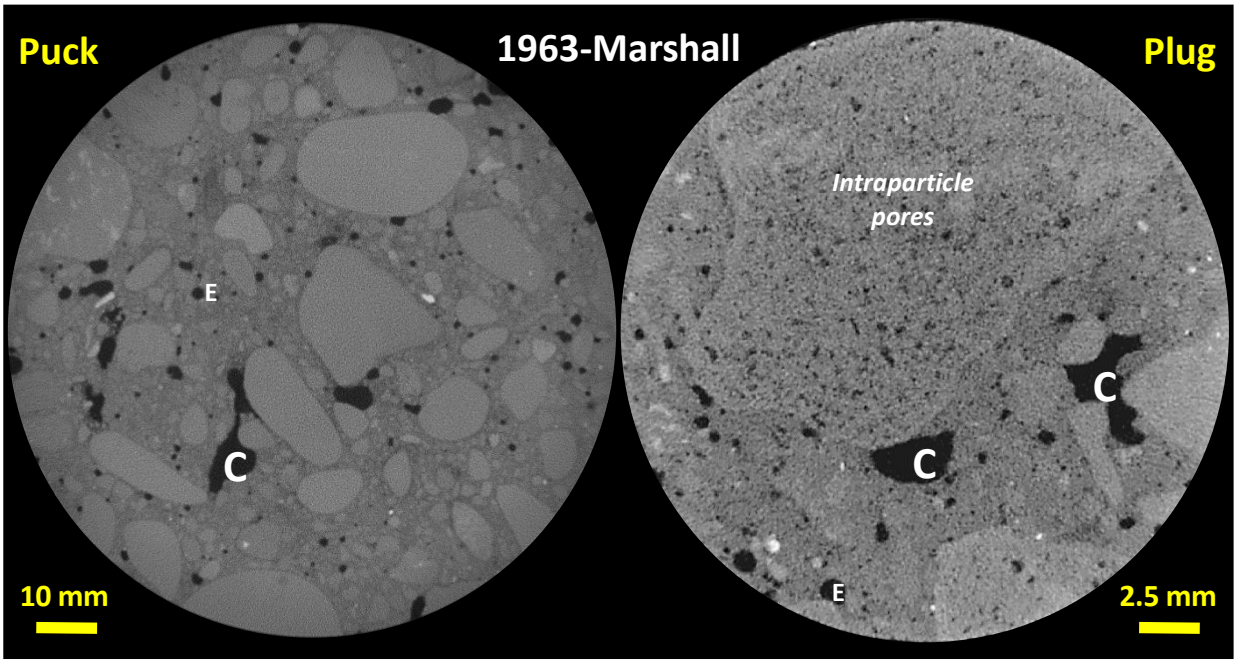

*Representative puck (59.2 microns/voxel) and plug (35 microns/voxel) CT images for pavement constructed **after 1950**: 1963-Marshall—Images show abundant circumgranular (unlabeled) and coalescent (C) pores; intraparticle pores are also visible in coarse aggregate. Entrained air (E) is visible in paste.*

Figure 19. Representative puck and plug CT images for pavement constructed *after* 1950: 1963-Marshall

1976-Hamilton

The puck image for 1976-Hamilton (Figure 20) shows partially deteriorated CA (D) that has detached from the paste and contains fractures. Small (<1 mm) circumgranular pores are evident in both puck and plug images as well as a network of abundant coalescent (C) air voids. The sample's entrained air pores (E) are subrounded and between 1 and 2 mm in diameter, easily discernible in the paste in both the puck and plug scans. The CA in 1976-Hamilton has two groups of CT intensities for its limestone grains: very bright (indicating undeteriorated grains) and dark (indicating ongoing deterioration, D). The FA often has similar CT intensities to the CA, making segmentation more difficult than with the other samples. Both the CA and FA in 1976-Hamilton are angular.

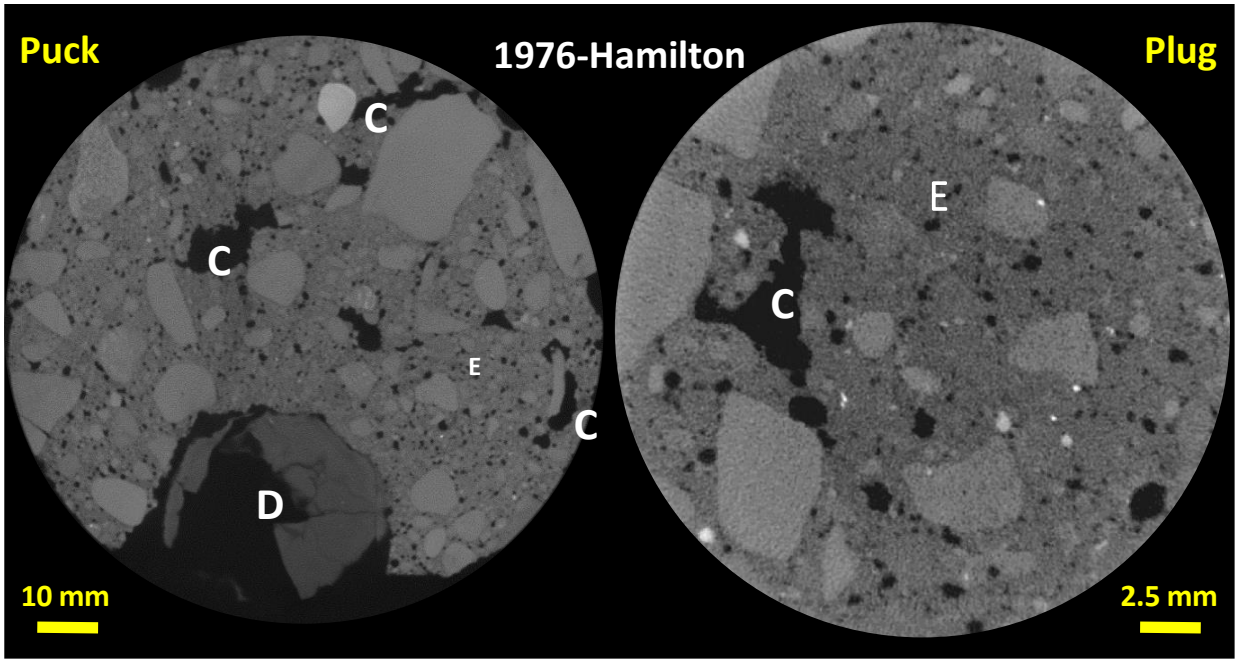

*Representative puck (59.2 microns/voxel) and plug (35 microns/voxel) CT images for pavements constructed **after 1950**: Hamilton (1976)—Images show abundant coalescent (C) pores and deterioration of coarse aggregate (D); entrained air (E) is visible in paste.*

Figure 20. Representative puck and plug CT images for pavement constructed *after* 1950: 1976-Hamilton

1980-Boone

The puck and plug CT images for 1980-Boone (Figure 21) show abundant circumgranular pores (A) formed around the edges of the CA, due to paste deterioration (D). Entrained air pores (E) are visible in the paste, subrounded, and between 0.5 and 1.5 mm in diameter. They tend to concentrate around gravel and to have coalesced (C), again due to paste deterioration.

The CA in 1980-Boone is less deteriorated, having moderately uniform CT intensities that indicate similar densities and possibly one source. The FA is visible, but it often has CT intensities that are similar to those of the paste. Most of the sample's aggregate grains are very angular.

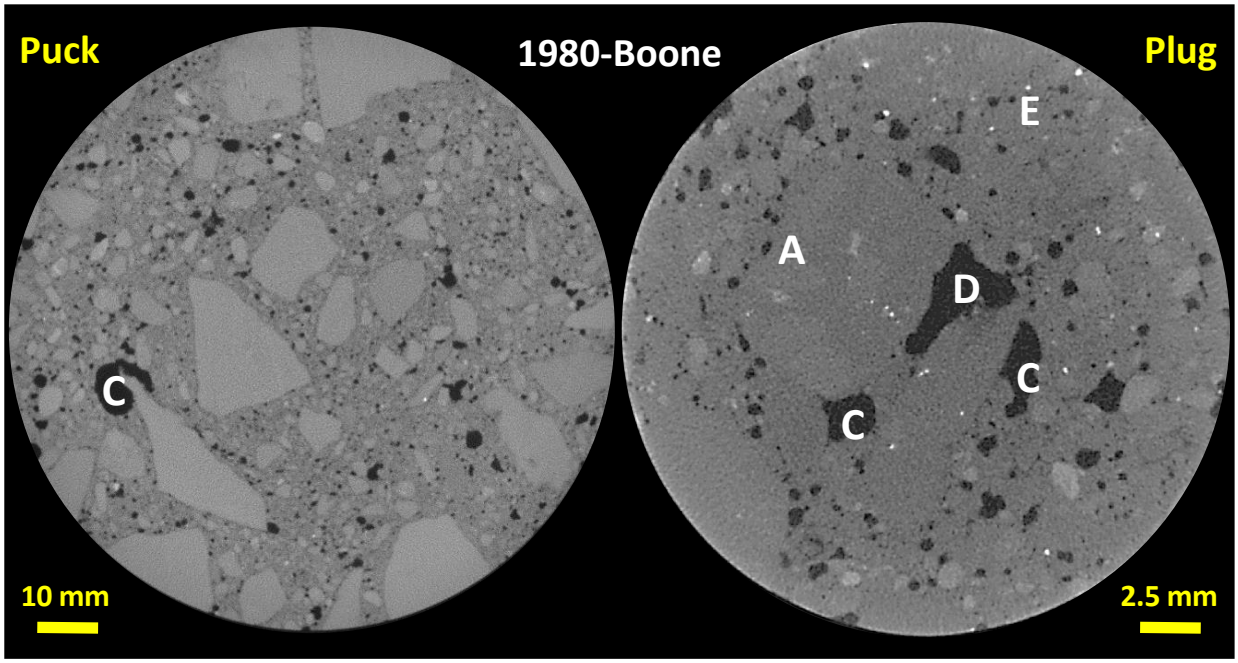

*Representative puck (59.2 microns/voxel) and plug (35 microns/voxel) CT images for pavements constructed **after 1950**: Boone (1980)—Images show abundant circumgranular (A) pores and coalescent (C) pores and less deterioration of coarse aggregate (D); entrained air (E) is also visible in paste.*

Figure 21. Representative puck and plug CT images for pavement constructed *after* 1950: 1980-Boone

1992-Story

The 1992-Story puck image (Figure 22) shows rare circumgranular pores but abundant coalescent pores (C) that form the air void network between the CA. Mostly the CA shows uniform CT intensities indicative of a uniform lithology, though some CA shows evidence of internal pores. The sample's CA grains are subangular to angular. Its entrained air pores are less evident due to the low resolution of the puck's CT volume (59.2 μm).

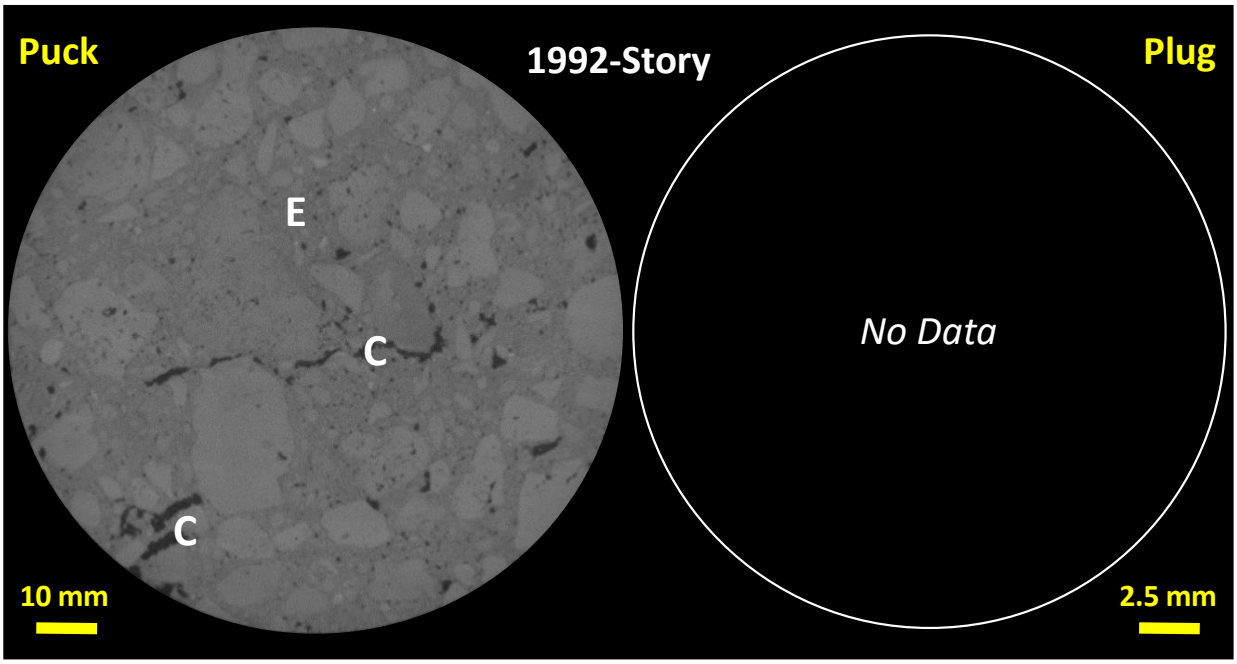

*Representative puck (59.2 microns/voxel) and plug (35 microns/voxel) CT images for pavements constructed **after 1950**: 1992-Story—Images show abundant coalescent (C) pores forming the air void network. Entrained air pores (E) are visible in the paste.*

Figure 22. Representative puck CT image for pavement constructed *after* 1950: 1992-Story

1997-Linn

The puck and plug images of 1997-Linn (Figure 23) show abundant coalescent pores (C) formed on the edges of CA and between coarse grains in the paste. Intraparticle pores in the CA are visible in the plug image. A dark-colored CA grain in the puck image also shows ongoing deterioration (D) that appears to be leading to the grain detaching from the paste matrix. Other coarse grains are subrounded to angular and have uniform CT intensities. Entrained air pores (E) are visible in the paste, subrounded, and between 0.5 and 2 mm in diameter.

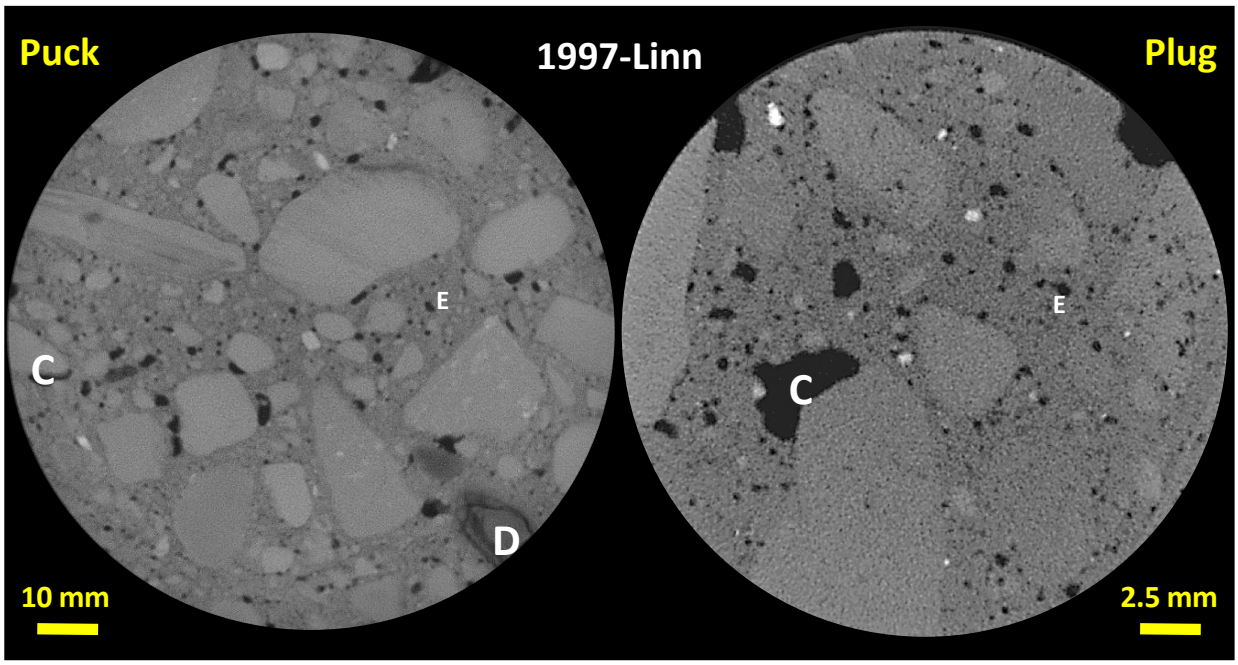

*Representative puck (59.2 microns/voxel) and plug (35 microns/voxel) CT images for pavements constructed **after 1950**: 1997-Linn—Images show abundant circumgranular pores (unlabeled) as well as coalescent (C) pores and deteriorating coarse aggregate (D); intraparticle pores in coarse aggregate and entrained air (E) are also visible in paste.*

Figure 23. Representative puck and plug CT images for pavement constructed *after* 1950: 1997-Linn

2002-Jones

The CT images for 2002-Jones (Figure 24) show a pore network connected through coalescent pores (C) between coarse grains. Intraparticle pores are evident in the CA that connect with the coalescent pores that have formed along the edges of the CA. Interparticle pore networks are elongated and have formed due to paste deterioration. CT intensities show moderate variations in the CA that indicate deterioration-related differences in the density of the limestone grains. Entrained air pores (E) are visible in the paste, subrounded, and between 0.5 and 1.5 mm in diameter. The sample's aggregate grains vary from subangular to angular.

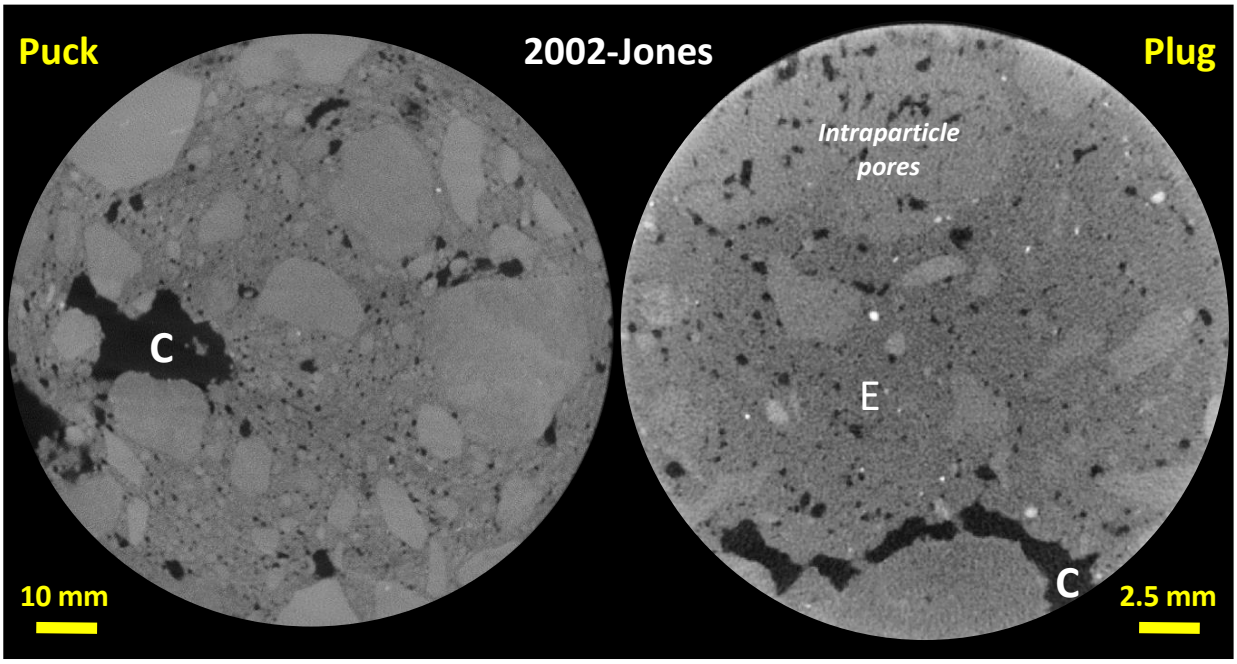

*Representative puck (59.2 microns/voxel) and plug (35 microns/voxel) CT images for pavements constructed **after 1950**: 2002-Jones—Images show abundant coalescent (C) pores and entrained air (E) are also visible in paste.*

Figure 24. Representative puck and plug CT images for pavement constructed *after* 1950: 2002-Jones

Relative Abundance of Components

The CT images allowed us to measure the relative abundance of each phase (e.g., pores, aggregate, and paste) in three dimensions .The relative abundance of each segmented phase shows a slight trend toward decreasing CA in younger samples due to the increases in pore space that result from entrained air (Table 6 previously and Figure 25).

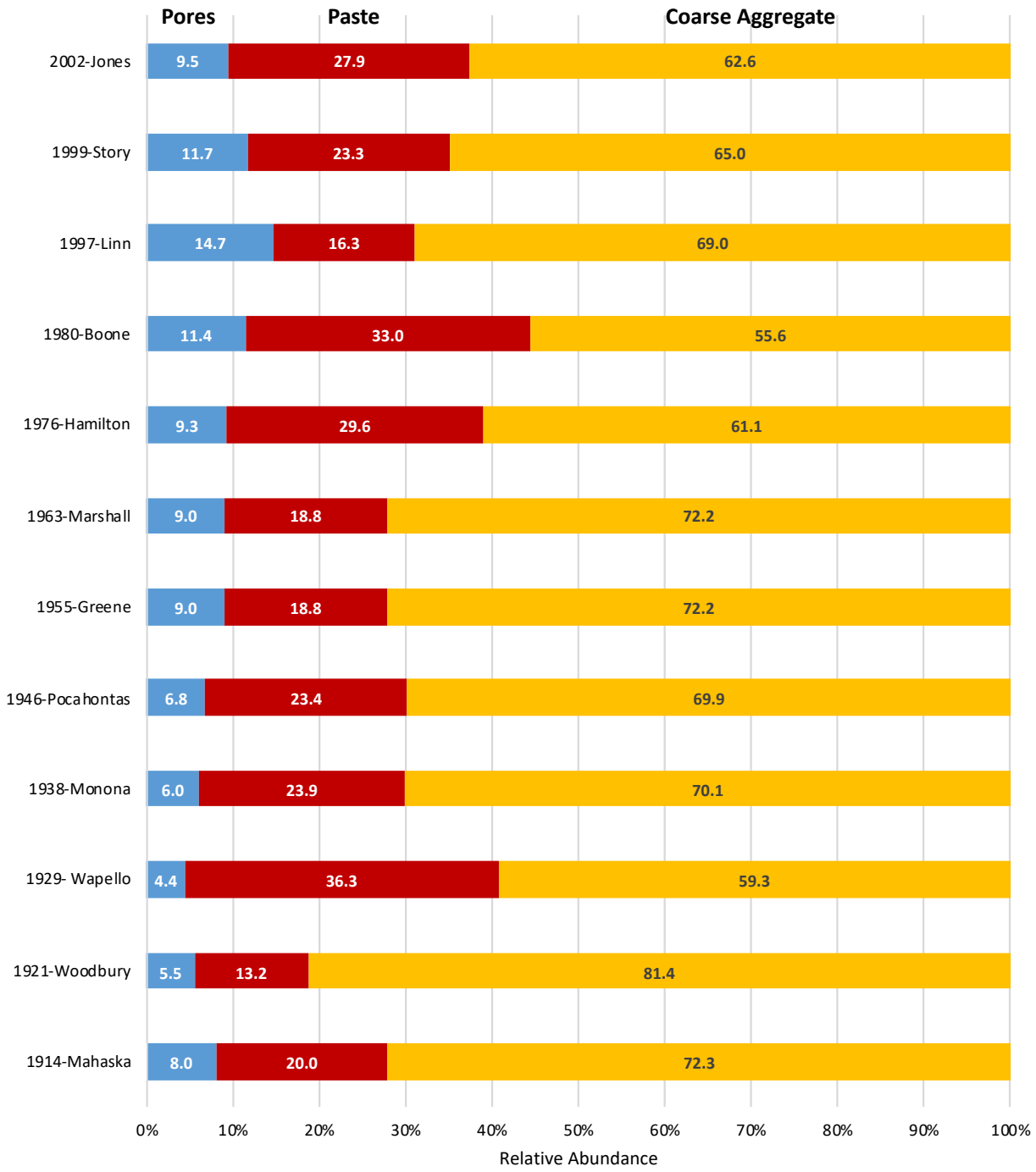

Figure 25. Relative abundance of PCC components: CA, paste, and pores

Because CT-measured porosity had a good match to helium porosity, voxels assigned to the pore phase were used as the basis for thresholding pores in all samples. The segmentation of the FA from the paste was challenging because the CT scan resolution's partial-volume effect meant that the voxel intensities for the FA and paste overlapped, resulting in FA likely being included in the paste values). The confounding effect of FA often being indiscernible from the paste likely

explains why, while the porosity of both the puck and plug sample sizes is highly correlated, the puck and plug abundances for paste and CA are less so as indicated by a lower R^2 (Figure 26). (Because relative abundance is calculated out of 100%, errors in the paste also affect CA measurement.)

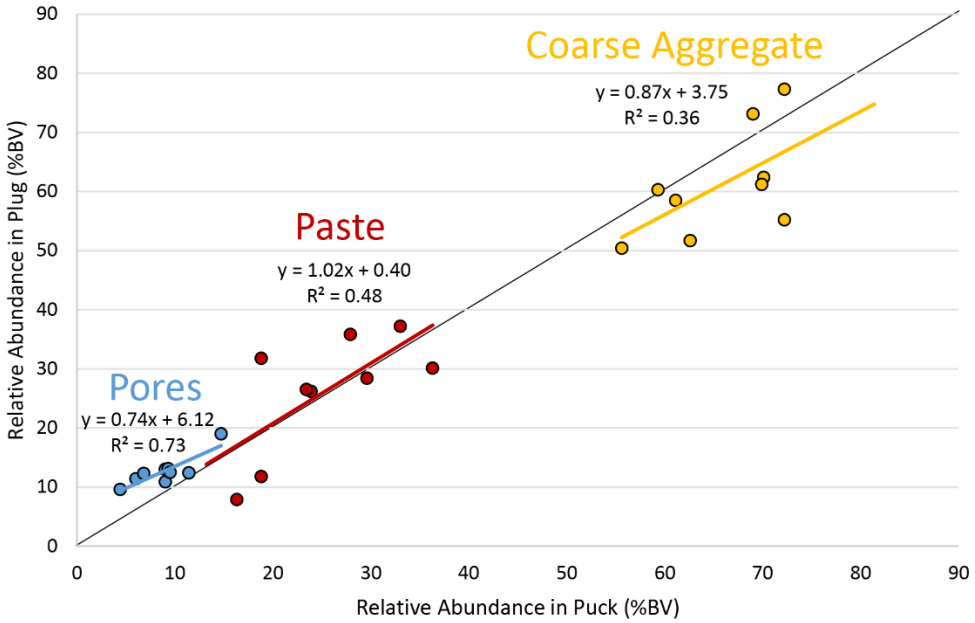

Figure 26. Correlation between the relative abundance of components in pucks and plugs

CT Porosity

As was stated previously, helium porosity was used as a guide to identify the proper intensity threshold in order to discriminate the pore space in the CT data. This resulted in a fairly strong correlation between helium porosity and CT porosity (R^2 = 0.9 for pucks, 0.7 for plugs, Figure 27).

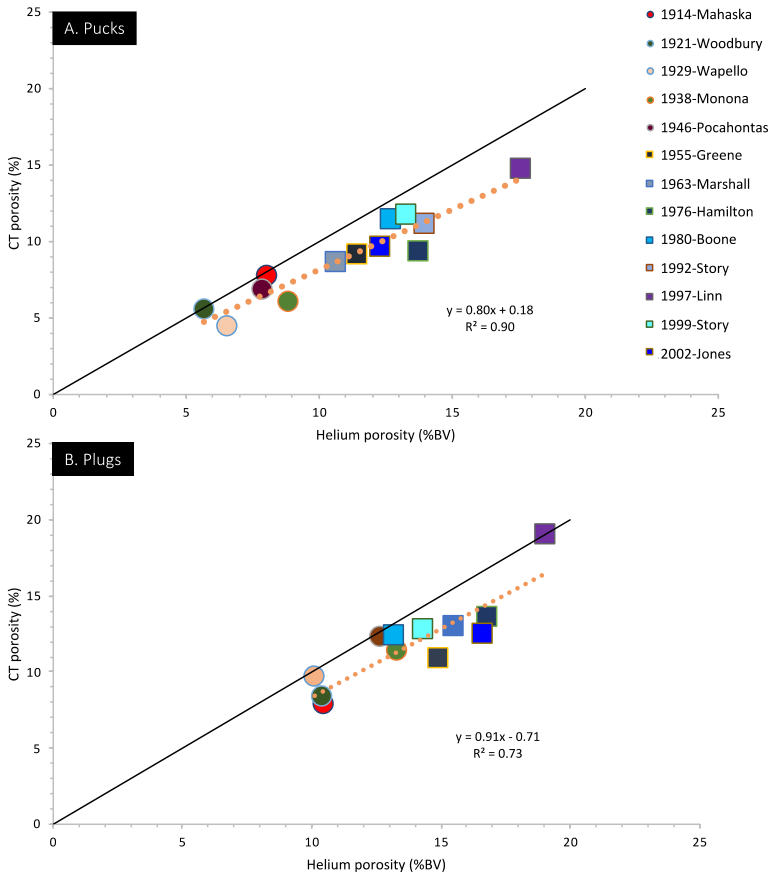

Figure 27. Comparison of helium- and CT-measured porosity

Pre-1950 pucks show closer correlation between helium and CT porosities' higher deviation in porosity (~5–6 percentage points) than post-1950 samples (which had a deviation of less than 5 percentage points). This was likely due to the older samples containing less entrained air below the resolution of the CT scan.

For plug data (Figure 27B), both pre- and post-1950 samples show similar deviation between helium and CT porosities, with the post-1950 samples (aside from 1997-Linn) showing a greater difference than the pre-1950 samples.

The CT porosity for plugs was higher than for pucks (Figure 27) in all samples because the voxel size in the CT images of the plugs was smaller (35 µm) than in the pucks (60 µm), allowing smaller pores in the plugs to be recognized. Paste volumes were just as likely to be higher as lower in the plugs compared to the pucks and coarse aggregates were almost always higher in the pucks.

Measurements of porosity from CT data and from helium pycnometry reveal a clear trend of decreasing porosity with age (cf. Figure 3), with the pre-1950 and post-1950 samples forming two separate porosity groups along the same trend. Specifically, the match between helium- and CT-measured porosity for pucks improves with sample age, suggesting the older samples had

fewer pores below the CT resolution (Figure 27A). For plugs, their helium and CT-measured porosity match less closely (Figure 27B). (The solid black line in the background of both Figures 27A and B is unity.) Therefore, the CT images provide evidence that the additional pore volume in the post-1950 samples was created from 1) entrained air void networks and 2) deteriorating aggregate and paste. In addition, the entrained air pores in post-1970 samples are more irregularly shaped than those from between the 1950s and 1970s. This might indicate ongoing deterioration in the paste, resulting in changed pore shape and increasing porosity and permeability. Pores formed due to aggregate deterioration may have connected with entrained air voids to form a complex pore system.

The RapidAir 457 Air Void Analyzer (hereafter "RapidAir") produced a 2D (ASTM C457) measurement of air void content that differs significantly from both the CT and helium porosities (Figure 28).

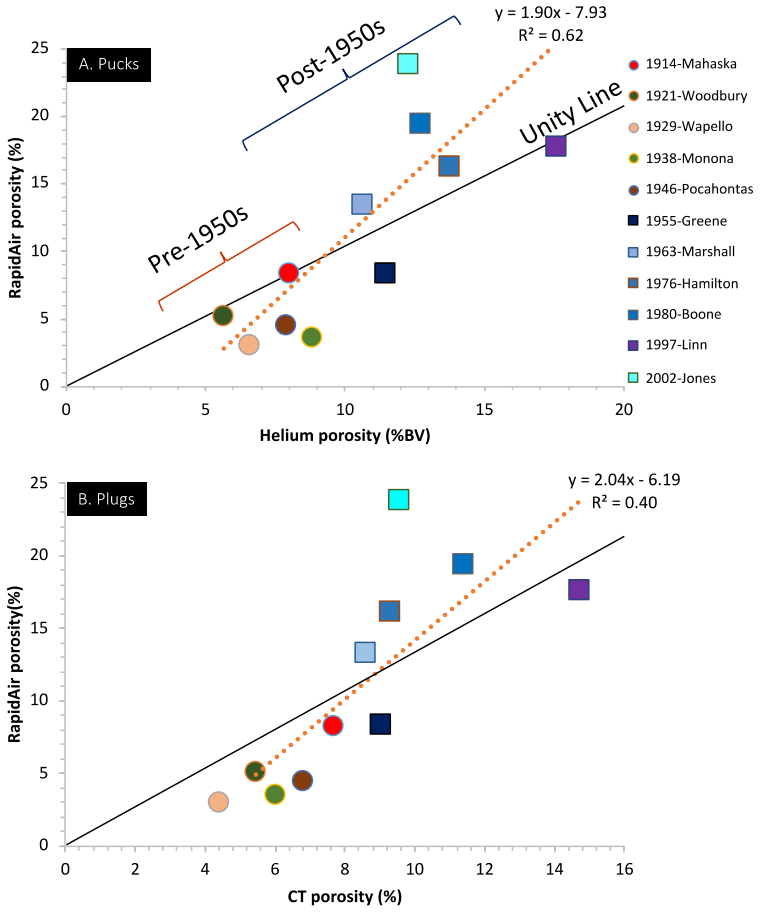

Figure 28. Comparison of RapidAir-(ASTM-C457)-, helium-, and CT-measured porosity

The correlation between the RapidAir and helium porosities for the pucks can be described by an R^2 of 0.6 (Figure 28A). However, there is again a clear difference in behavior between the pre- and post-1950 samples, with porosity decreasing with age like described above. Pre-1950

samples have a helium porosity greater than or approximately equal to their RapidAir porosity, while post-1950 samples have, for the most part, a helium porosity less than their RapidAir porosity.

The plug helium porosity shows a weaker correlation with RapidAir (ASTM C457) porosity than the puck helium porosity does but exhibits similar behavior for both the pre- and post-1950 samples in that the plug helium porosity also decreases with sample age (Figure 28B). This can be interpreted as pre-1950 samples having more pores that can be seen by the helium method and cannot be seen by the RapidAir method. On the other hand, post-1950 samples have more pores that can be seen by the RapidAir than helium method—a counterintuitive result. One possible explanation is that the air entrainment process used to construct the post-1950 samples yielded a significant number of isolated pores (i.e., pores not connected to the exterior of the sample and thus not measurable by helium).

Porosity measured by the two image-analysis methods, CT and thin section images (with 2D CT images selected from the 3D volumes of plugs scanned at 35 µm per voxel), shows little correlation (R^2=0.04) (Figure 29).

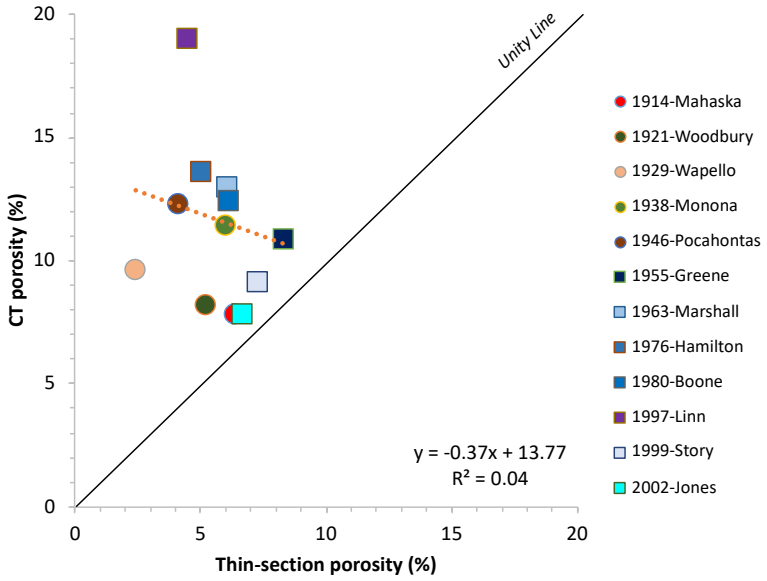

Figure 29. Comparison of porosity measured via thin section and CT images

Size Distribution of Grains and Pores

To avoid artifacts and unreliable data from the puck and plug CT images, only grain and pore size distributions were calculated for each sample (Tables 7 and 8, Figures 30 and 31).

The pre-1950 pucks show a mode of 210 µm for equivalent grain diameters and 230 µm for equivalent pore diameters. The post-1950 pucks show similar modes of 230 µm for equivalent grain diameters and 220 µm for equivalent pore diameters. All plugs show two matching modes

at 1) 80 µm and 2) 200 µm. The fact that the most abundant size of grains and pores is similar for all samples suggests that the original size of the deteriorated grains was equivalent to the current pore size.

This hypothesis was further tested with mercury porosimetry, which was used to characterize the pore-throat size distribution down to ~5 nm. For pre-1950 samples (Figure 5 above), three pore-throat modes were identified: 1) pore throats that connect pores formed in deteriorating paste (<25 nm), 2) pore throats that connect intraparticle pores (~50 nm), and 3) pore throats that connect interparticle pores (~250 nm). For post-1950 samples (previous Figure 6), an additional pore-throat type (entrained) was observed at sizes > 1 micron. The highest intruded volume was in the interparticle range for the pre-1950 samples (previous Figure 5) and intraparticle range for the post-1950 samples (Figure 6 above).

Table 7. Size distribution of pores and grains from puck and plug CT data by area

		Grain Area (µm²)					Pore Area (µm²)				
	Sample	Min	Median	Mean	St Dev	Max	Min	Median	Mean	St Dev	Max
Pucks	1914-Mahaska										
	1921-Woodbury										
	1929-Wapello	1.1E+04	2.0E+04	1.3E+06	1.3E+09	1.3E+12	1.1E+04	2.0E+04	1.6E+05	4.9E+07	3.7E+10
	1938-Monona	1.1E+04	1.4E+05	6.6E+06	1.4E+09	4.6E+11	1.1E+04	2.0E+04	1.9E+05	1.0E+08	1.0E+11
	1946-Pocahontas	1.1E+04	1.4E+05	8.8E+06	1.8E+09	6.9E+11	1.1E+04	2.0E+04	2.0E+05	1.3E+08	1.4E+11
	1955-Greene	1.1E+04	2.0E+04	1.5E+06	1.3E+09	1.2E+12	1.1E+04	2.0E+04	2.4E+05	1.1E+08	1.1E+11
	1963-Marshall	1.1E+04	1.4E+05	9.0E+06	1.8E+09	7.2E+11	1.1E+04	2.0E+04	2.2E+05	1.5E+08	1.6E+11
	1976-Hamilton	1.1E+04	2.0E+04	1.2E+06	1.2E+09	1.2E+12	1.1E+04	2.0E+04	3.6E+05	1.8E+08	1.8E+11
	1980-Boone	1.1E+04	2.0E+04	1.3E+06	7.6E+08	5.7E+11	1.1E+04	2.0E+04	3.7E+05	2.5E+08	2.5E+11
	1992-Story	1.1E+04	2.0E+04	1.8E+06	1.5E+09	1.2E+12	1.1E+04	2.0E+04	2.7E+05	1.0E+08	9.4E+10
	1997-Linn	1.1E+04	2.0E+04	1.2E+06	1.2E+09	1.2E+12	1.1E+04	2.0E+04	3.6E+05	1.8E+08	1.8E+11
	1999-Story										
	2002-Jones	1.1E+04	2.0E+04	1.5E+06	1.5E+09	1.5E+12	1.1E+04	2.0E+04	4.1E+05	3.4E+08	3.5E+11
Plugs	1929-Wapello	4.5E+03	1.4E+04	5.9E+05	1.6E+08	4.6E+10	4.5E+03	1.1E+04	5.1E+04	2.4E+06	5.0E+08
	1938-Monona	4.5E+03	1.3E+04	3.5E+05	1.2E+08	4.5E+10	4.5E+03	1.1E+04	2.7E+05	2.1E+06	8.7E+07
	1946-Pocahontas	4.5E+03	1.3E+04	4.6E+05	2.0E+08	9.3E+10	4.5E+03	1.3E+04	4.7E+05	8.3E+06	5.1E+08
	1955-Greene	4.5E+03	1.3E+04	3.1E+05	9.9E+07	3.5E+10	4.5E+03	1.3E+04	1.1E+05	1.5E+06	1.5E+08
	1963-Marshall	4.5E+03	1.3E+04	3.6E+05	1.6E+08	8.0E+10	4.5E+03	1.7E+04	8.3E+04	1.3E+06	2.3E+08
	1976-Hamilton	4.5E+03	1.3E+04	2.4E+05	9.4E+07	4.5E+10	4.5E+03	1.7E+04	1.1E+05	1.8E+06	3.6E+08
	1980-Boone	4.5E+03	1.3E+04	2.7E+05	1.2E+08	5.6E+10	4.5E+03	1.3E+04	9.1E+04	1.1E+07	4.4E+09
	1997-Linn	4.5E+03	1.4E+04	6.0E+05	2.6E+08	1.2E+11	4.5E+03	1.9E+04	1.3E+05	1.1E+06	1.4E+08
	2002-Jones	4.5E+03	1.4E+04	3.3E+05	1.3E+08	5.5E+10	4.5E+03	2.0E+04	1.1E+05	1.6E+06	3.2E+08

Table 8. Size distribution of pores and grains from puck and plug CT data by diameter

		Grain Diameter (µm)					Pore Diameter (µm)				
	Sample	Min	Median	Mean	St Dev	Max	Min	Median	Mean	St Dev	Max
Pucks	1914-Mahaska	73	158	190	139	4.4E+04	73	147	205	178	3.2E+04
	1921-Woodbury	73	93	106	120	5.7E+04	73	93	109	78	2.8E+04
	1929-Wapello	73	93	106	81	6.7E+04	73	93	108	109	1.7E+04
	1938-Monona	73	185	194	214	5.0E+04	73	93	107	107	2.9E+04
	1946-Pocahontas	73	185	201	249	5.6E+04	73	93	106	74	3.0E+04
	1955-Greene	73	93	103	88	7.0E+04	73	93	110	100	2.8E+04
	1963-Marshall	73	185	207	251	5.5E+04	73	93	105	80	3.7E+04
	1976-Hamilton	73	93	106	80	6.4E+04	73	93	116	113	4.1E+04
	1980-Boone	73	93	102	91	5.2E+04	73	93	116	110	4.7E+04
	1992-Story	74	93	102	95	7.2E+04	74	93	114	117	2.7E+04
	1997-Linn	73	93	106	80	6.4E+04	73	93	116	113	4.1E+04
	1999-Story	73	93	106	91	5.1E+04	73	93	101	63	5.1E+04
	2002-Jones	74	93	106	84	6.9E+04	74	93	110	79	3.9E+04
Plugs	1929-Wapello	47	74	82.6	93	2.5E+04	47	67	78	69	7.0E+03
	1938-Monona	47	74	81.8	60	1.7E+04	47	67	136	231	4.5E+03
	1946-Pocahontas	47	74	81.5	62	2.3E+04	47	74	152	271	7.1E+03
	1955-Greene	47	74	83.0	68	1.9E+04	47	74	108	121	4.5E+03
	1963-Marshall	47	74	83.3	62	2.2E+04	47	80	105	93	5.1E+03
	1976-Hamilton	47	74	83.3	63	1.9E+04	47	80	112	108	4.6E+03
	1980-Boone	47	74	82.1	65	2.2E+04	47	74	90	81	8.7E+03
	1997-Linn	47	74	85.0	66	2.3E+04	47	85	122	121	4.7E+03
	2002-Jones	47	74	83.3	63	2.0E+04	47	85	119	110	5.2E+03

To measure pore size distribution, computational image analysis was undertaken, initially for the three test samples only (Figure 30).

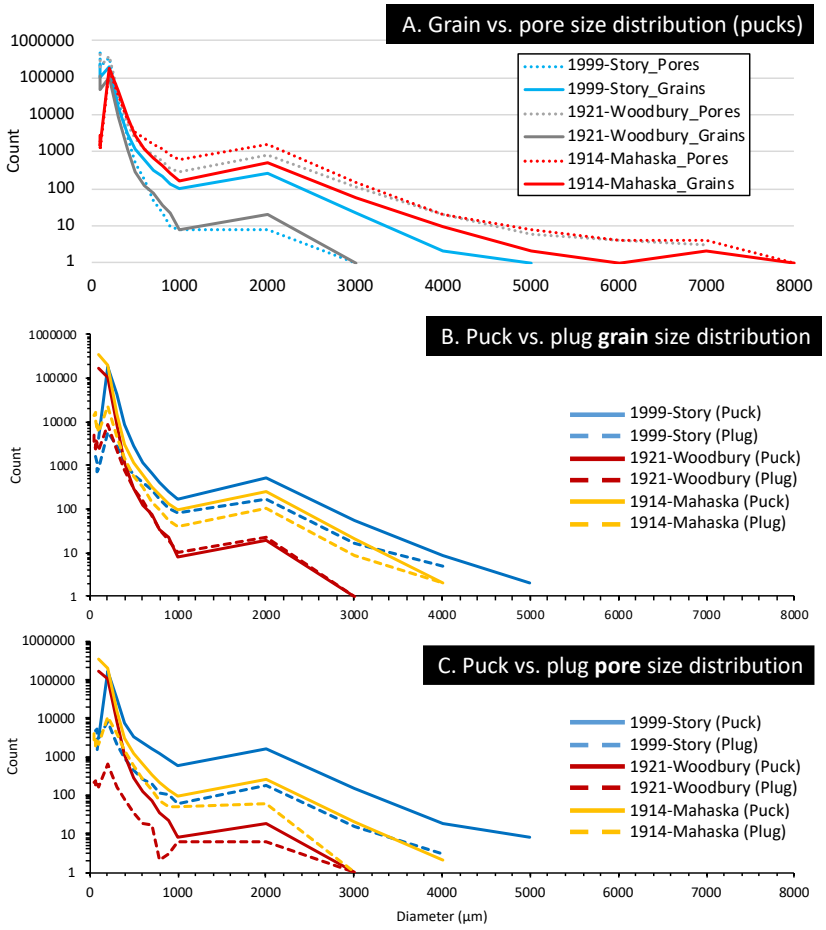

Figure 30. Size distribution histogram of grains and pores from the 1914-Mahaska, 1921-Woodbury, and 1999 Story test samples

While 1999-Story's grain size distribution falls between that of 1914-Mahaska and 1921-Woodbury, its pore size distribution is much lower (Figure 30A). This difference could arise from the different construction practices and materials used for 1914-Mahaska and 1921-Woodbury compared to 1999-Story.

Computational image analysis was then undertaken to measure the pore size distributions for the remaining PCC samples in this study (Figure 31).

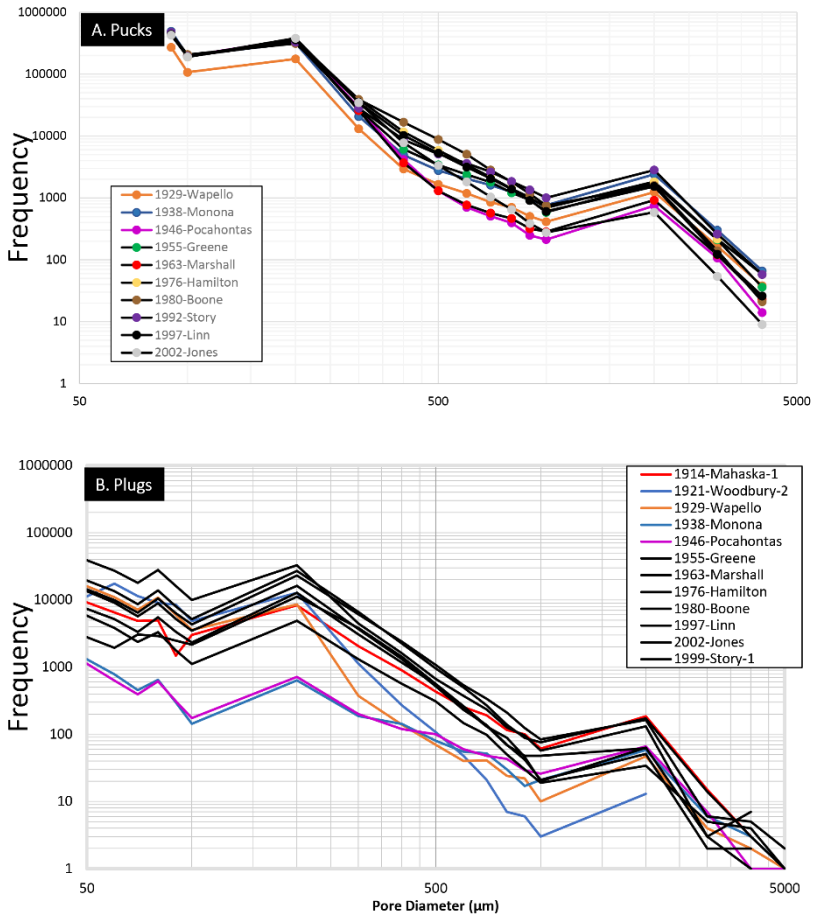

Figure 31. Pore size distribution calculated from the CT data for pucks (A) and plugs (B)

For pucks, the pore size distributions for pre- and post-1950 samples show little difference (Figure 31A). However, when the smaller plug samples were analyzed (Figure 31B), it was found that the pre-1950 samples exhibit a wider variety of distributions, whereas the post-1950 samples have fairly similar pore size distributions. This suggests that the differences between the pore systems of pre- and post-1950 samples could lie in smaller pore sizes—sizes that were glossed over by the partial volume effect when scanning pucks (at a 60-µm resolution) but not when scanning plugs (at a 35-µm resolution).

Evaluation of CT Porosity Measurements

Pore networks in pavement materials are composed of pore bodies and the pore throats that connect them. In this study, CT images were segmented according to the smallest distinguishable feature (at 60 µm for pucks and 35 µm for plugs). Some pores and pore throats were not visible in the CT images due to the technique's resolution as well as to data acquisition artifacts. Although pore body and pore throat size may have been below CT resolution, they may nevertheless be vital for quantifying pore connectivity developed due to deterioration.

Thin Section Imaging—Mosaics

Analysis of thin sections cut from PCC plugs allows characterization of the texture and components of PCC at a finer scale over a broader area than is possible via computed tomography. Features as small as a few microns can be observed via thin section, whereas the resolution of CT data is often in the tens-of-microns range. Thin sections also allow the identification of grain types (e.g., ooids, peloids, fossils, etc.) and of the mineralogy for coarse and fine aggregate that is not possible with CT (Tables 9 and 10).

Table 9. Visual description of thin section images

Thin Section	Pore Roundness (Paste)	Pore Roundness (Interparticle)	Pore Network (Natural, Entrained)	Pore type (Circumgranular, Moldic, Deterioration, Paste)	Pore Connectivity	Grain Roundness	Grain Deterioration (Partial, Full, Fractures)
1929- Wapello	Rounded	Irregular dissolution	Natural	Circumgranular and Paste	Yes (in paste)	Semi-rounded	Fractures
1938-Monona	Rounded	Irregular dissolution	Natural	Circumgranular and Paste	Yes	Semi-rounded	Partial and Fractures
1946-Pocahontas	Rounded	Irregular dissolution	Natural	Circumgranular and Paste	Yes	Semi-rounded	Partial and Fractures
1955-Greene	Rounded and Irregular	Irregular dissolution	Both	Circumgranular, Moldic, Deterioration, and Paste	Yes (in paste)	Semi-rounded	Partial, Full, and Fractures
1963-Marshall	Rounded and Irregular	Irregular dissolution	Both	Circumgranular, Deterioration, and Paste	Yes	Semi-rounded	Partial and Fractures
1976-Hamilton	Rounded and Irregular	Irregular dissolution	Both	Circumgranular and Deterioration	Yes (in some grains)	Semi-rounded	Partial and Fractures
1980-Boone	Rounded and Irregular	Irregular dissolution	Both	Circumgranular, Moldic, and Deterioration	No	Semi-rounded	Partial and Fractures
1997-Linn	Rounded and Irregular	Irregular dissolution	Both	Circumgranular and Deterioration	Yes (in carb grains)	Semi-rounded	Partial and Fractures
2002-Jones	Rounded and Irregular	Irregular dissolution	Both	Circumgranular and Deterioration	Yes (in carb grains)	Semi-rounded	Partial and Fractures

Table 10. Visual description of coarse aggregate (CA) lithology, pore types, and CA deterioration

Sample	Lithology	Visible Porosity			Visible CA Deterioration	Porosity (%Area)
		Within CA	Between CA	Large Voids		
1914-Mahaska	Igneous & Metamorphic	None	Common	Rare	Rare	6.4
1921-Woodbury	Igneous & Metamorphic	None	Common	Rare	Rare	5.2
1929-Wapello	Crushed limestone	None	Common	Common	Rare	2.4
1938-Monona	Igneous & Metamorphic	None	Rare	None	Rare	6.0
1946-Pocahontas	Igneous & Metamorphic	None	Rare	Rare	Rare	4.1
1955-Greene	Igneous & Metamorphic	None	Common	Rare	Rare	8.3
1963-Marshall	Crushed limestone	Rare	Rare	Rare	None	6.1
1976-Hamilton	Crushed limestone	None	Common	Rare	Rare	5.1
1980-Boone	Igneous & Metamorphic	None	Common	Common	Rare	6.1
1992-Story	Crushed limestone	None	Common	Common	None	Not Calculated
1997-Linn	Crushed dolostone	Common	Abundant	None	None	4.5
1999-Story	Crushed limestone	None	Abundant	Rare	None	7.3
2002-Jones	Crushed dolostone	Abundant	Abundant	Rare	None	6.7

1914-Mahaska

Thin sections from 1914-Mahaska (Figures 32–36) show a PCC composed of CA that is a subrounded gravel consisting of igneous and metamorphic rock fragments. Much of the CA is quartzite. The fine aggregate (FA) is dominated by coarse-grained, angular quartz. Some CA has internal pores suggestive of selective mineral dissolution from igneous rock fragments. Other CA fragments are undergoing wholesale disintegration. The paste is for the most part opaque, suggesting a lack of micron-sized intra-paste pores. Numerous large pores are present that have both smooth and irregular boundaries, suggesting multiple origins.

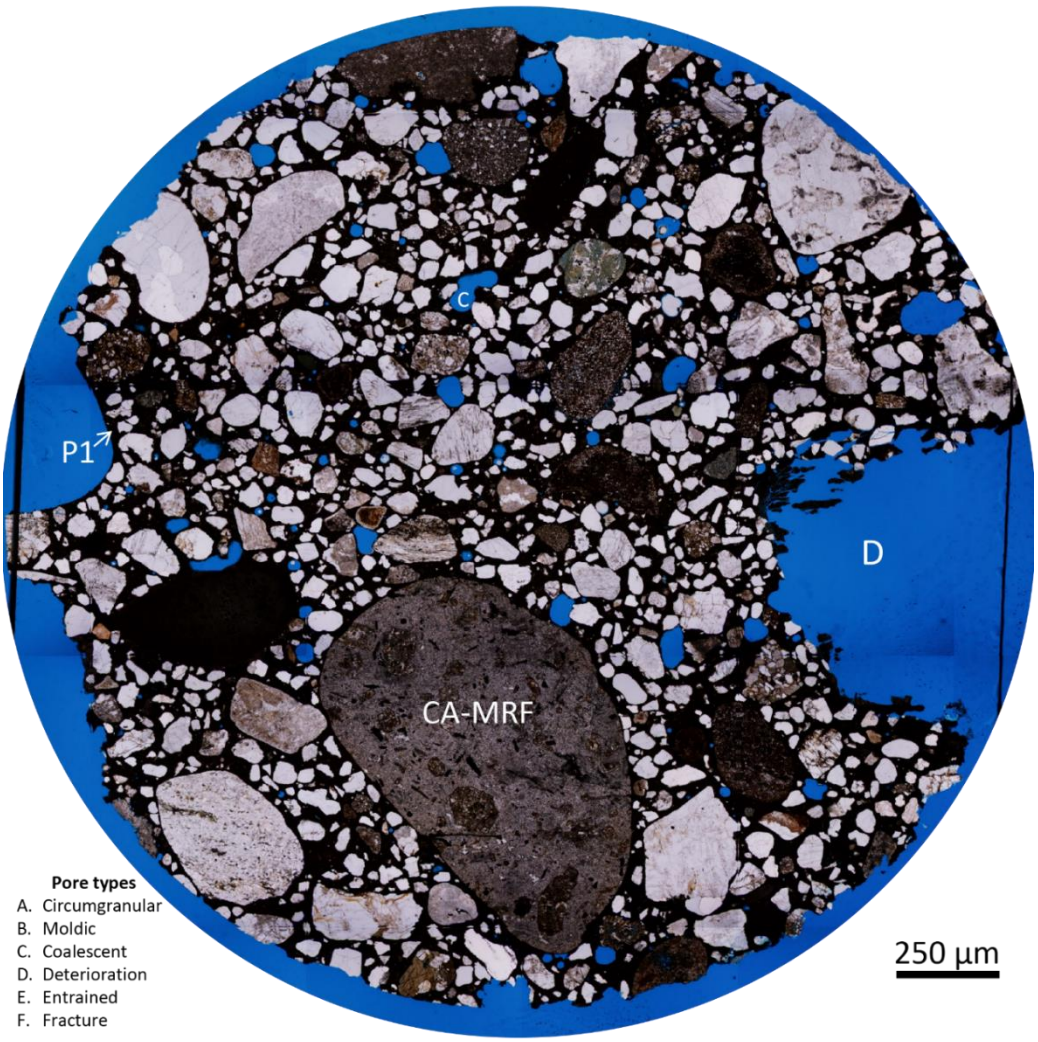

Thin section photomosaic from 1914-Mahaska showing PCC components: CA is composed of a metamorphic rock fragment (CA-MRF). FA is composed of angular-to-rounded quartz grains as well as of rounded igneous and metamorphic rock fragments. Pores have rounded edges lined with FA. One large pore is present, suggesting large-scale deterioration of PCC components. Paste is uniformly dark (P1).

Figure 32. Thin section photomosaic from 1914-Mahaska showing PCC components (#1)

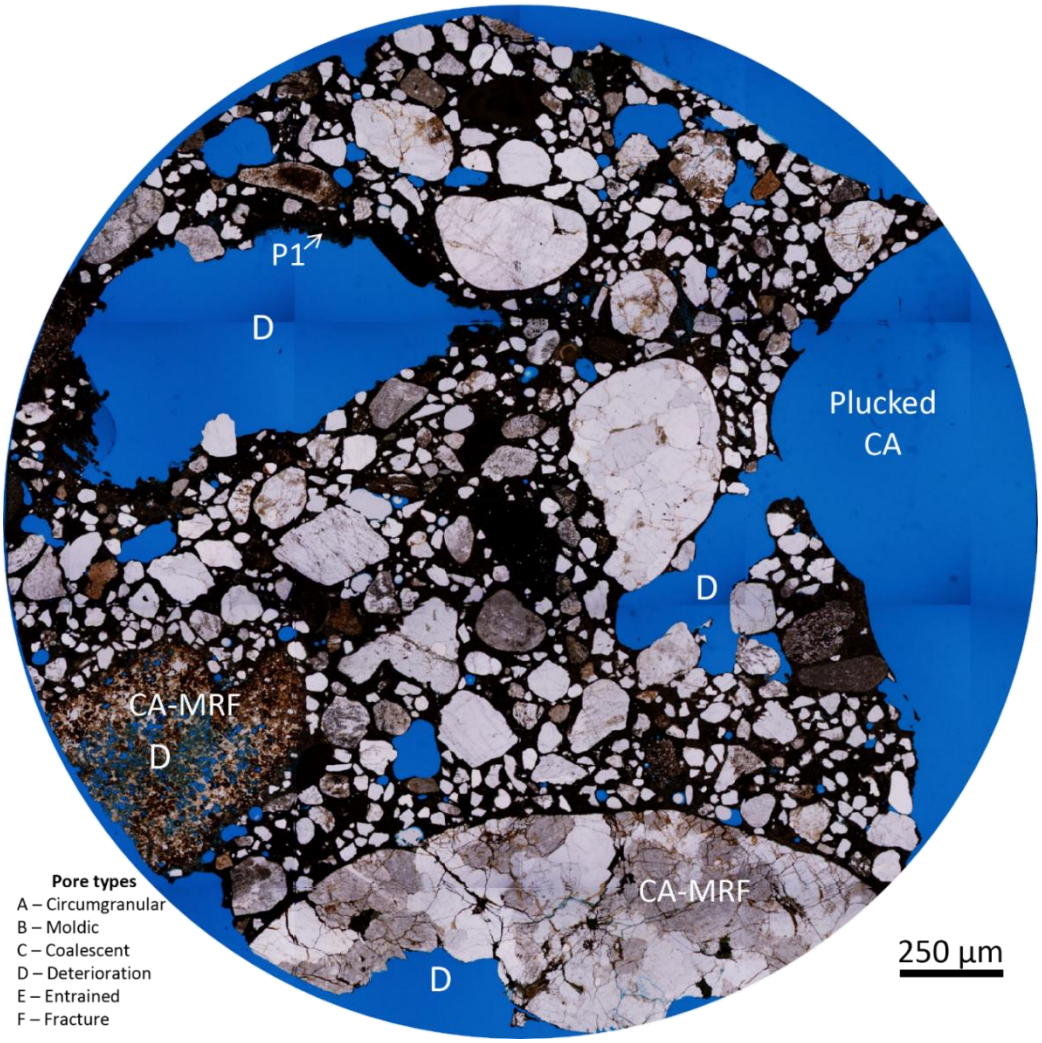

Thin section photomosaic from 1914-Mahaska showing PCC components: CA is composed of metamorphic rock fragments (CA-MRF). FA is composed of angular-to-rounded quartz grains as well as of rounded igneous and metamorphic rock fragments. Pores have rounded edges lined with FA. One large pore is present, suggesting large-scale deterioration of PCC components. Paste is uniformly dark (P1). (One large pore is likely from a CA grain being plucked during thin section preparation.)

Figure 33. Thin section photomosaic from 1914-Mahaska showing PCC components (#2)

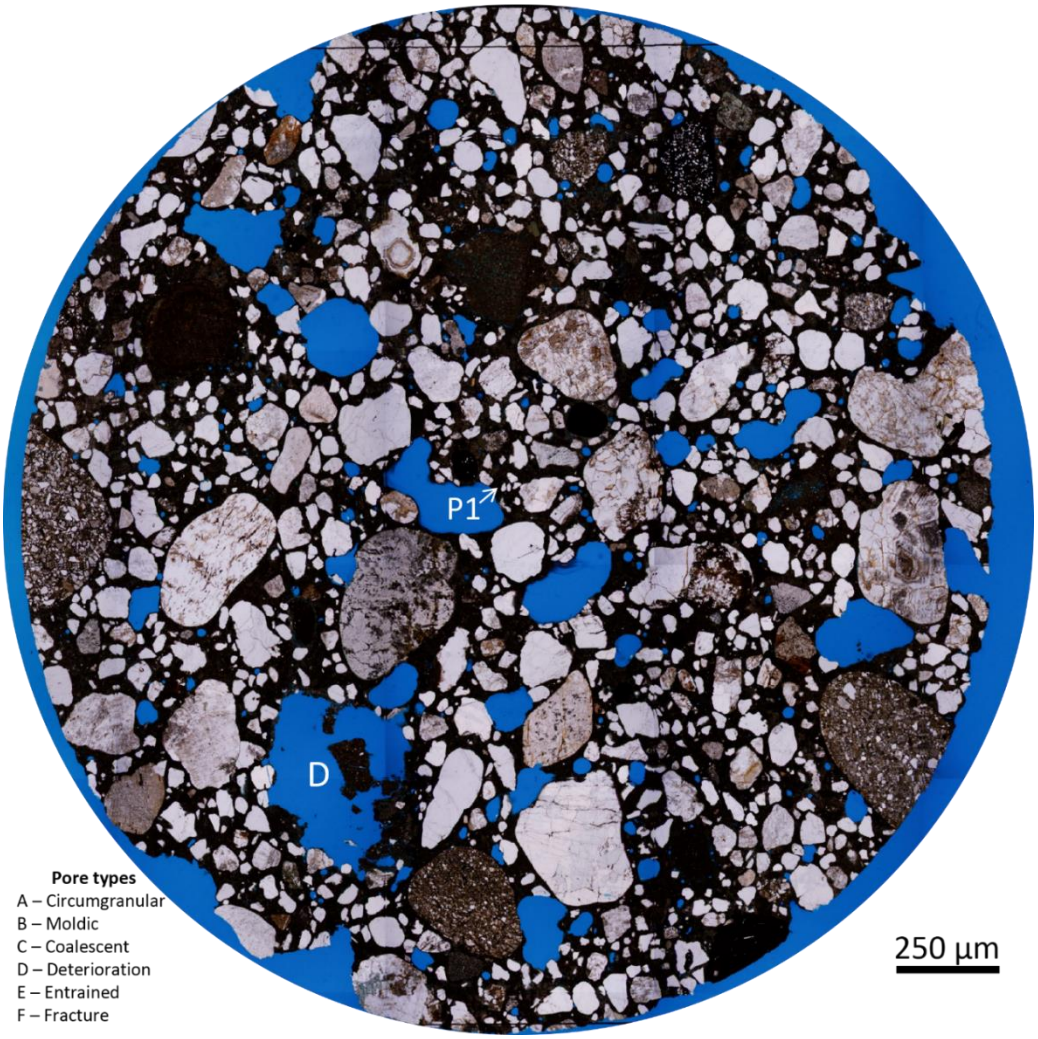

Thin section photomosaic from 1914-Mahaska showing PCC components: CA is absent in this thin section. FA is composed of angular-to-rounded quartz grains as well as of rounded igneous and metamorphic rock fragments. Pores have rounded edges lined with FA. One larger pore is present, suggesting large-scale deterioration of PCC components. Paste is uniformly dark (P1).

Figure 34. Thin section photomosaic from 1914-Mahaska showing PCC components (#3)

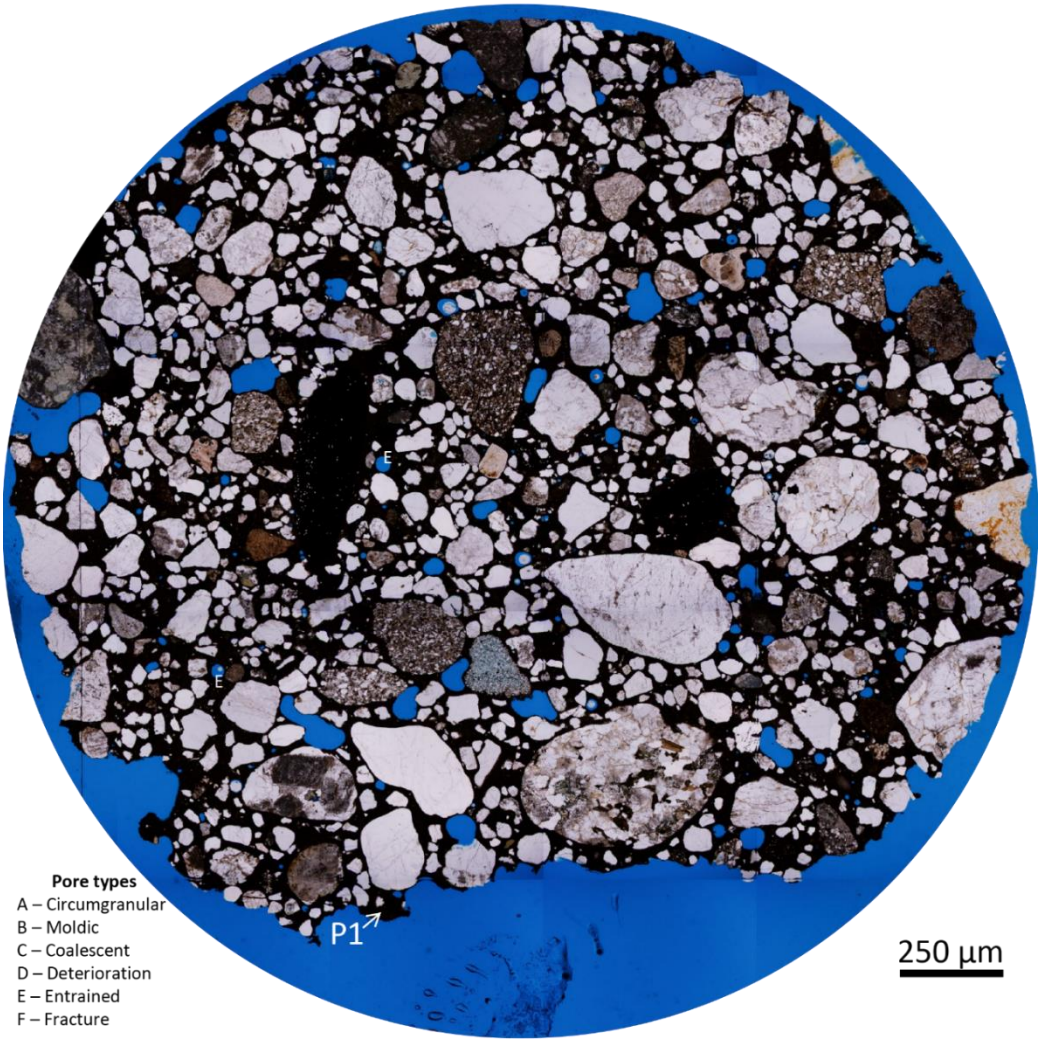

Thin section photomosaic from 1914-Mahaska showing PCC components: CA is absent in this thin section. FA is composed of angular-to-rounded quartz grains as well as of rounded igneous and metamorphic rock fragments. Small pores are circular and larger pores have rounded edges constrained by FA. Paste is uniformly dark (P1).

Figure 35. Thin section photomosaic from 1914-Mahaska showing PCC components (#4)

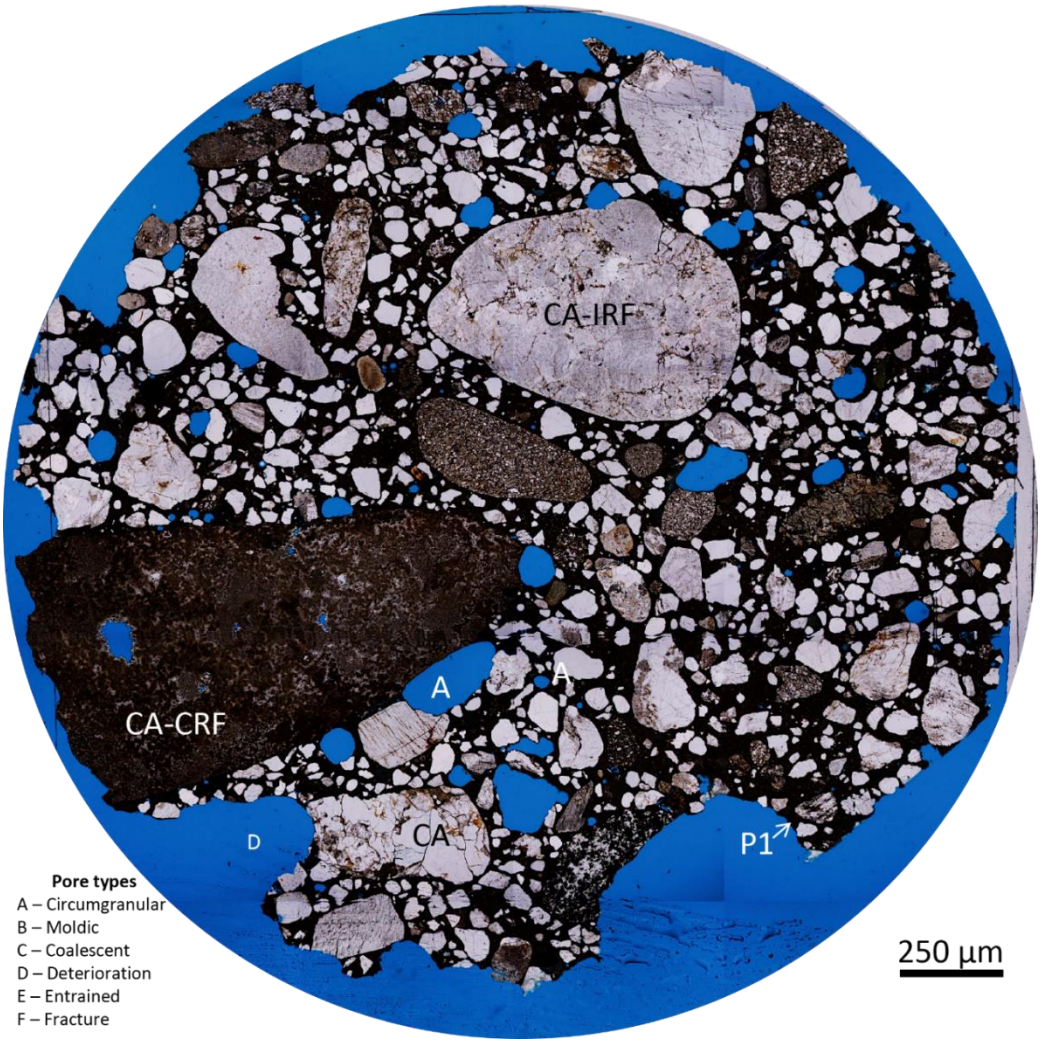

Thin section photomosaic from 1914-Mahaska showing PCC components: CA is composed of a carbonate rock fragment (CRF) and igneous rock fragment (IRF). FA is composed of angular quartz as well as of igneous and metamorphic rock fragments. None of the pores are circular and larger pores have rounded edges lined with FA. Paste is uniformly dark (P1).

Figure 36. Thin section photomosaic from 1914-Mahaska showing PCC components (#5)

1921-Woodbury

The 1921-Woodbury thin sections (Figures 37–41) are similar in composition to 1914-Mahaska but have a greater abundance of CA and more of their CA is non-quartzite rock fragments. Some 1921-Woodbury pores show mineral growth, though this growth is microporous. Evidence was seen in one thin section for "honeycomb pores," likely formed when the PCC was undercompacted. These pores show quartz cement growth predominantly on the bottom of mineral grains, suggesting they were deposited through water films. Most other pores seem similar in size and shape to coarse or fine aggregate grains. Several grains show reaction rims.

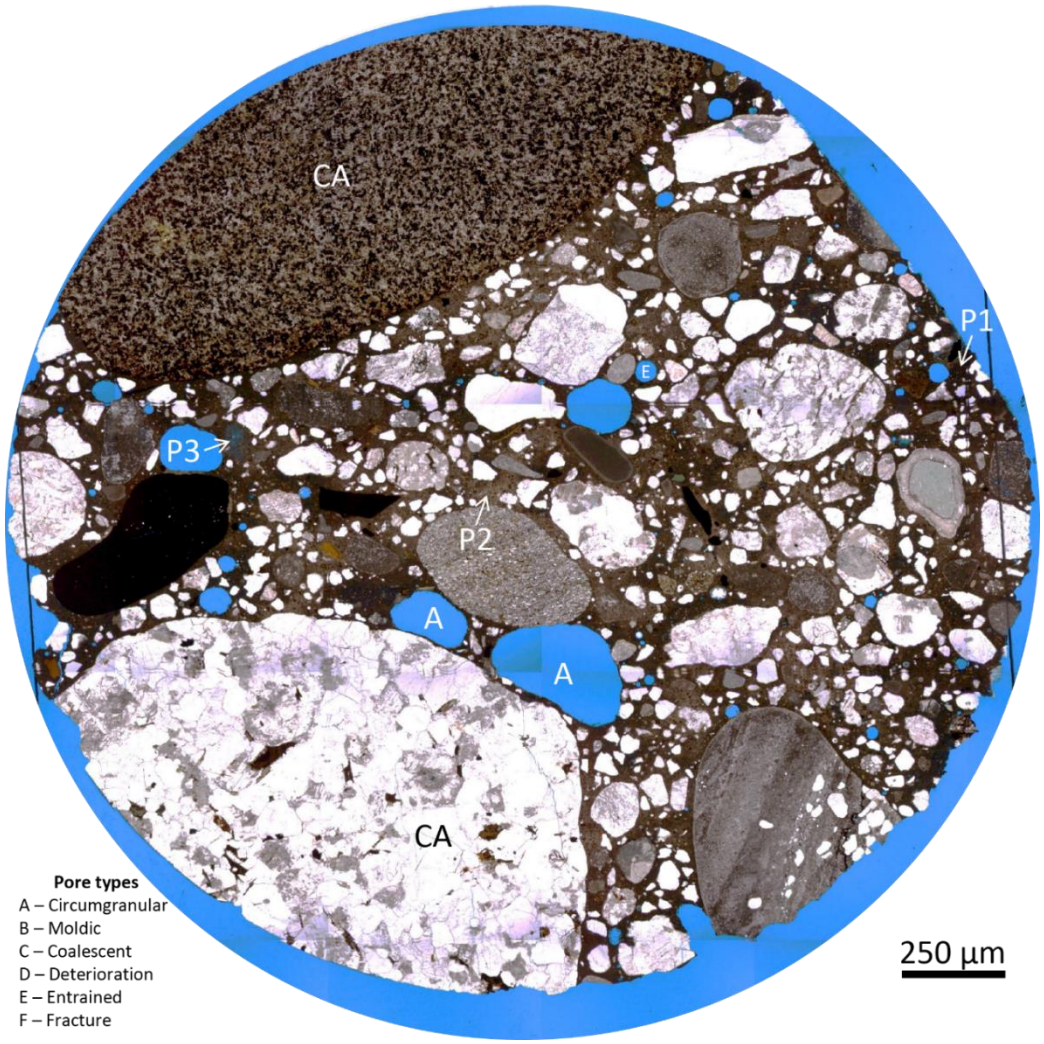

Thin section photomosaic from 1921-Woodbury showing PCC components: CA is composed of two pebbles of igneous rock (one mafic, one felsic). FA is composed of angular quartz as well as of igneous and metamorphic rock fragments. Small pores are circular and larger pores are nearly elliptical or have rounded edges lined with FA. Paste varies from dark (P1) to light (P2) to porous (P3).

Figure 37. Thin section photomosaic from 1921-Woodbury showing PCC components (#1)

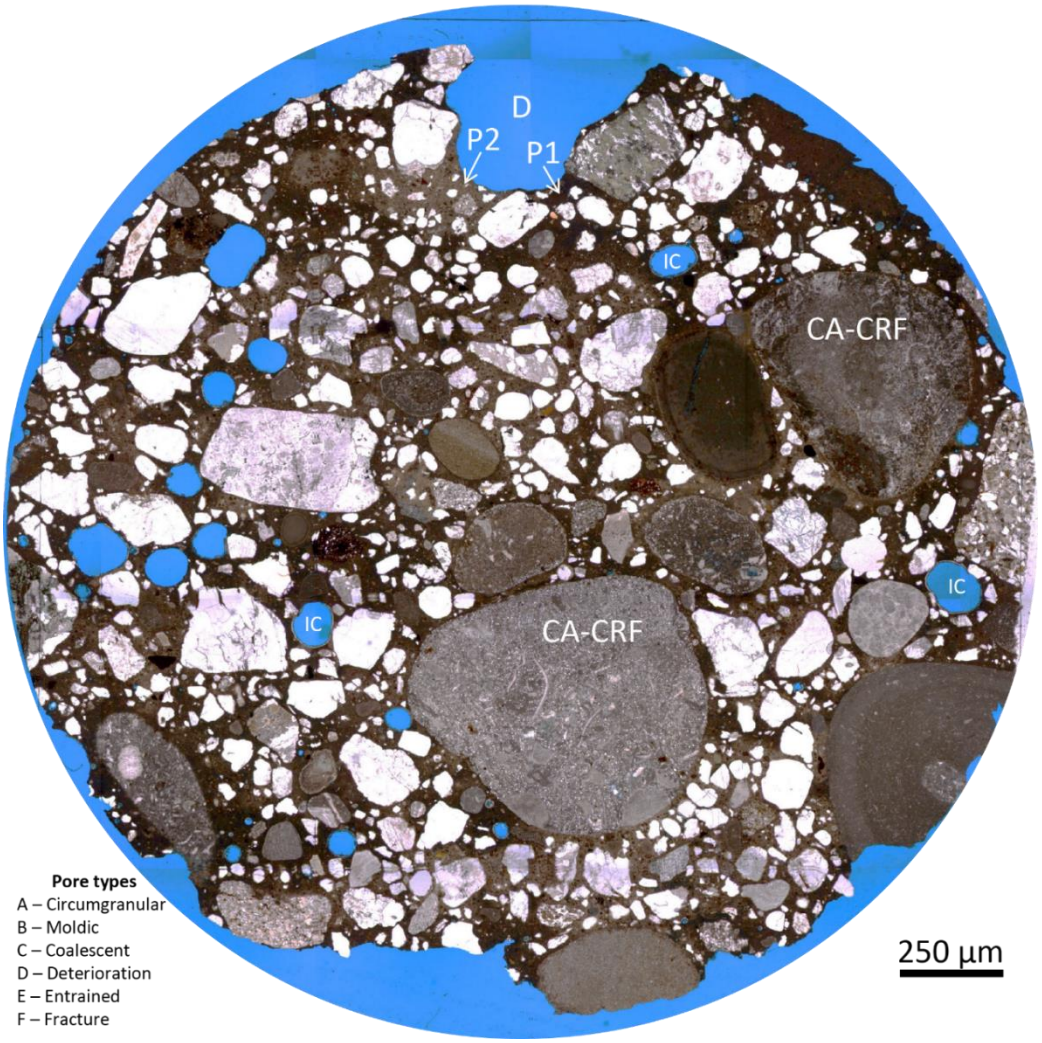

Thin section photomosaic from 1921-Woodbury showing PCC components: CA is composed of carbonate rock fragments (CA-CRF). FA is composed of angular quartz as well as of larger, rounded igneous and metamorphic rock fragments. Most pores are circular, and some pores are lined with isopachous cement (IC, portlandite?). Paste varies from dark (P1) to light (P2).

Figure 38. Thin section photomosaic from 1921-Woodbury showing PCC components (#2)

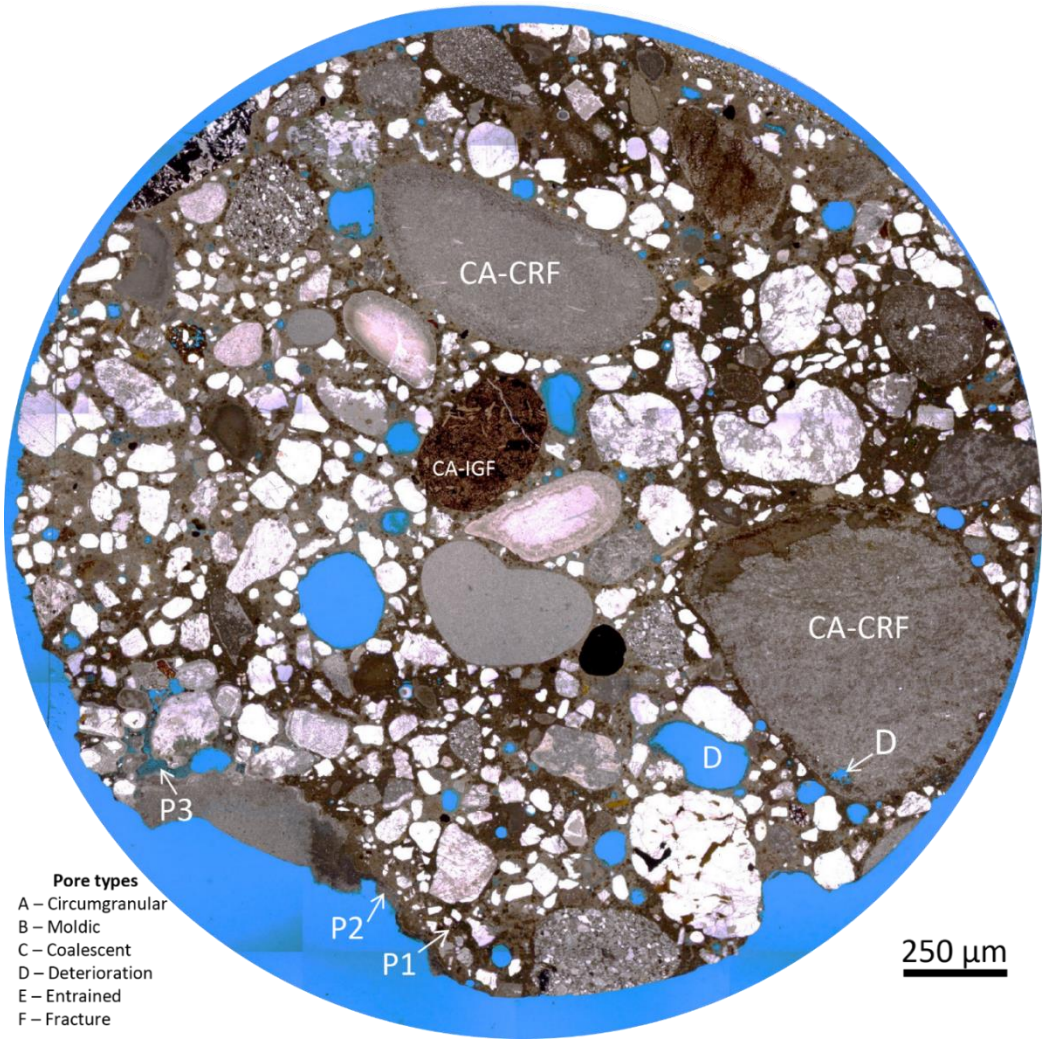

Thin section photomosaic from 1921-Woodbury showing PCC components: CA is composed of igneous (CA-IGF) and carbonate (CA-CRF) rock fragments. FA is composed of angular quartz as well as of larger, rounded igneous and metamorphic rock fragments. Most pores are circular, and some pores are lined with a fringe of porous cement). Paste varies from dark (P1) to light (P2) to porous (P3).

Figure 39. Thin section photomosaic from 1921-Woodbury showing PCC components (#3)

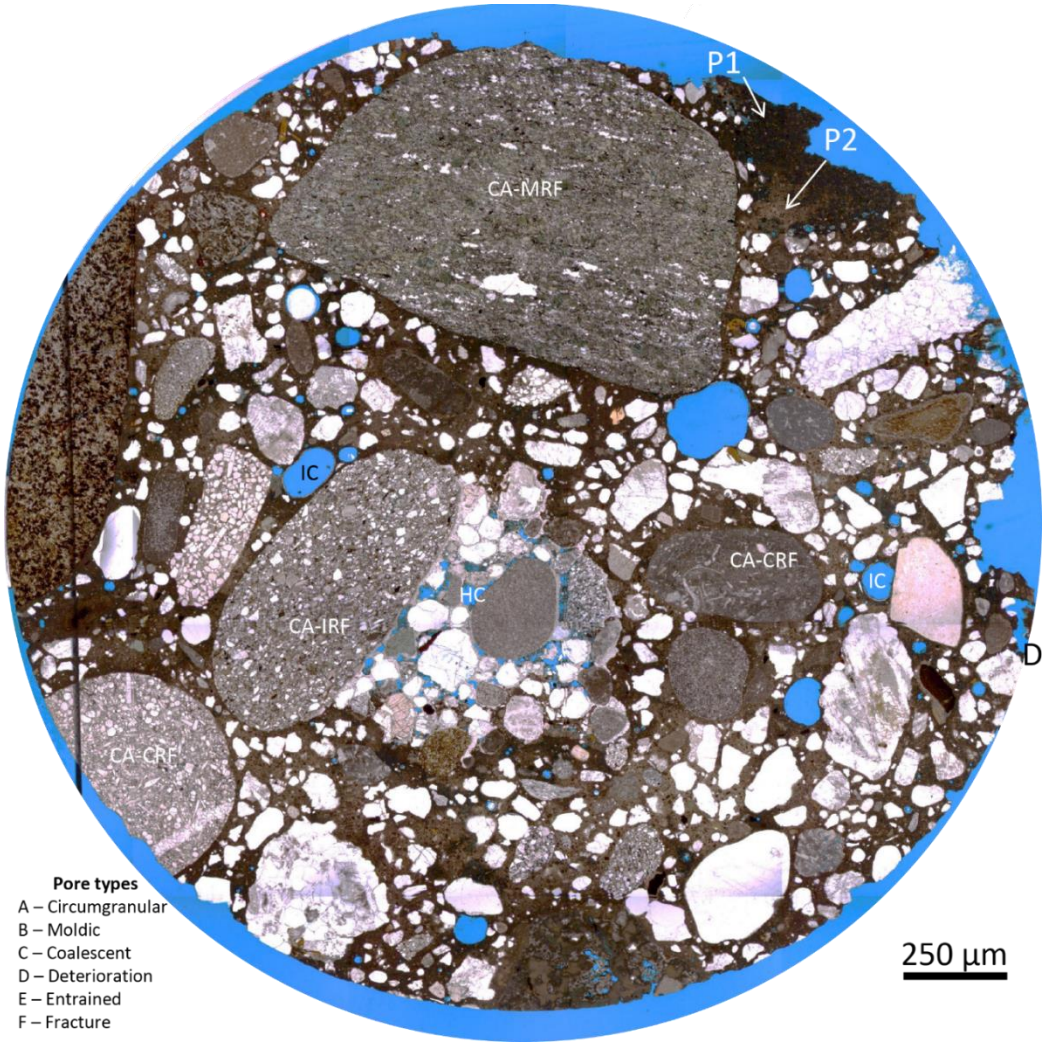

Thin section photomosaic from 1921-Woodbury showing PCC components: CA is composed of igneous (CA-IGF) and carbonate (CA-CRF) rock fragments. FA is composed of angular quartz as well as of larger, rounded igneous and metamorphic rock fragments (CA-MRF). Most pores are circular, and some pores are lined with isopachous cement (IC, portlandite?). A large portion in the center of the image shows "honeycomb cement" where isopachous cement lines all FA grains and there is no paste present. Paste varies from dark (P1) to light (P2).

Figure 40. Thin section photomosaic from 1921-Woodbury showing PCC components (#4)

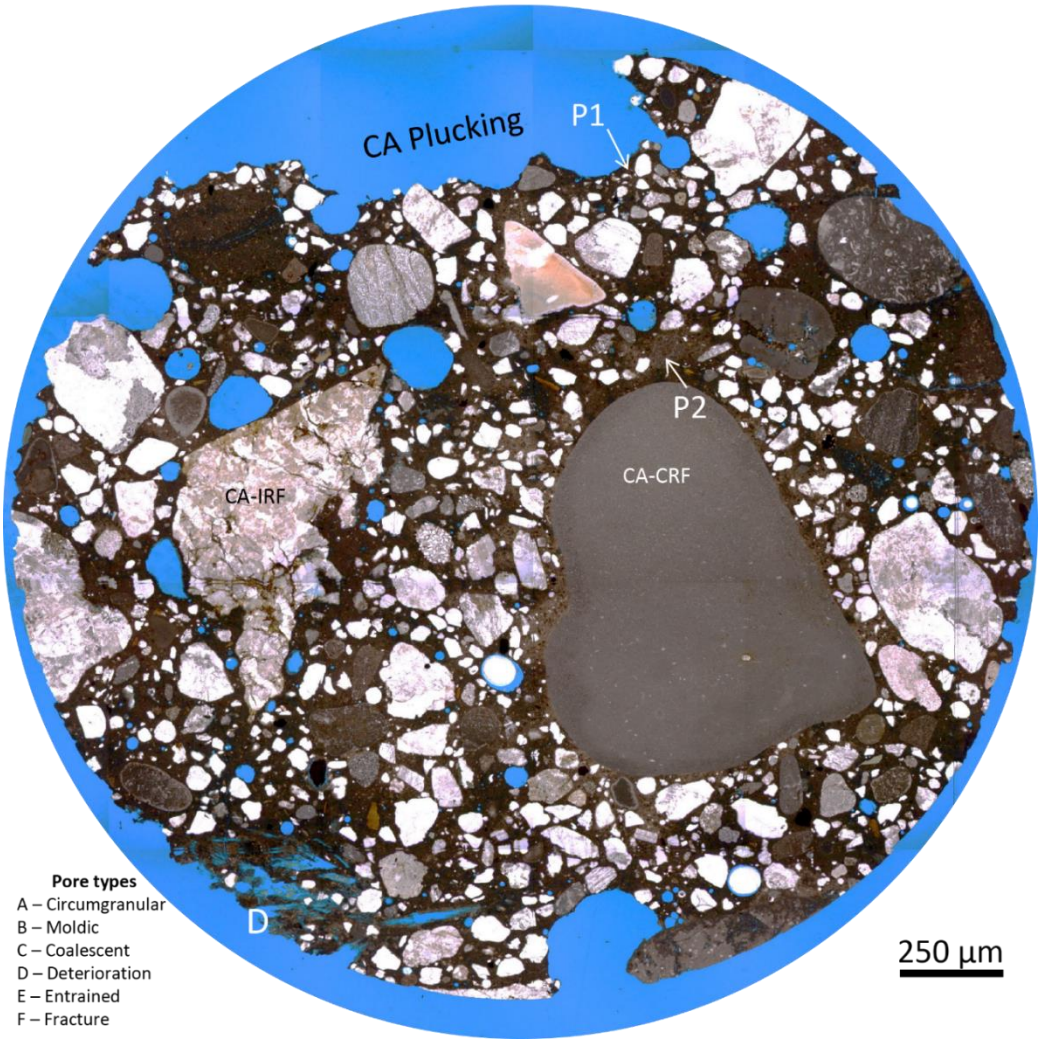

Thin section photomosaic from 1921-Woodbury showing PCC components: CA is composed of igneous (CA-IGF) and carbonate (CA-CRF) rock fragments. FA is composed of angular quartz and larger, rounded igneous and metamorphic rock fragments. Most pores are circular or elliptical. Paste varies from dark (P1) to light (P2).

Figure 41. Thin section photomosaic from 1921-Woodbury showing PCC components (#5)

1929-Wapello

The PCC thin section from 1929-Wapello (Figure 42) is the oldest sample with limestone rock fragments used as CA. These fine-grained limestone rock fragments (CA-LRF) are angular and display common carbonate rock fabric features like lamina and stylolites. The sample's FA is composed mostly of coarse-grained, angular-to-subangular quartz sand with some larger, rounded igneous and metamorphic rock fragments. The paste is in some places highly microporous, yet in other places completely nonporous. Most of the pores in 1929-Wapello have smooth edges and, in at least one case, the boundary of a pore seems to have crosscut the edges of a CA grain, suggestive of dissolution. Some grains show reaction rims.

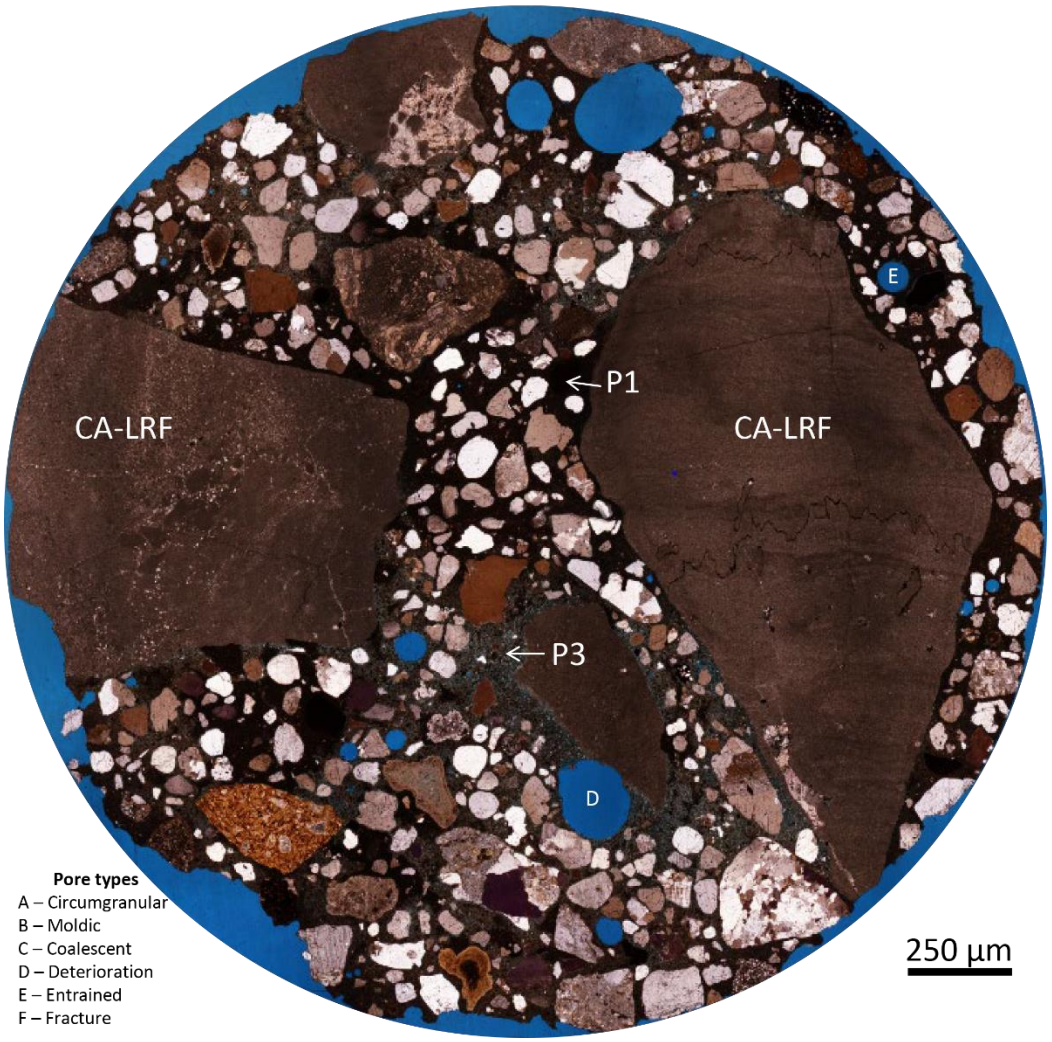

Thin section photomosaic from 1929-Wapello showing PCC components: CA is composed of fine-grained limestone (CA-LRF) rock fragments. FA is composed of angular-to-subangular quartz as well as of larger, rounded igneous and metamorphic rock fragments. Most pores are circular or elliptical, including one that appears to have been entrained (E). In areas where paste is porous, larger pores have irregular edges (D). Paste varies from dark (P1) to porous (P3).

Figure 42. Thin section photomosaic from 1929-Wapello showing PCC components

1938-Monona

The CA in 1938-Monona (Figure 43) is rounded igneous and metamorphic rock fragments. This thin section's CA displays intraparticle porosity as well as fractures. Its FA is angular-to-subrounded coarse-grained quartz sand as well as larger, rounded igneous and metamorphic rock fragments. Its pores display both smooth and irregular boundaries. Its paste is variably microporous. Reaction rims are also present in some of its CA.

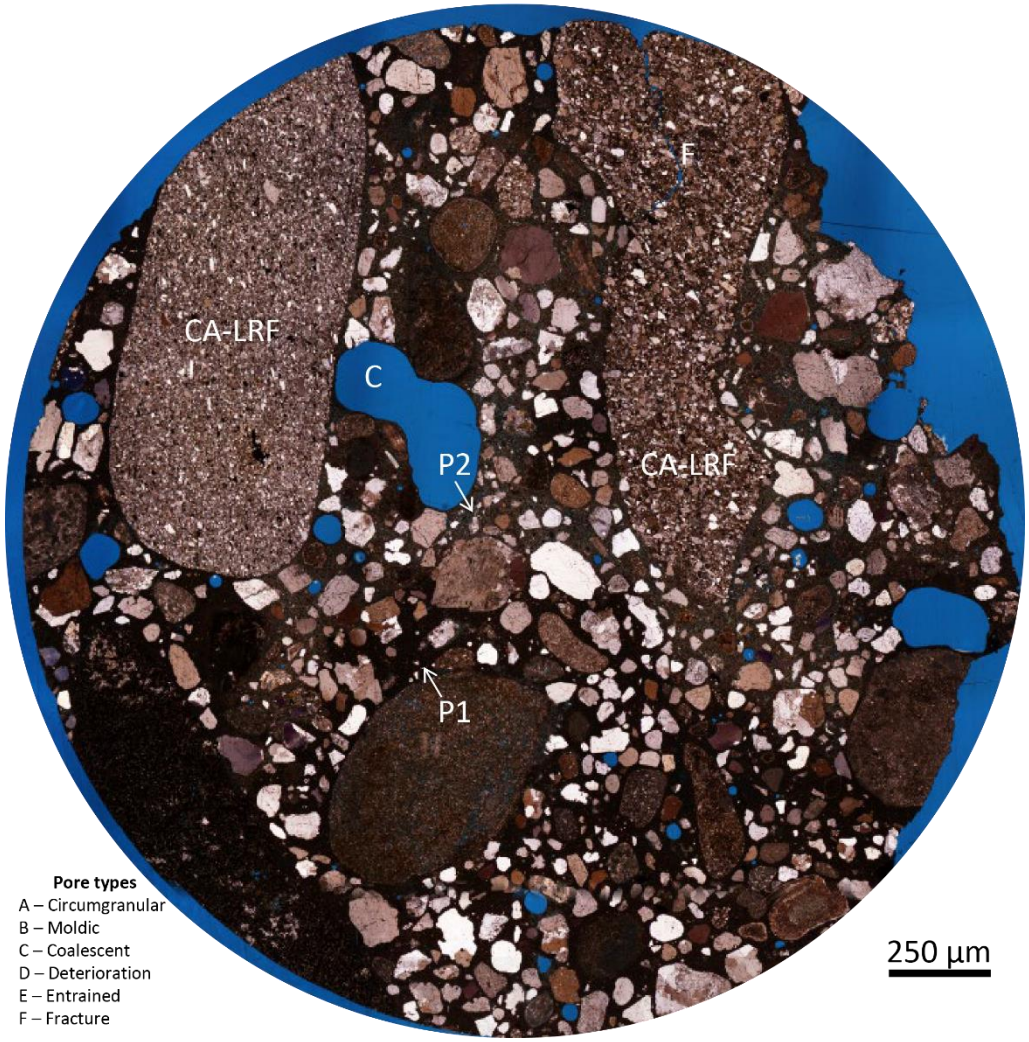

Thin section photomosaic from 1938-Monona showing PCC components: CA is composed of limestone (CA-LRF) rock fragments, one of which is fractured (F). FA is composed of angular-to-subrounded quartz as well as larger, rounded igneous and metamorphic rock fragments. Smaller pores are more circular, while larger pores are elliptical or display irregular, but rounded, forms. One pore appears to be the coalescence of two smaller pores (C). In areas where paste is porous, larger pores have irregular edges. Paste varies from dark (P1) to porous.

Figure 43. Thin section photomosaic from 1938-Monona showing PCC components

1946-Pocahontas

The CA in 1946-Pocahontas (Figure 44) consists of limestone rock fragments (CA-LRF), some displaying intraparticle pores. Its paste is, for the most part, nonporous but in some places microporous areas are present. One CA grain is undergoing mass loss, causing it to detach from its surrounding paste and then fracture. Its pores are both circular and irregular in shape, ranging from 0.25 to 1 mm in diameter. One circular pore has a euhedral mineral growing in it.

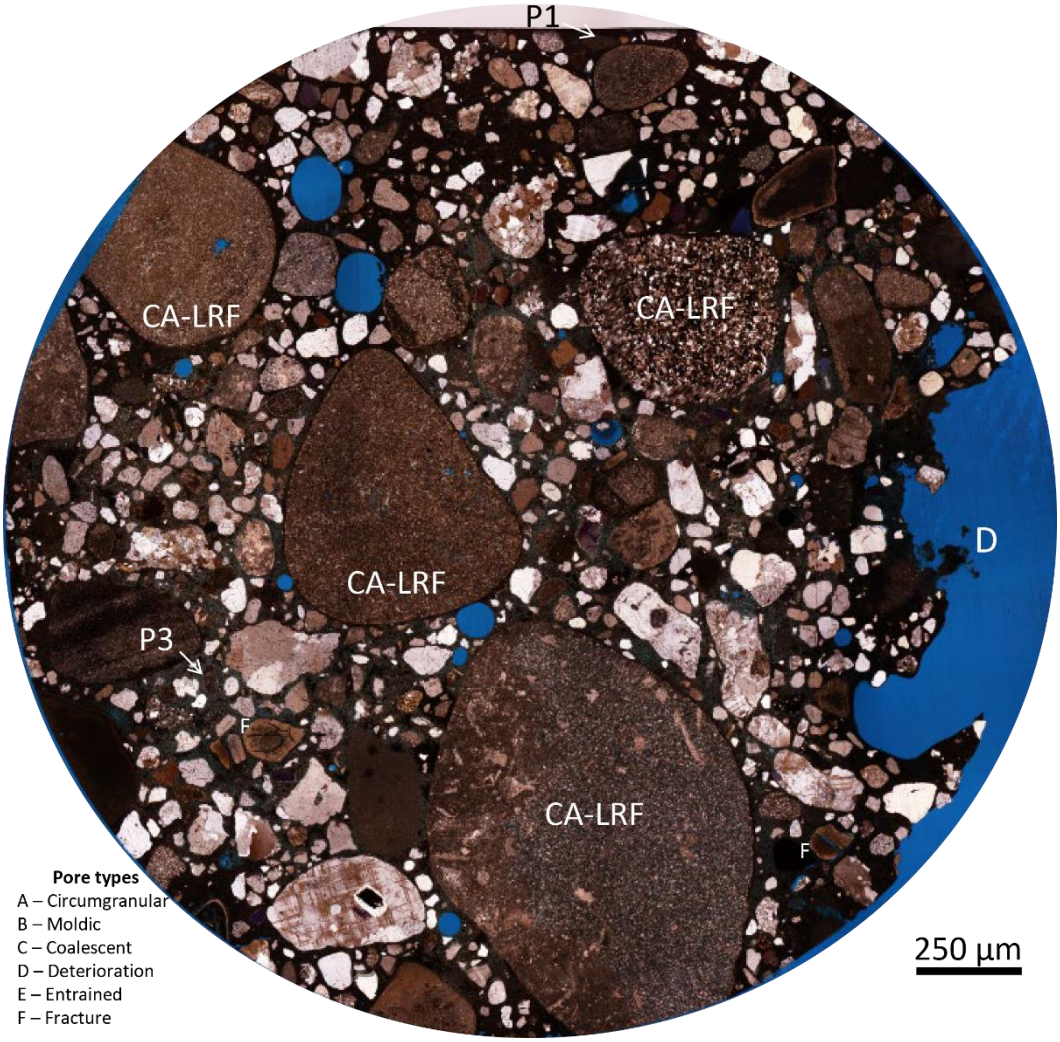

Thin section photomosaic from 1946-Pocahontas showing PCC components: CA is composed of limestone (CA-LRF) rock fragments. FA is composed mostly of angular quartz and larger, rounded igneous and metamorphic rock fragments. Rare shale rock fragments are fractured (F). Smaller pores are more circular while larger pores are elliptical or display irregular, but rounded, forms. The form of one large pore on the edge of the thin section suggests deterioration (D) of the paste and FA. Paste varies from dark (P1) to porous (P3).

Figure 44. Thin section photomosaic from 1946-Pocahontas showing PCC components

1955-Greene

Representing the first sample produced in the era of active air entrainment, it is possible to see remnants of smaller, more circular air voids in 1955-Greene (Figure 45). These pores, however, are mostly filled with a secondary precipitate. The CA in this thin section is composed of quartzite rock fragments that are subrounded and, in the case of the largest one, fractured (F). There are no conjugate margins across the fracture, suggesting some dissolution has occurred. Some small CA lithologies (e.g., shale) are heavily fractured. The FA is mostly coarse-grained, angular quartz sand. Its paste is variably microporous. Reaction rims are present on some of the CA.

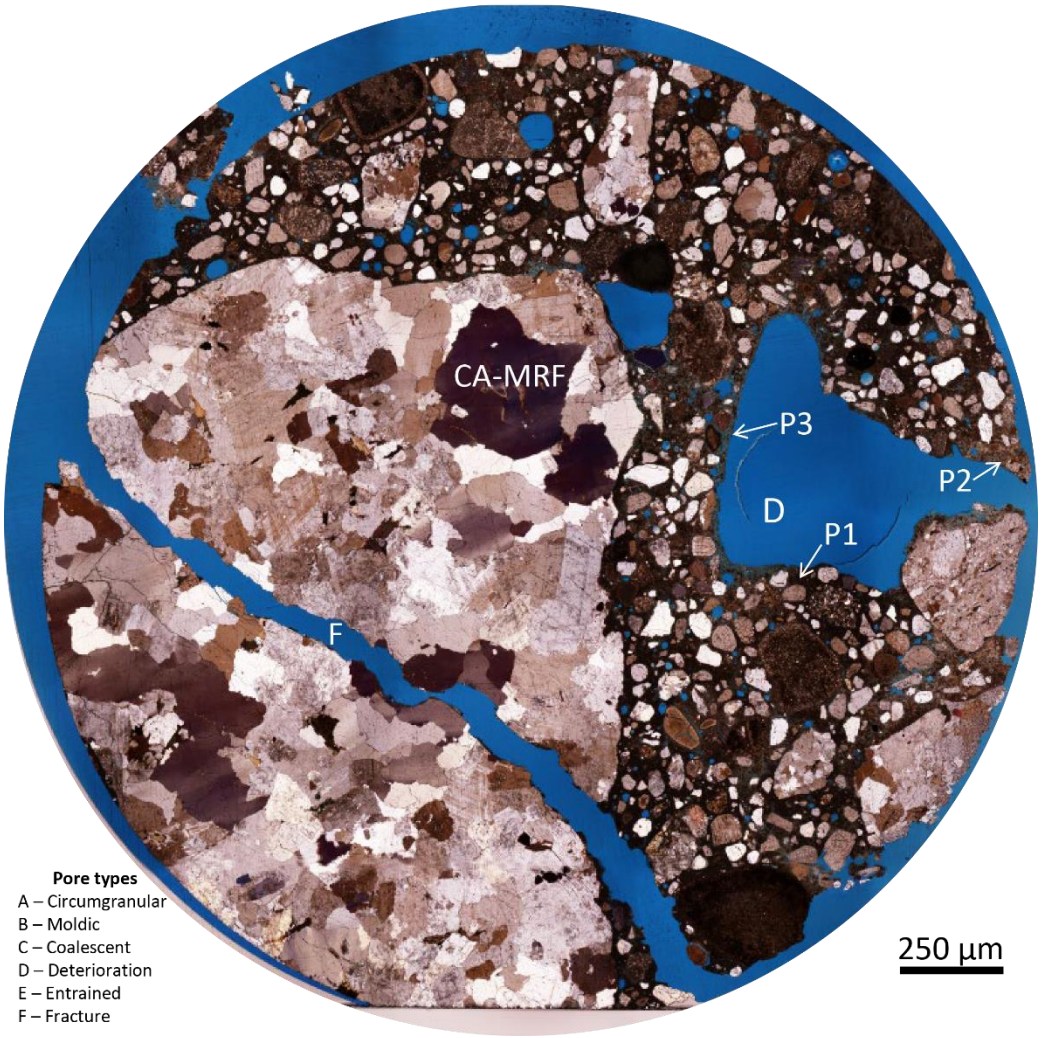

Thin section photomosaic from 1955-Greene showing PCC components: CA is composed of metamorphic (CA-MRF) rock fragments. The large CA-MRF is fractured (F) and this fracture extends into the paste and FA. FA is composed mostly of angular quartz and larger, rounded metamorphic rock fragments. Smaller pores are more circular while larger pores are elliptical or display irregular, but rounded, forms. The form of one large pore on the edge of the thin section suggests deterioration (D) of the paste and FA. Paste varies from dark (P1) to light (P2) to porous (P3).

Figure 45. Thin section photomosaic from 1955-Greene showing PCC components

1963-Marshall

Circular pores from air entrainment are abundant in the paste of 1963-Marshall (Figure 46). The paste itself is variably microporous and hosts other larger, irregularly shaped pores. Its CA is mostly porous, coarse-grained dolostone, with some of the pores appearing to have been widened by dissolution. The FA is coarse-grained angular quartz. Reaction rims are visible on some FA grains.

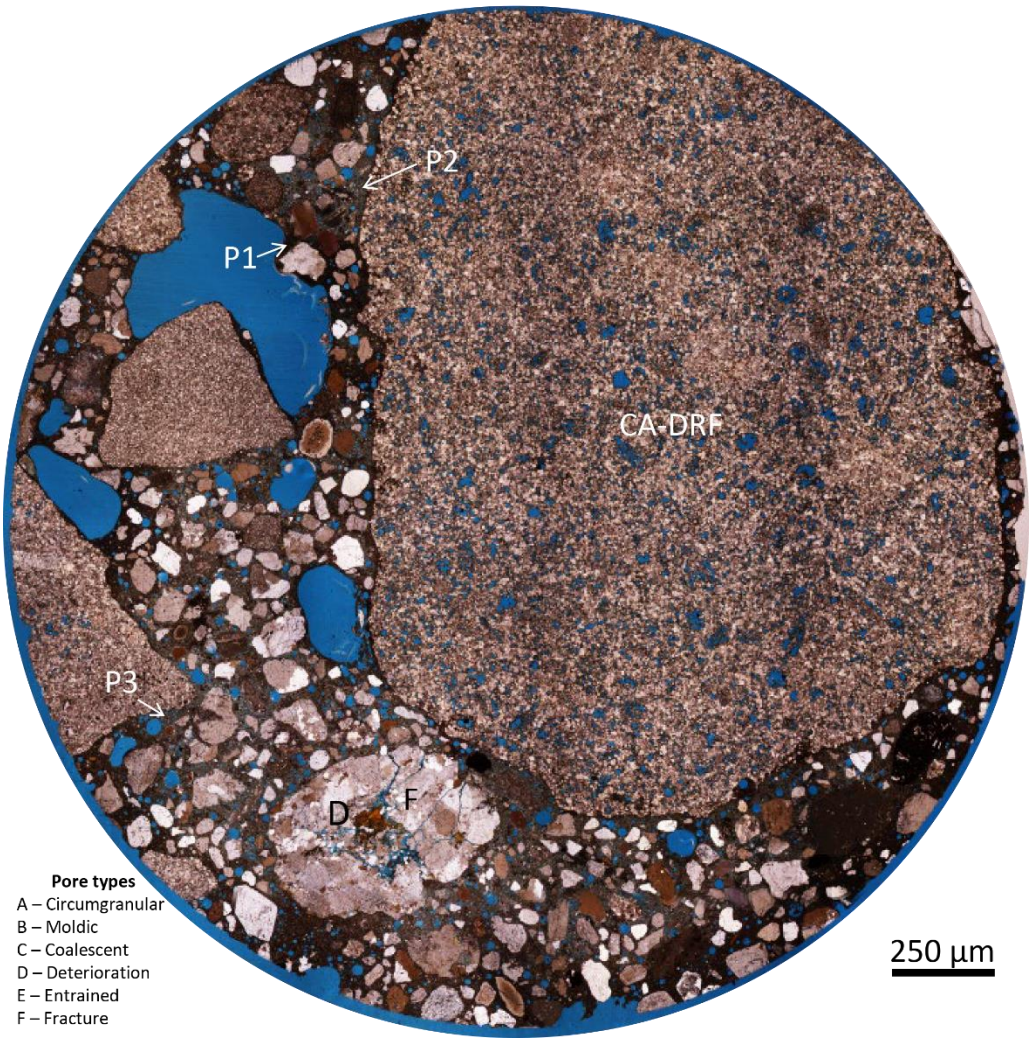

Thin section photomosaic from 1963-Marshall showing PCC components: CA is composed of dolomite (CA-DRF) rock fragments. The large CA-DRF is highly porous with both intercrystalline pores as well as larger vug pores. FA is composed mostly of angular quartz and larger, subrounded metamorphic rock fragments. One large piece of FA, a metamorphic rock fragment, is undergoing deterioration both as fracturing (F) and dissolution (D). Smaller pores are more circular while larger pores are elliptical or display irregular, but rounded, forms. Paste varies from dark (P1) to light (P2) to porous (P3).

Figure 46. Thin section photomosaic from 1963-Marshall showing PCC components

1976-Hamilton

CA in 1976-Hamilton (Figure 47) is composed of limestone rock fragments. The thin section's FA is mostly coarse-grained, subangular quartz sand. The paste appears non-microporous throughout, but it does host circular pores consistent with air entrainment that in some cases show secondary mineral growth.

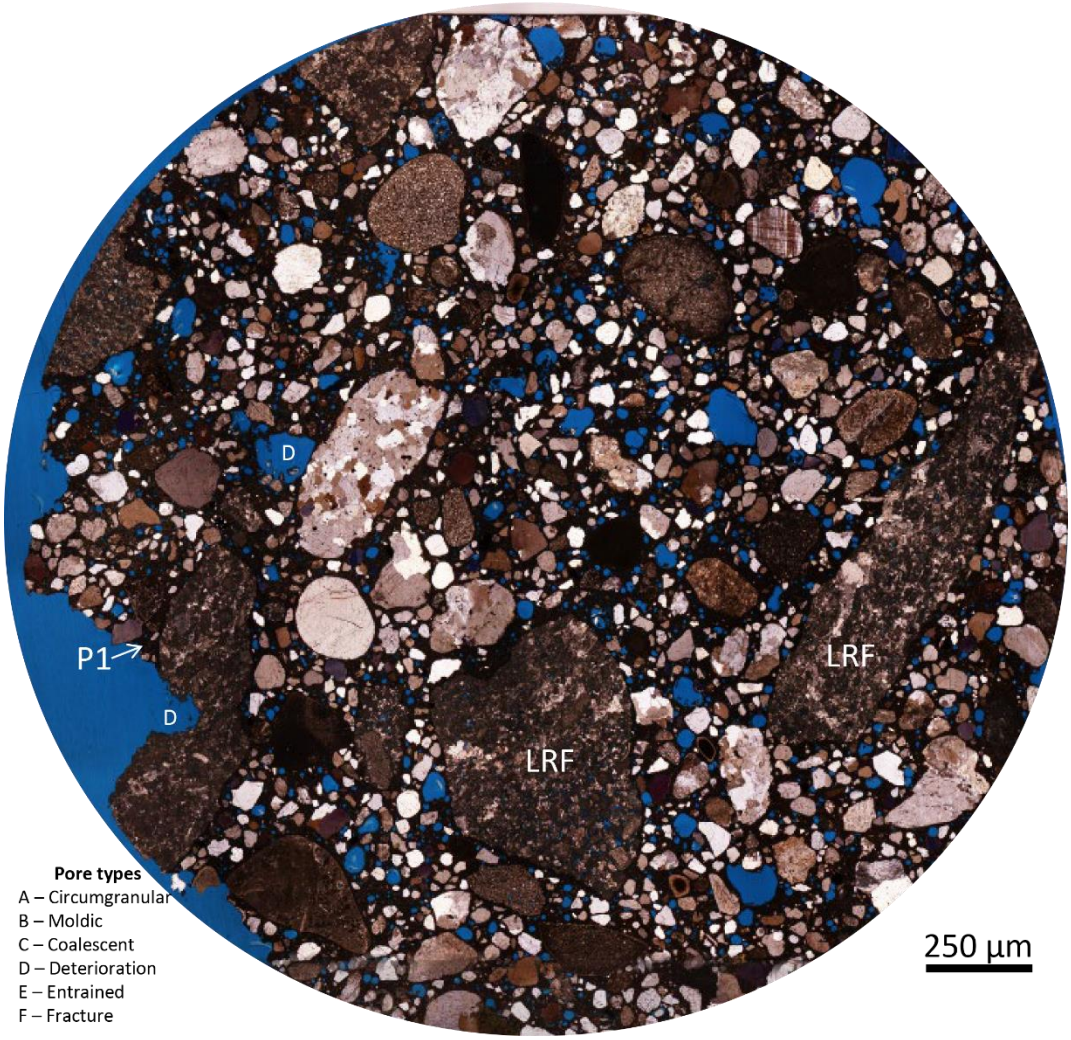

Thin section photomosaic from 1976-Hamilton showing PCC components: CA consists of rather small limestone rock fragments (LRF). One CA grain has a dissolution pit in it (D). FA is composed of subangular quartz and larger, rounded metamorphic rock fragments. Smaller pores are more circular, while larger pores are elliptical or display irregular forms. Paste is uniformly dark (P1).

Figure 47. Thin section photomosaic from 1976-Hamilton showing PCC components

1980-Boone

The CA in 1980-Boone (Figure 48) is composed of quartzite and other igneous and metamorphic rock fragments. Some fine-grained rock fragments are undergoing dissolution and fracturing that is causing the CA to pull away from the surrounding paste. The FA is mostly coarse- to very-coarse-grained, subangular quartz sand. The paste appears non-microporous throughout, but it does host smaller circular pores consistent with air entrainment that in some cases host minor secondary mineral growth.

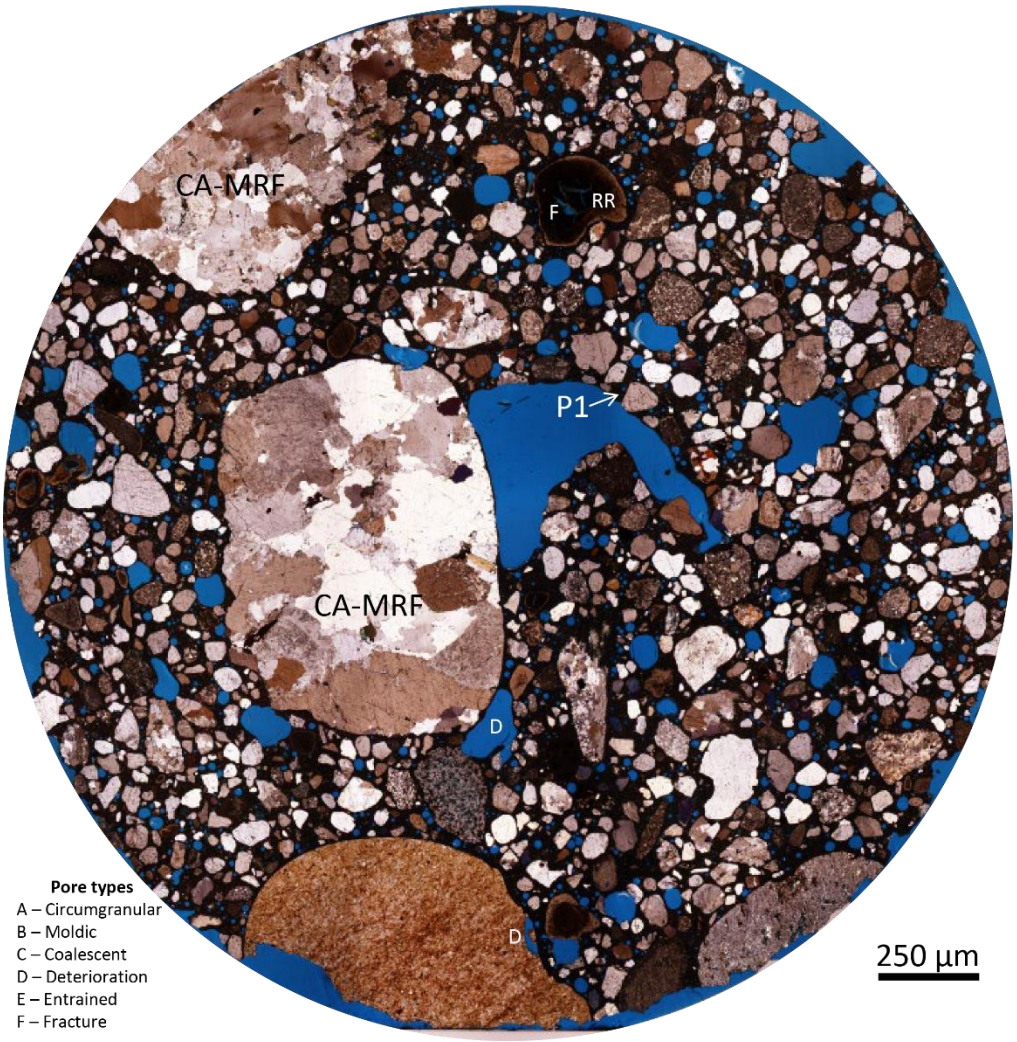

Thin section photomosaic from 1980-Boone showing PCC components: CA is composed of metamorphic rock fragments (CA-MRF). FA is composed of smaller, subangular quartz and larger, rounded metamorphic and carbonate rock fragments. Shale FA shows signs of deterioration such as reaction rims (RR) and fractures (F). Smaller pores are more circular while larger pores are elliptical or display irregular, but rounded, forms. In areas where paste is porous, larger pores have irregular edges (D). Paste is uniformly dark (P1).

Figure 48. Thin section photomosaic from 1980-Boone showing PCC components

1997-Linn

The CA in 1997-Linn (Figure 49) is composed of mostly porous, fine-grained dolostones. The FA in 1997-Linn consists mostly of coarse- to very-coarse-grained quartz sand with some lithic rock fragments. The thin section's paste appears uniformly non-microporous. Smaller, more circular pores consistent with air entrainment are visible with rare signs of secondary mineral growth. Larger pores that are more irregularly shaped are also present.

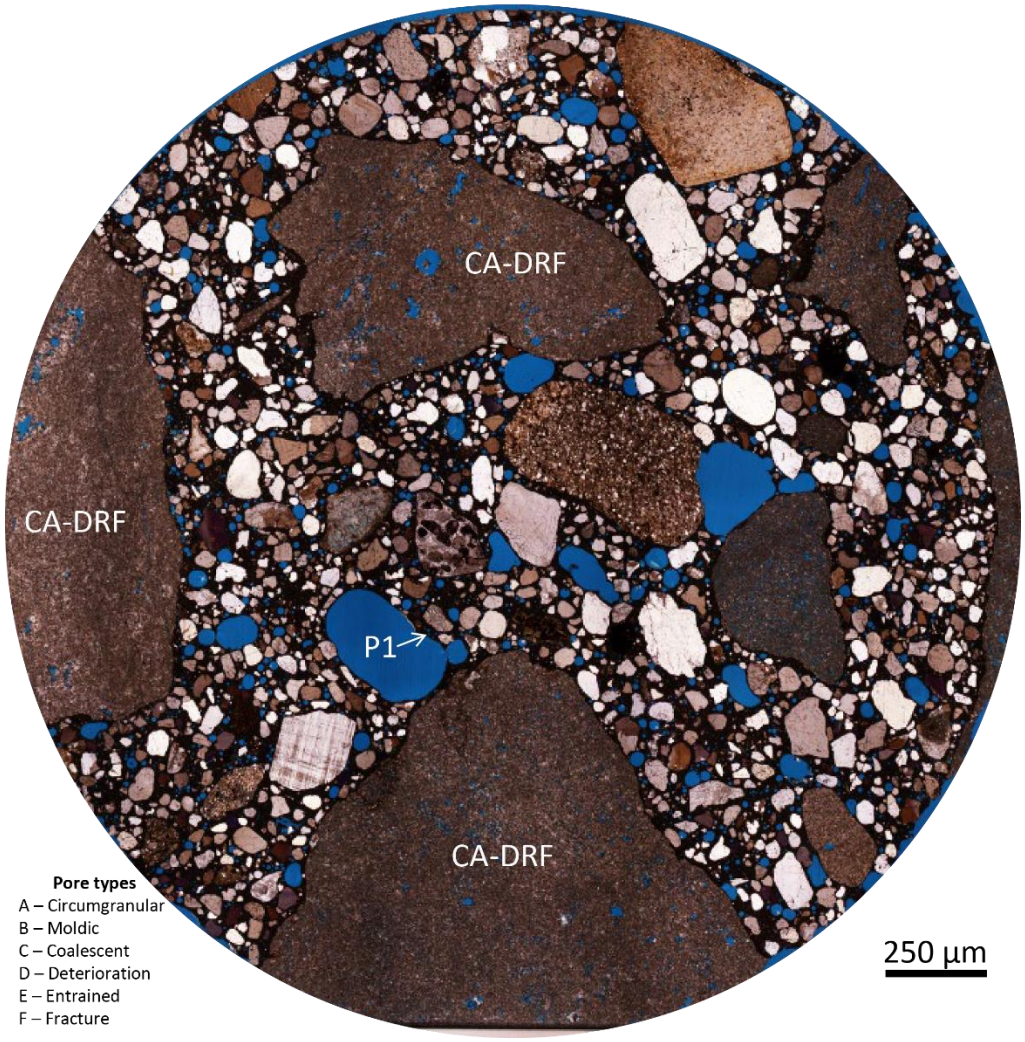

Thin section photomosaic from 1997-Linn showing PCC components: CA is composed of dolomite (CA-DRF) rock fragments. The large CA-DRFs are highly porous with both intercrystalline pores as well as larger vug pores. FA is composed mostly of smaller, angular quartz and larger, subrounded metamorphic rock fragments. Smaller pores are more circular, while larger pores are elliptical or display irregular, but rounded, forms. Paste is uniformly dark (P1).

Figure 49. Thin section photomosaic from 1997-Linn showing PCC components

1999-Story

In 1999-Story (Figures 50–52), thin-sectioning revealed its FA consists of angular, coarse-grained quartz sand to quartz pebbles. The sample's paste is variably microporous. Deterioration of some of the FA (shale?) in 1999-Story is evidenced through both dissolution and fracture fabrics. This deterioration has made the FA partially detach from the paste matrix. Circular pores consistent in size and shape with air entrainment are present. Larger, more irregularly shaped pores are also present, some with geopetal fillings of mineral precipitates.

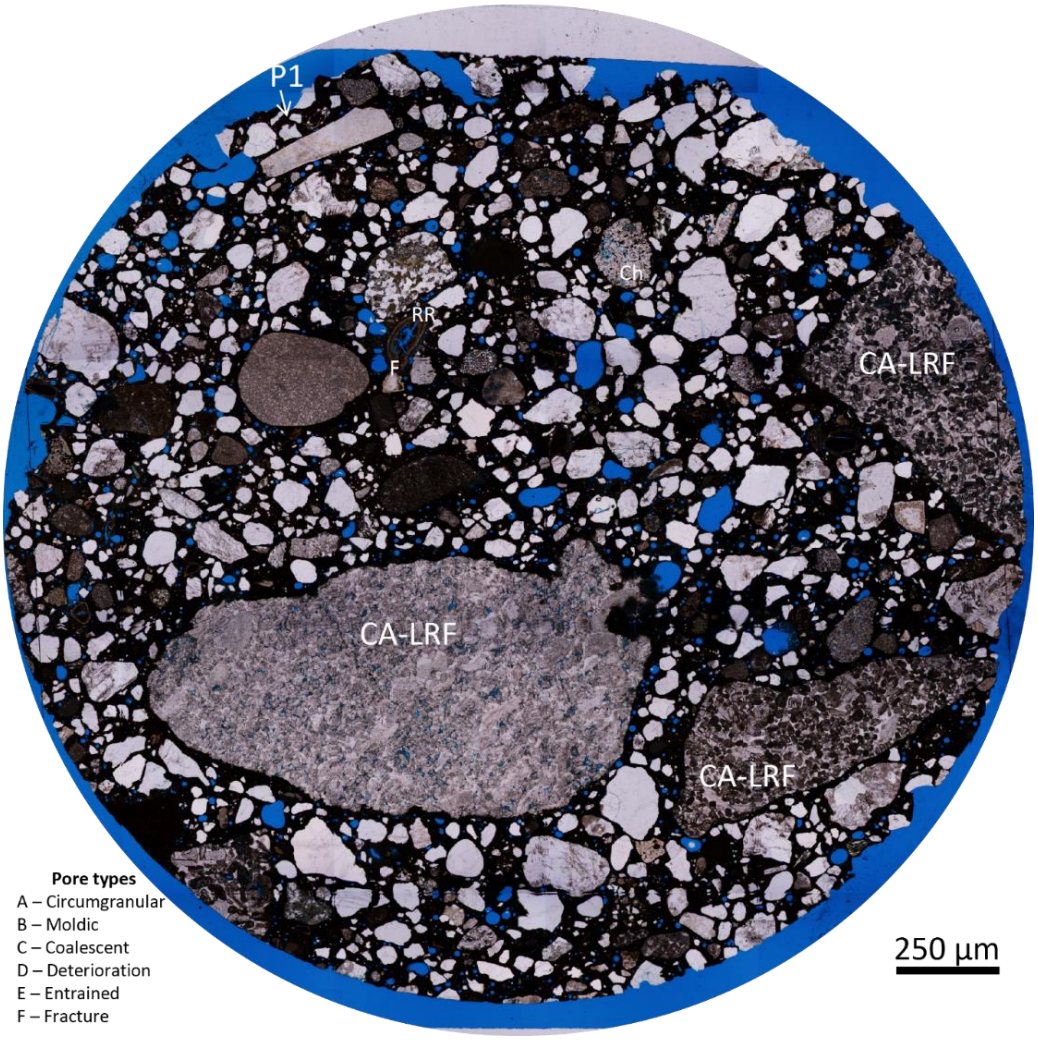

Thin section photomosaic from 1999-Story showing PCC components: CA is composed of coarse-grained limestone rock fragments (CA-LRF), specifically lime grainstones. FA is composed of angular quartz and larger, rounded rock fragments, including porous chert (Ch). Shale FA shows signs of deterioration, such as reaction rims (RR) and fractures (F). Most pores are circular or elliptical. Paste is uniformly dark (P1).

Figure 50. Thin section photomosaic from 1999-Story showing PCC components (#1)

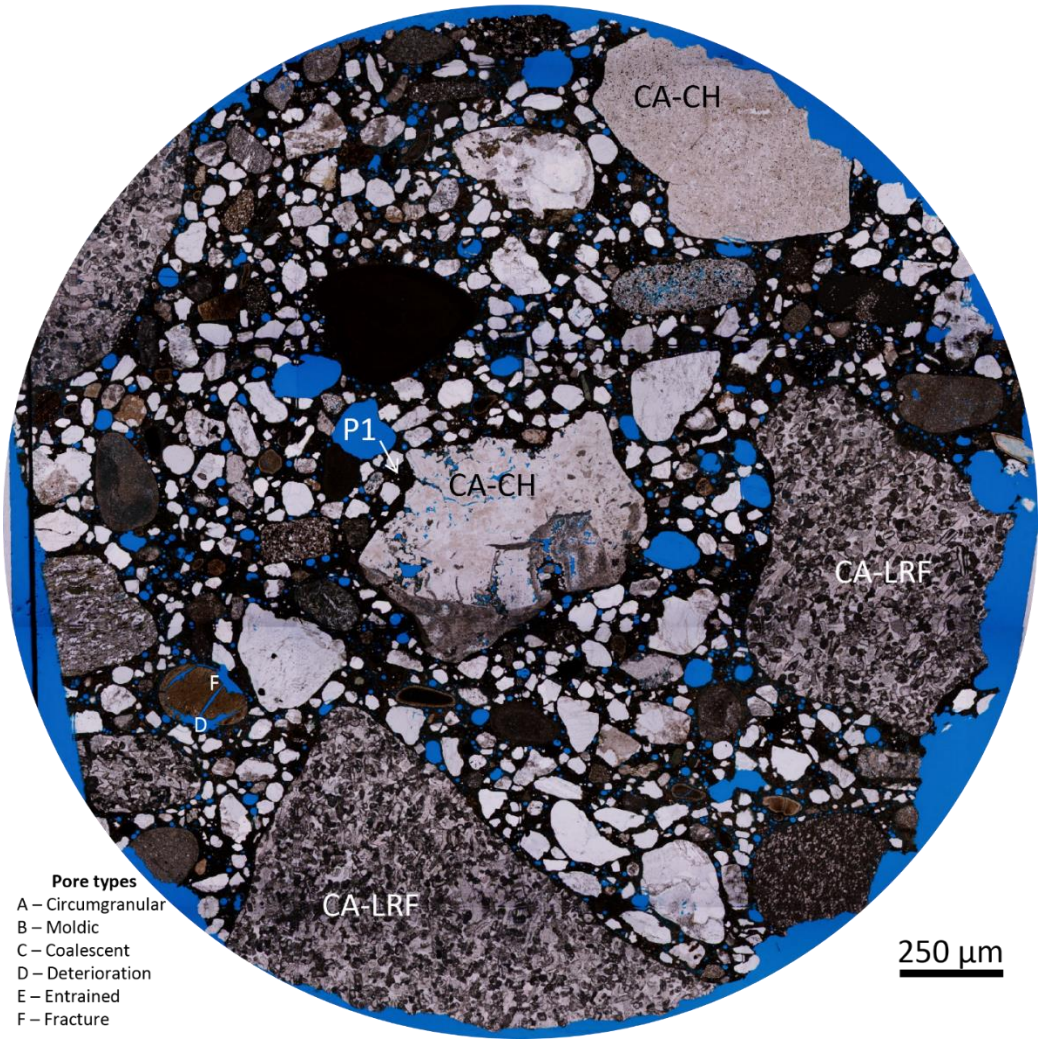

Thin section photomosaic from 1999-Story showing PCC components: CA is composed of coarse-grained limestone rock fragments (CA-LRF), specifically skeletal lime grainstones, and chert (CA-CH). FA is composed of angular quartz and larger, rounded rock fragments. Shale FA shows signs of deterioration, such as fractures (F). Most pores are circular or elliptical. In areas where paste is porous, larger pores have irregular edges (D). Paste is uniformly dark (P1).

Figure 51. Thin section photomosaic from 1999-Story showing PCC components (#2)

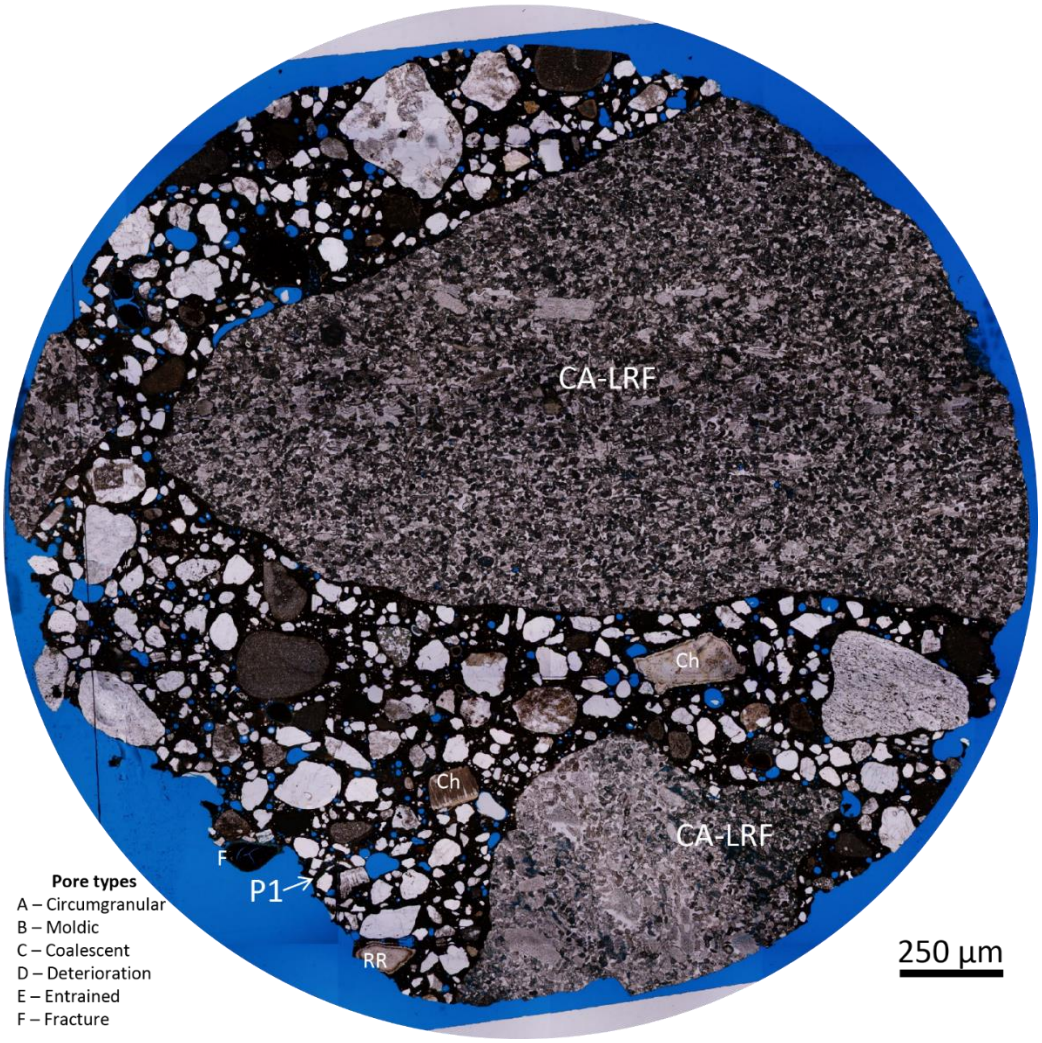

Thin section photomosaic from 1999-Story showing PCC components: CA is composed of coarse-grained limestone rock fragments (CA-LRF), specifically skeletal lime grainstones. FA is composed of angular quartz and larger, rounded rock fragments, including chert (Ch). Shale FA shows signs of deterioration, such as fractures (F) and reaction rims (RR). Most pores are circular or elliptical. Paste is uniformly dark (P1).

Figure 52. Thin section photomosaic from 1999-Story showing PCC components (#3)

2002-Jones

In 2002-Jones (Figure 53), the CA is mostly porous, coarse-grained dolostone, similar to 1963-Marshall (previous Figure 46), with some of the pores appearing to have been widened by dissolution. A euhedral dolomite rhomb is present in one pore within a CA grain, suggesting mineral precipitation. Air-entrainment pores are also present. Some larger pores (similar in size to FA) are filled with a mesh of mineral matter likely precipitated in the pore.

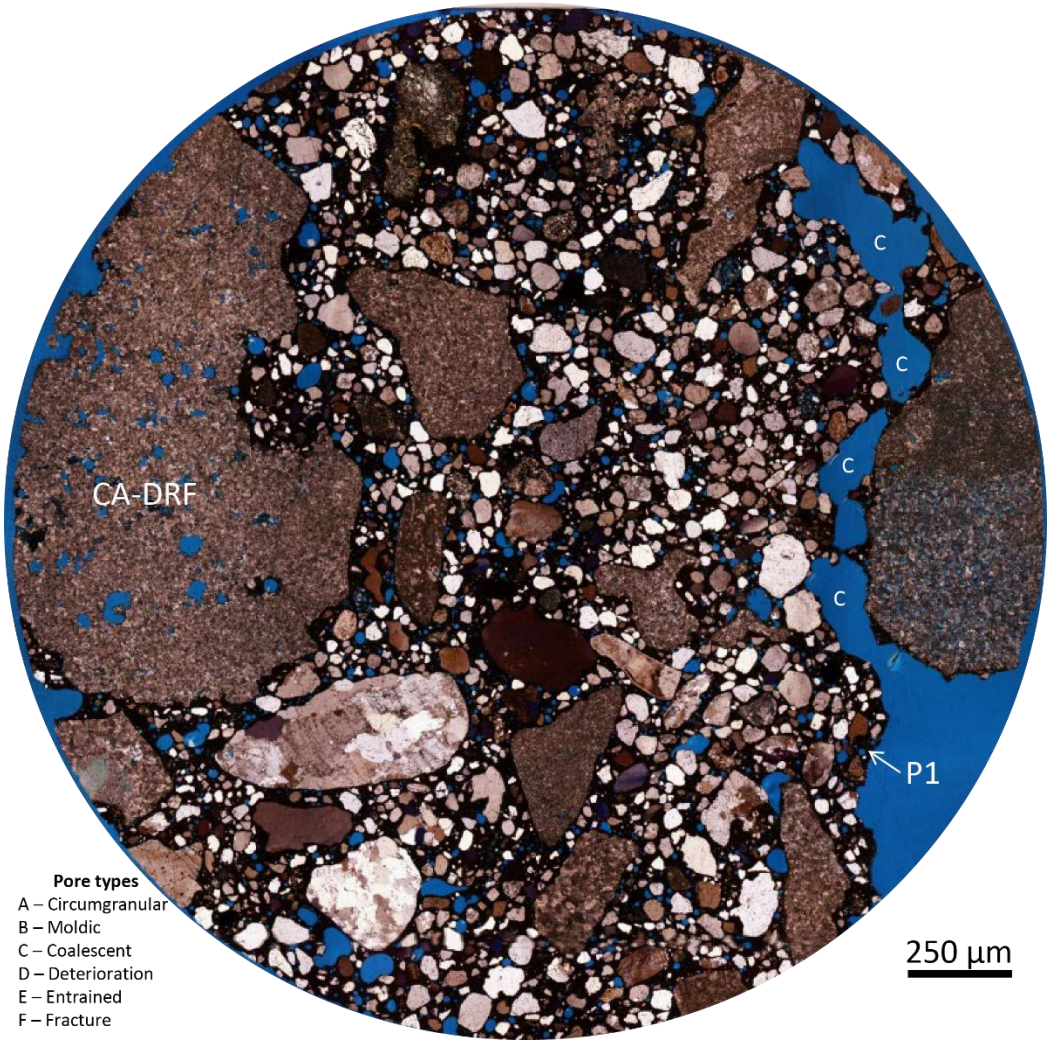

Thin section photomosaic from 2002-Jones showing PCC components: CA is composed of dolomite rock fragments (CA-DRF). The large CA-DRF is highly porous with both intercrystalline pores as well as larger vug pores. FA is composed mostly of smaller, angular quartz and larger, subrounded metamorphic rock fragments. Smaller pores are more circular, while larger pores are elliptical or display irregular, but rounded, forms. In one part of the thin section, circumgranular pores are coalescing (C) around a CA fragment. Paste is uniformly dark (P1).

Figure 53. Thin section photomosaic from 2002-Jones showing PCC components

Thin Section Imaging—Deterioration Features

Close-up images of certain features were captured from each thin section. These images document changes in pore shape, cementation in pores, CA and FA deterioration, as well as fracturing in the paste. A representative photomicrograph was taken from each thin section. Figures are laid out to show either each sample's representative thin section or a blank space indicating that a given feature was not observed in that particular sample's thin section. Figures 54-70 are all at the same scale (scale bar = 200 µm) and Figures 70-75 are at a similarly uniform, but finer, scale (scale bar = 100 µm).

Paste

Paste from the pre-1960 samples (Figure 54) is noticeably more mottled in appearance due to more abundant lighter-colored cement than is observed in post-1960 samples (Figure 55). This lighter-colored cement (P2) appears to be nonporous, whereas the darker-colored cement (P1) that was found in all thin sections is characterized by abundant micropores. Rarely, a third type of paste was observed (P3), which is highly macroporous (previous Figure 23E).

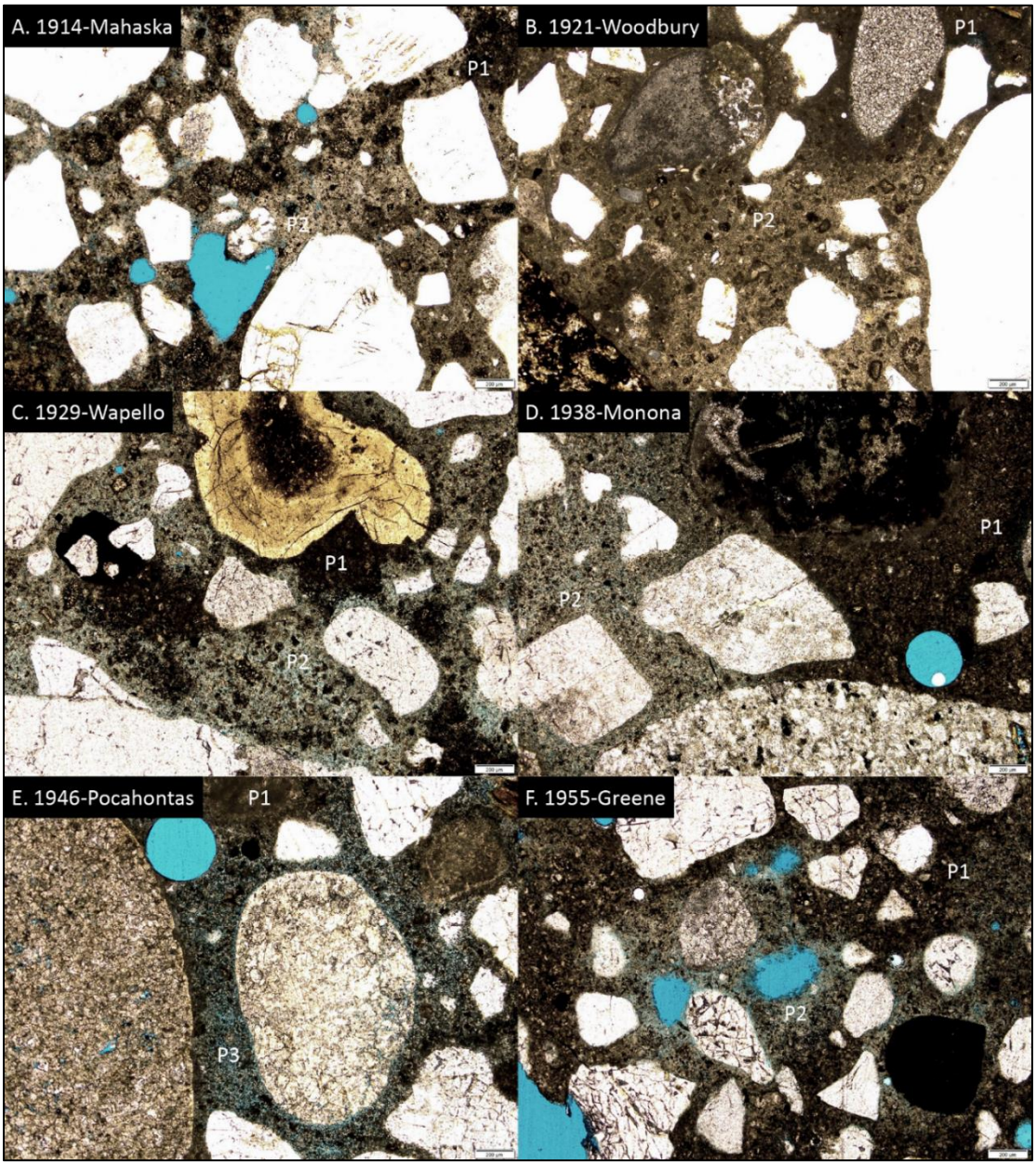

*Photomicrographs of paste from samples **before** 1960: Images show "P1" paste (dark), "P2" paste (light), and "P3" paste (blue-tinted). Scale bar is 200 µm in all images.*

Figure 54. Photomicrographs of paste from samples *before* 1960

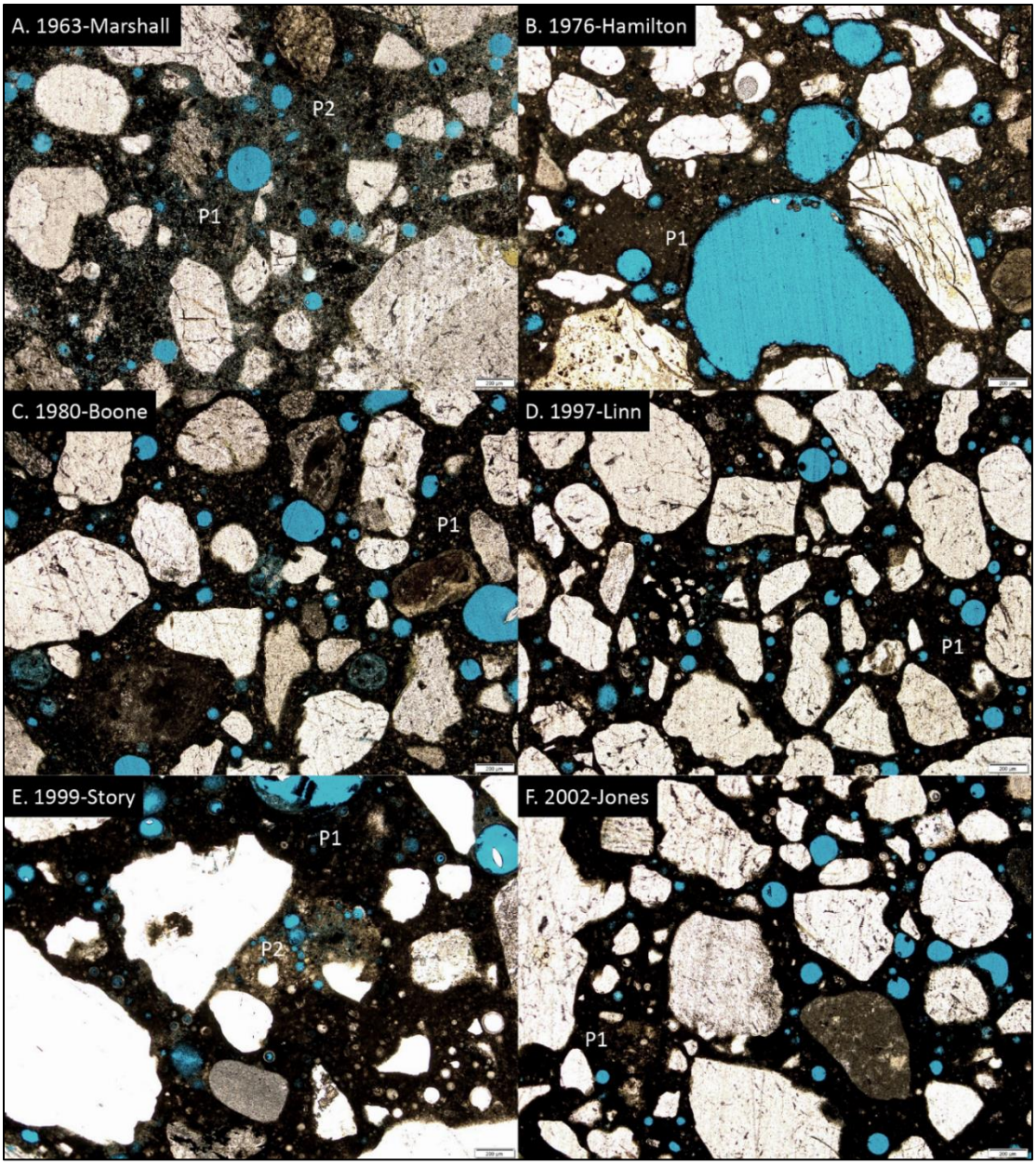

*Photomicrographs of paste from samples **after** 1960: Images show "P1" paste (dark), "P2" paste (light), and "P3" paste (blue-tinted) that is only visible in voids filled with debris. Scale bar is 200 µm in all images.*

Figure 55. Photomicrographs of paste from samples *after* 1960

Pores

For all thin sections, abundant circular to irregular pores were observed (Figures 56 and 57). Smaller pores tend to be more circular, whereas larger pores tend to be more irregular in their perimeter.

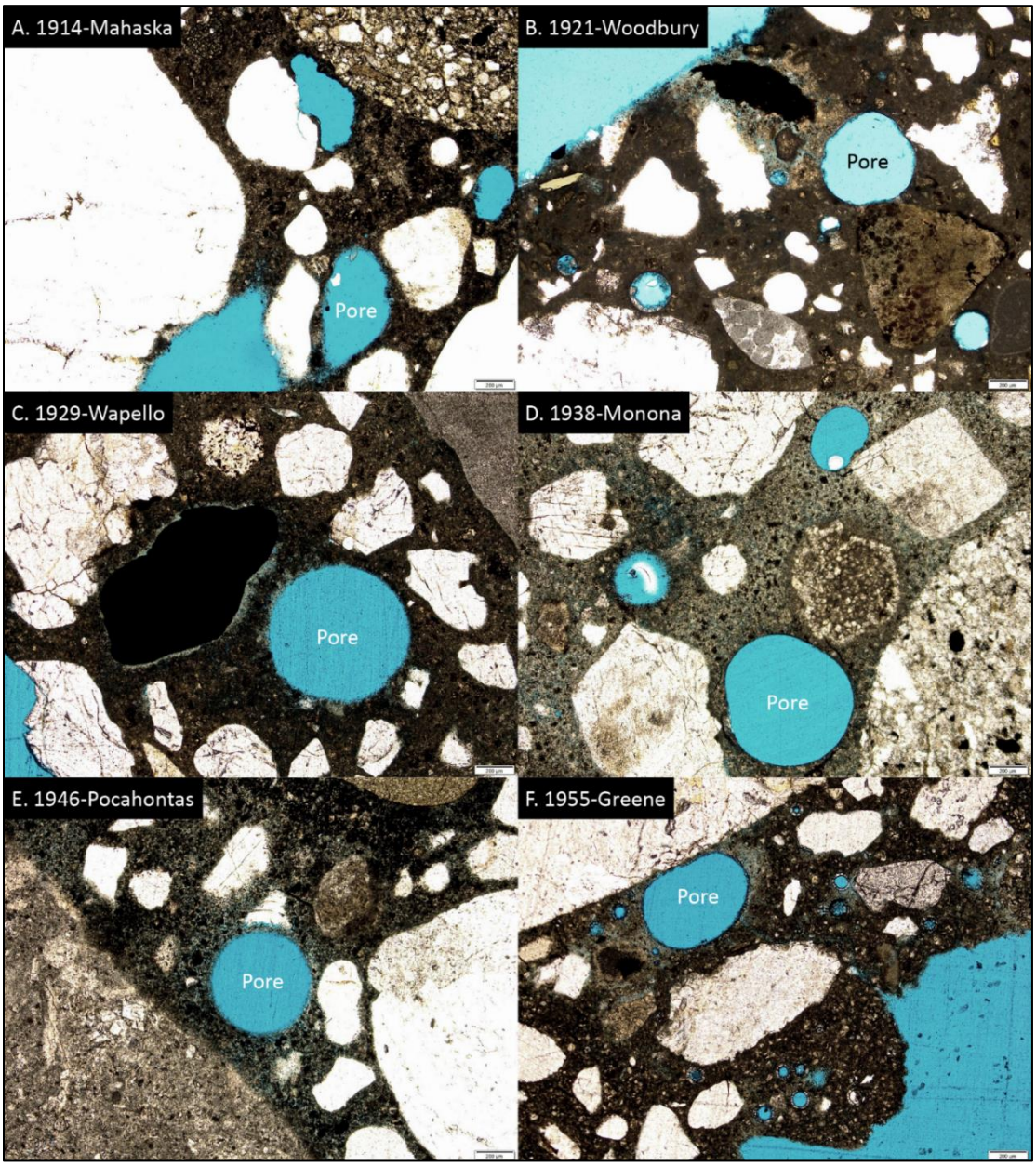

*Photomicrographs of open pores (blue) from samples **before** 1960. Scale bar is 200 µm in all images.*

Figure 56. Photomicrographs of open pores from samples *before* 1960

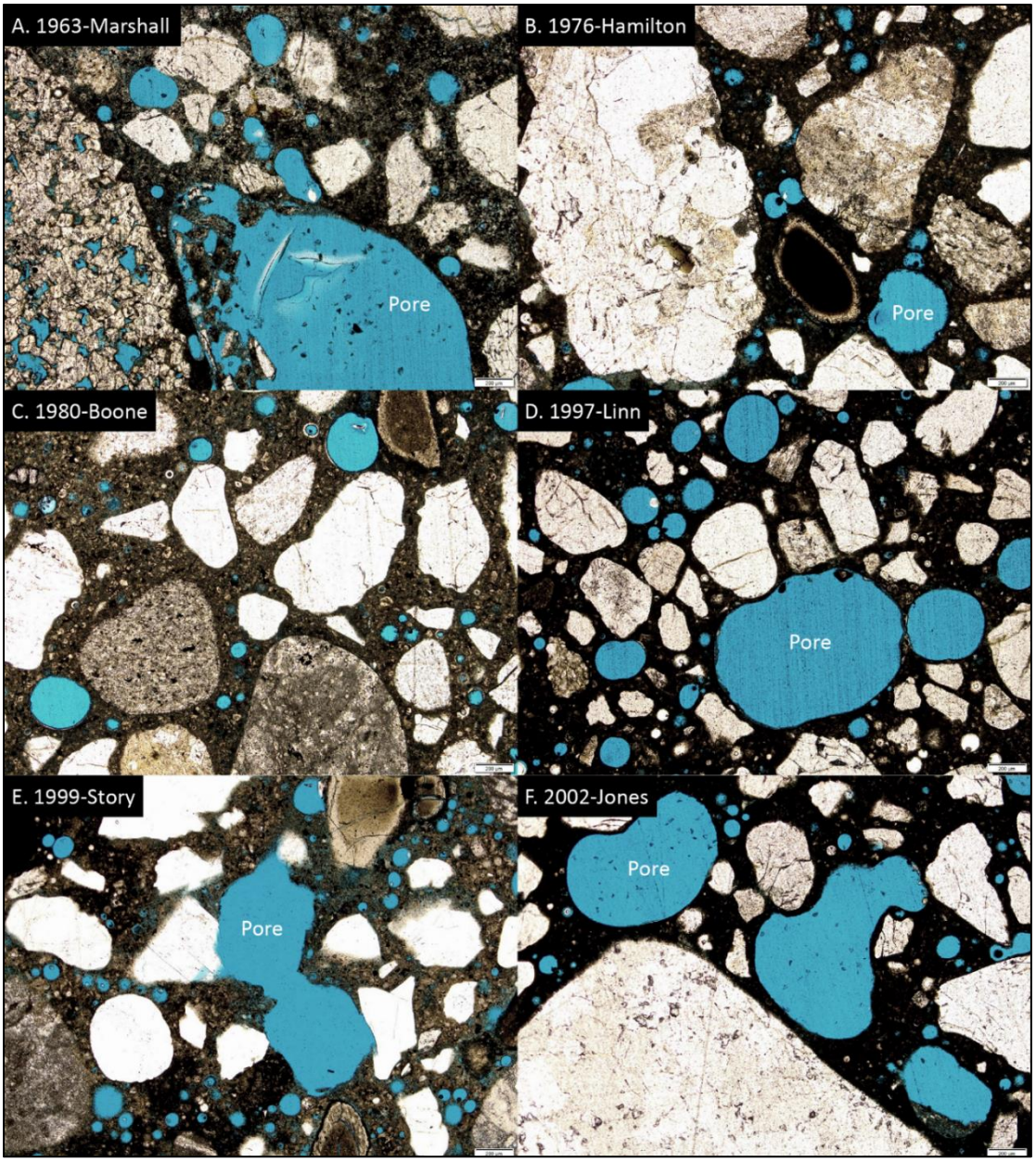

*Photomicrographs of open pores (blue) from samples **after** 1960. Scale bar is 200 µm in all images.*

Figure 57. Photomicrographs of open pores from samples *after* 1960

Pores with Diffuse Boundaries

Diffuse boundaries were observed in all thin sections except 1929-Wapello, 1938-Monona, and 1963-Marshall (Figures 58 and 59). These diffuse boundaries manifest as a fringe of what appears to be cement crystals lining open pores. In some cases, the fringe appears to completely occlude the pore, but this likely indicates that the plane of the thin section only cut tangentially through the pore.

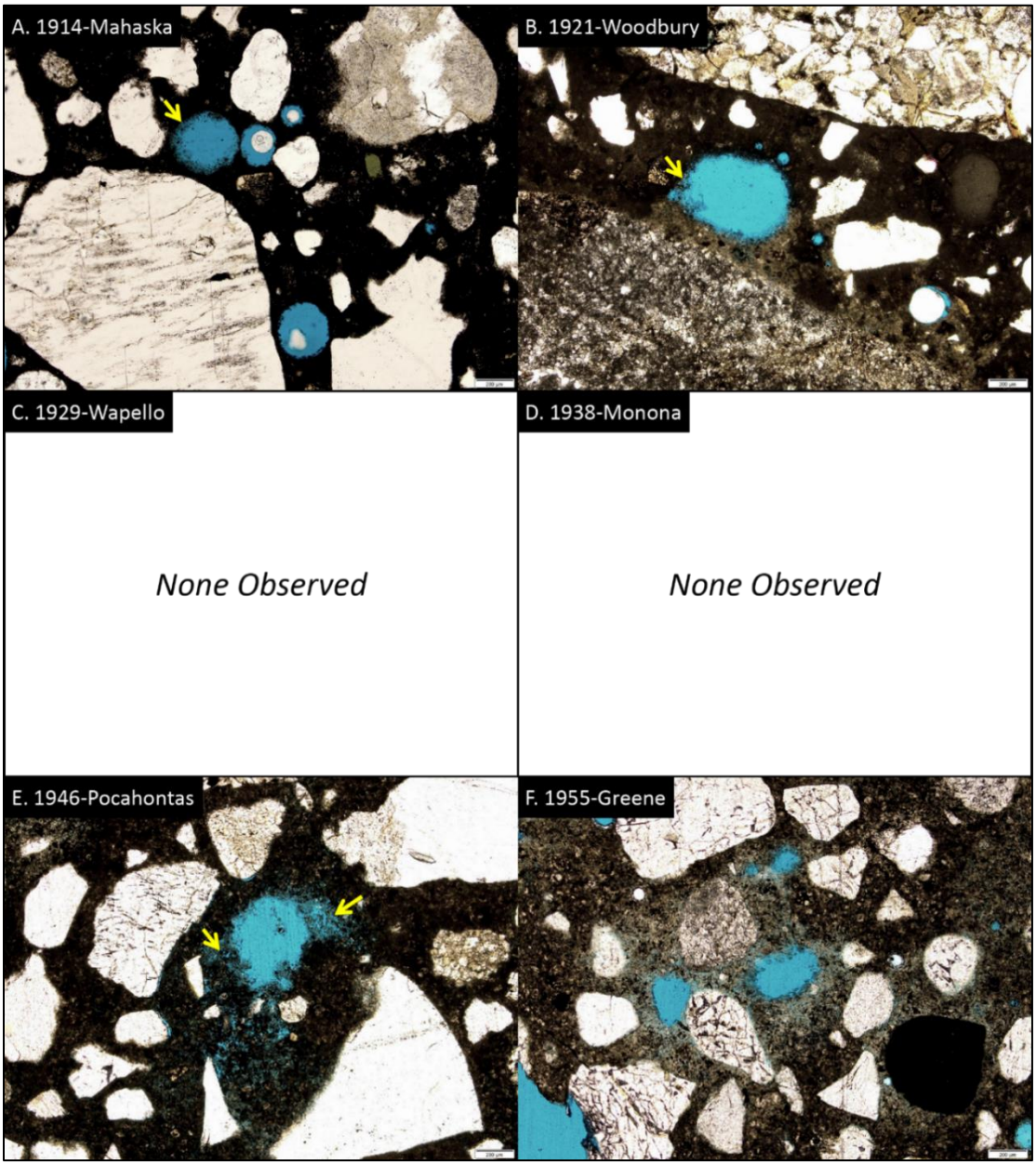

*Photomicrographs of pores with diffuse boundaries (yellow arrows) from samples **before** 1960. Scale bar is 200 µm in all images.*

Figure 58. Photomicrographs of pores with diffuse boundaries from samples *before* 1960

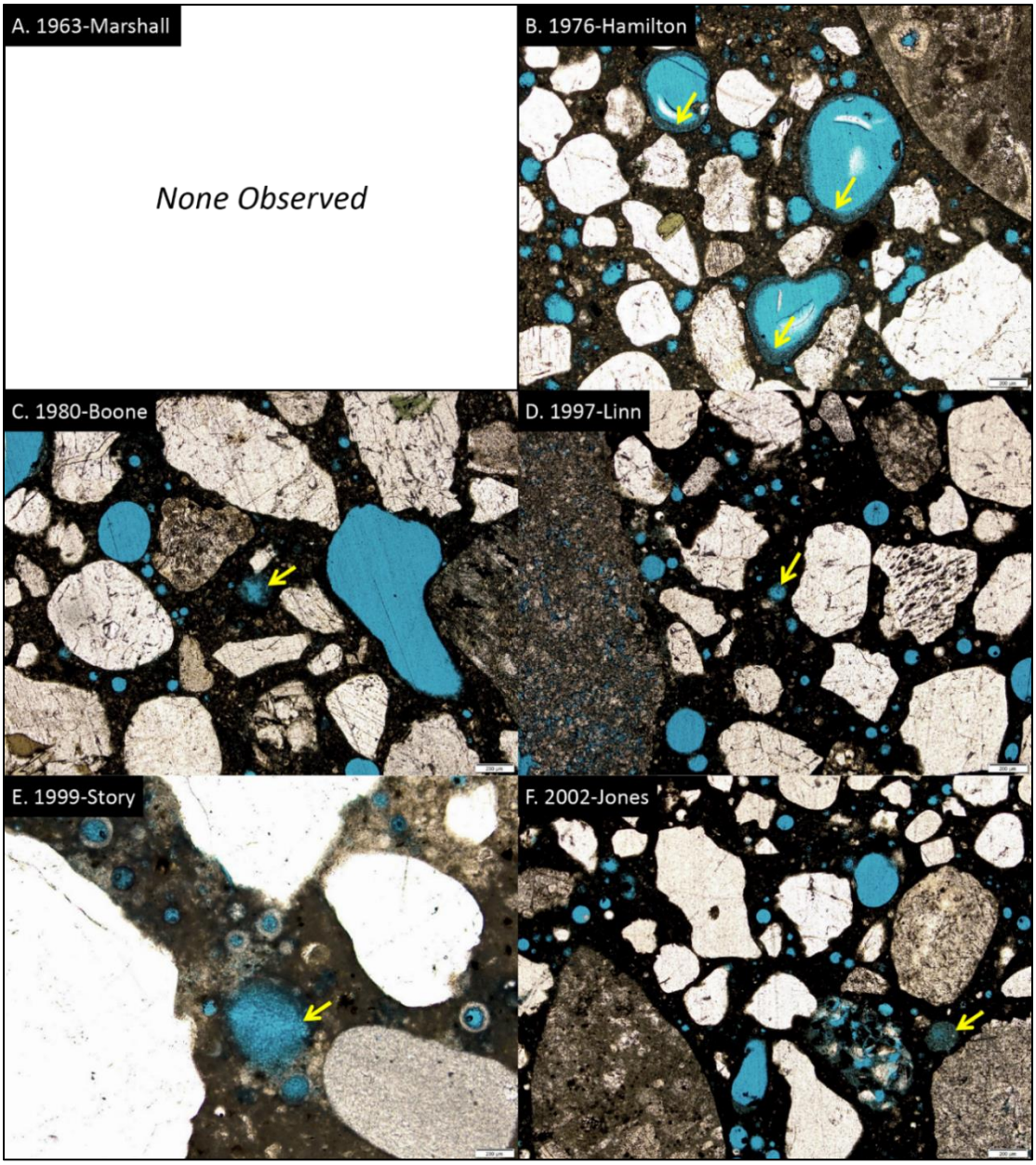

*Photomicrographs of pores with diffuse boundaries (yellow arrows) from samples **after** 1960. Scale bar is 200 µm in all images.*

Figure 59. Photomicrographs of pores with diffuse boundaries from samples *after* 1960

Pores with Mineral Cements

Mineral (i.e., non-paste) cements were found in all thin sections except 1938-Monona, 1946-Pocahontas, 1963-Marshall, and 2002-Jones (Figures 60 and 61). These cements range from irregular, discontinuous pore linings (Figures 60A, C) to irregular continuous pore linings (Figure 60B) to complete, isopachous pore linings (Figures 60F and 61D–E) to single crystals growing from pore walls (Figures 61B–C).

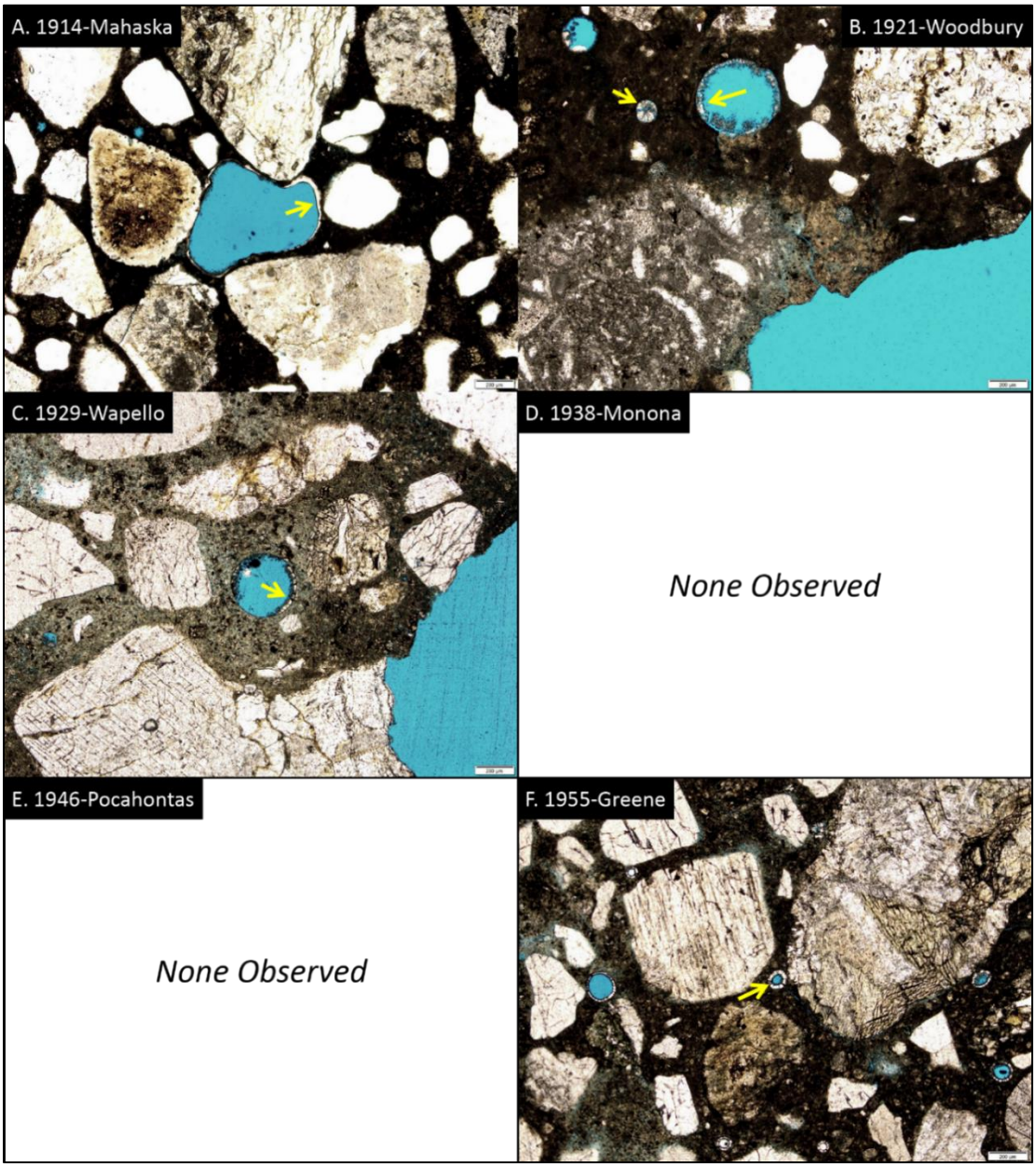

*Photomicrographs of pores with mineral cements (yellow arrows) from samples **before** 1960. Scale bar is 200 µm in all images.*

Figure 60. Photomicrographs of pores with mineral cements from samples *before* 1960

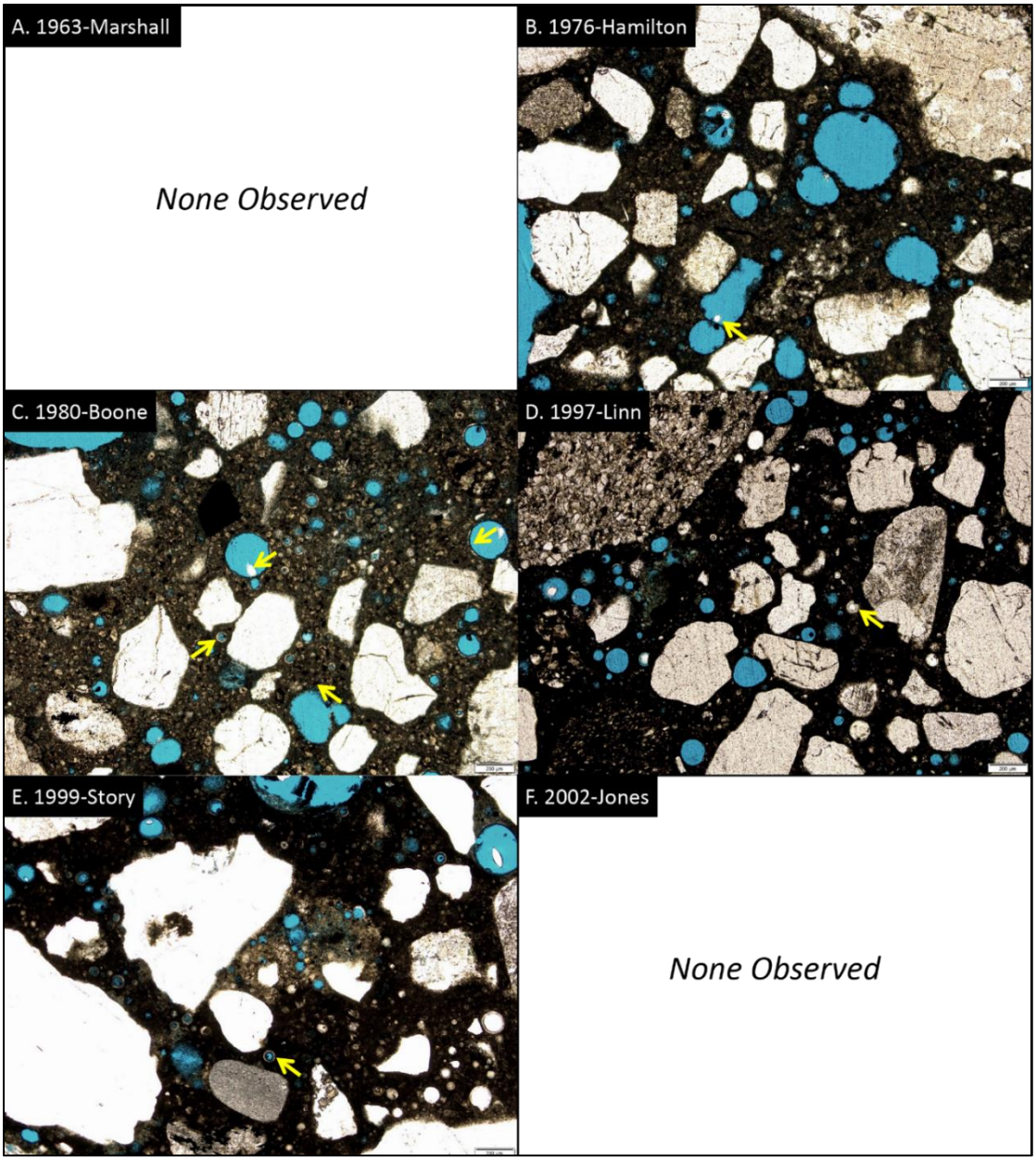

*Photomicrographs of pores with mineral cements (yellow arrows) from samples **after** 1960. Scale bar is 200 µm in all images.*

Figure 61. Photomicrographs of pores with mineral cements from samples *after* 1960

Coarse Aggregate Deterioration

CA deterioration was more commonly observed in pre-1960 samples than in post-1960 samples (Figures 62 and 63). Both mechanical (i.e., fracturing: Figures 62A, 62F, 63C, 63E) and chemical (i.e., dissolution: Figures 62B–D and 63A) deterioration were observed.

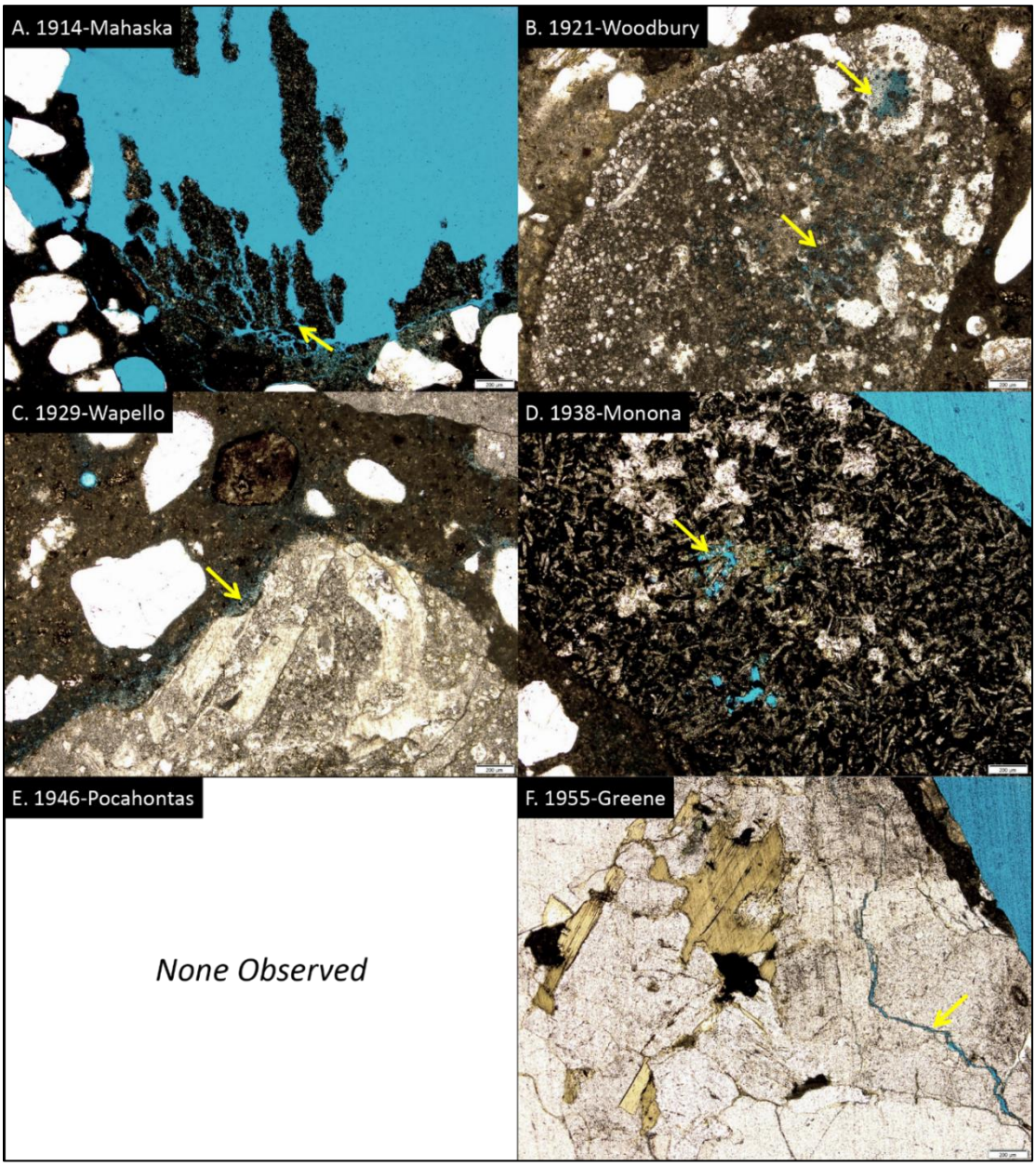

*Photomicrographs of coarse aggregate deterioration (yellow arrows) from samples **before** 1960. Scale bar is 200 µm in all images.*

Figure 62. Photomicrographs of coarse aggregate deterioration from samples *before* 1960

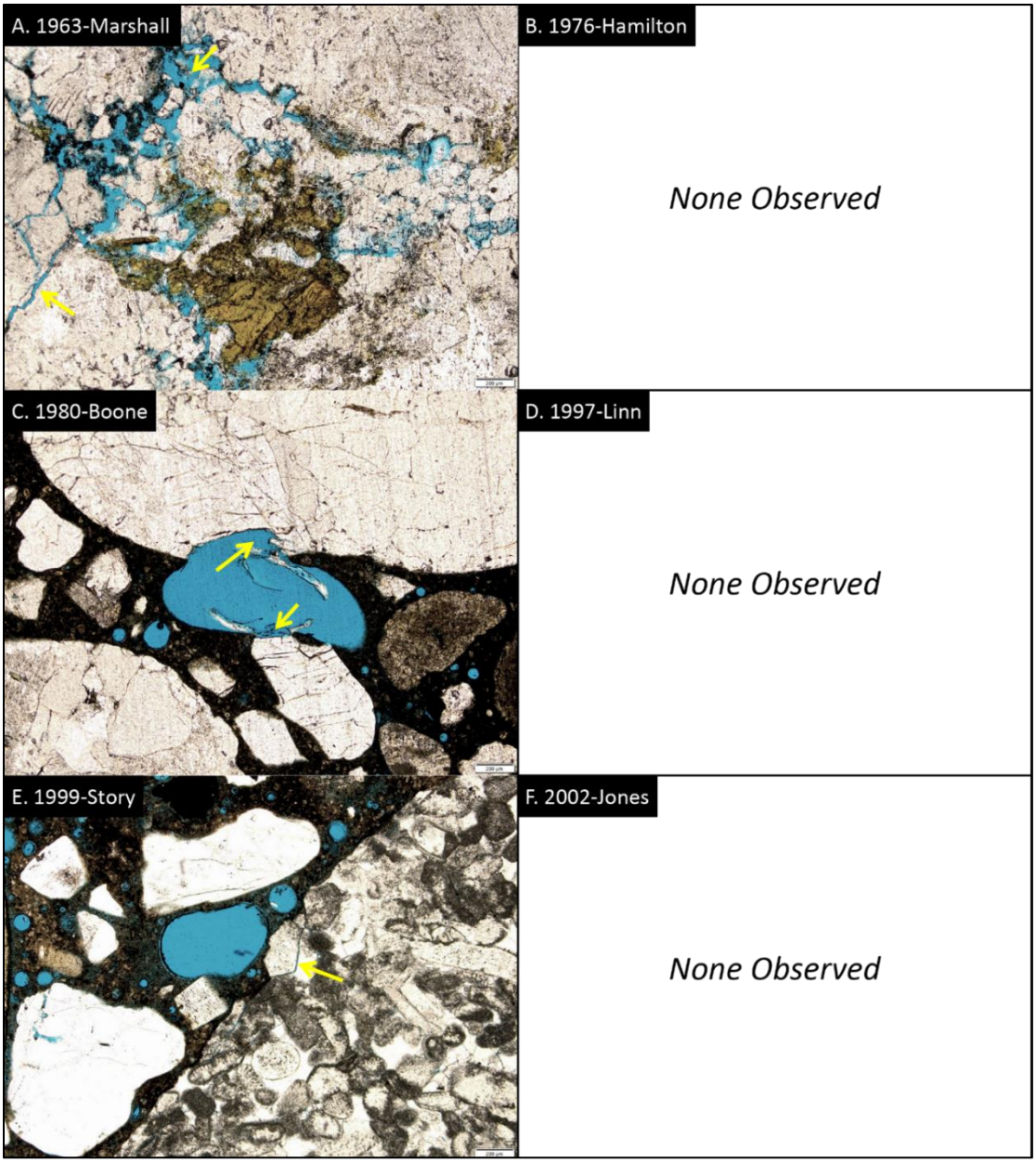

*Photomicrographs of coarse aggregate deterioration (yellow arrows) from samples **after** 1960. Scale bar is 200 µm in all images.*

Figure 63. Photomicrographs of coarse aggregate deterioration from samples *after* 1960

Fine Aggregate Deterioration

Deterioration in fine aggregate (Figures 64 and 65) was most commonly observed in shale particles that had undergone shrinkage fracturing (e.g., Figures 64E–F, 65C, and 65E). Dissolution of fine aggregate was also observed (Figures 64A–B, D, 65B) as was non-shale fracturing (Figure 65A).

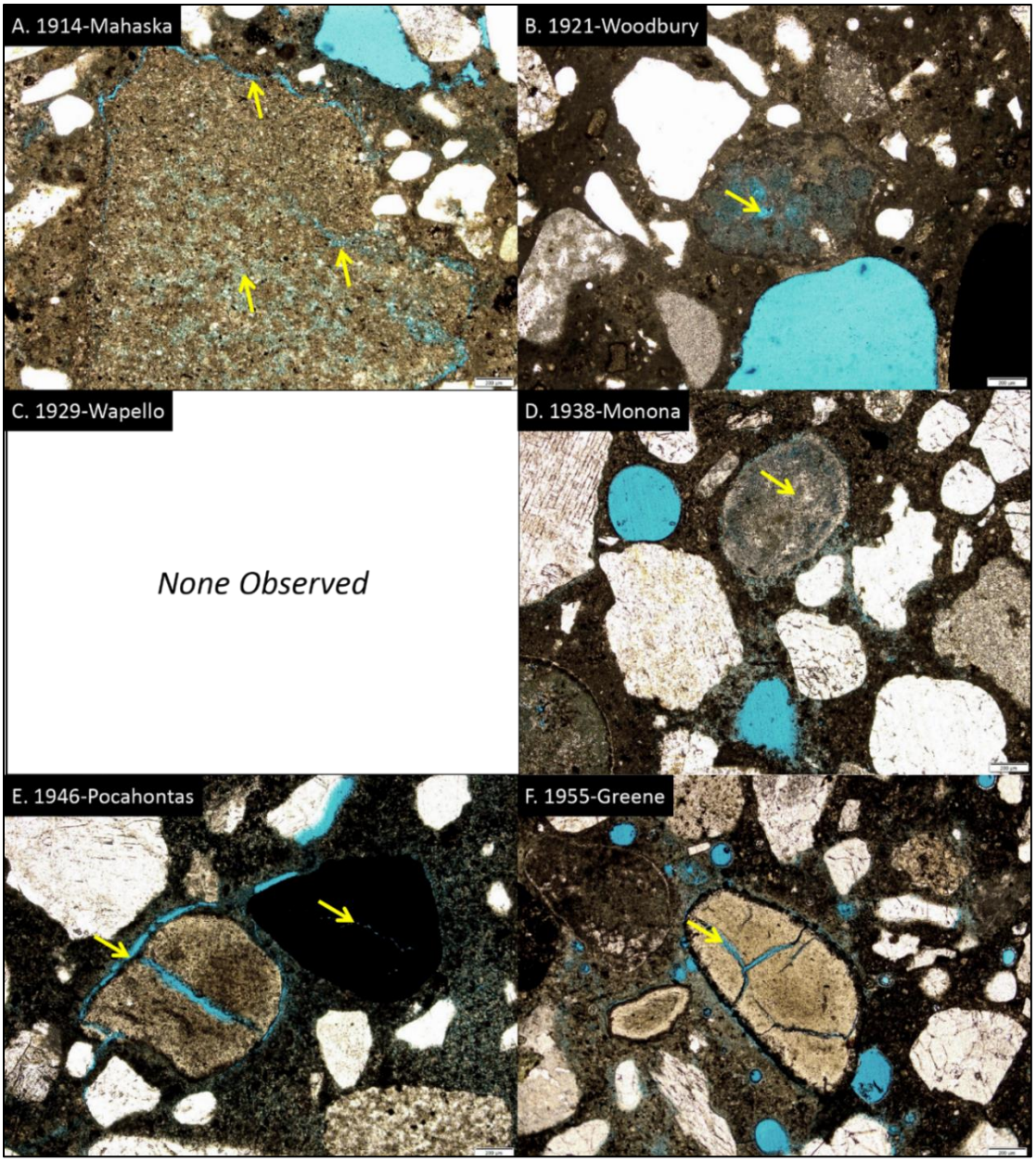

*Photomicrographs of fine aggregate deterioration (yellow arrows) from samples **before** 1960. Scale bar is 200 µm in all images.*

Figure 64. Photomicrographs of fine aggregate deterioration from samples *before* 1960

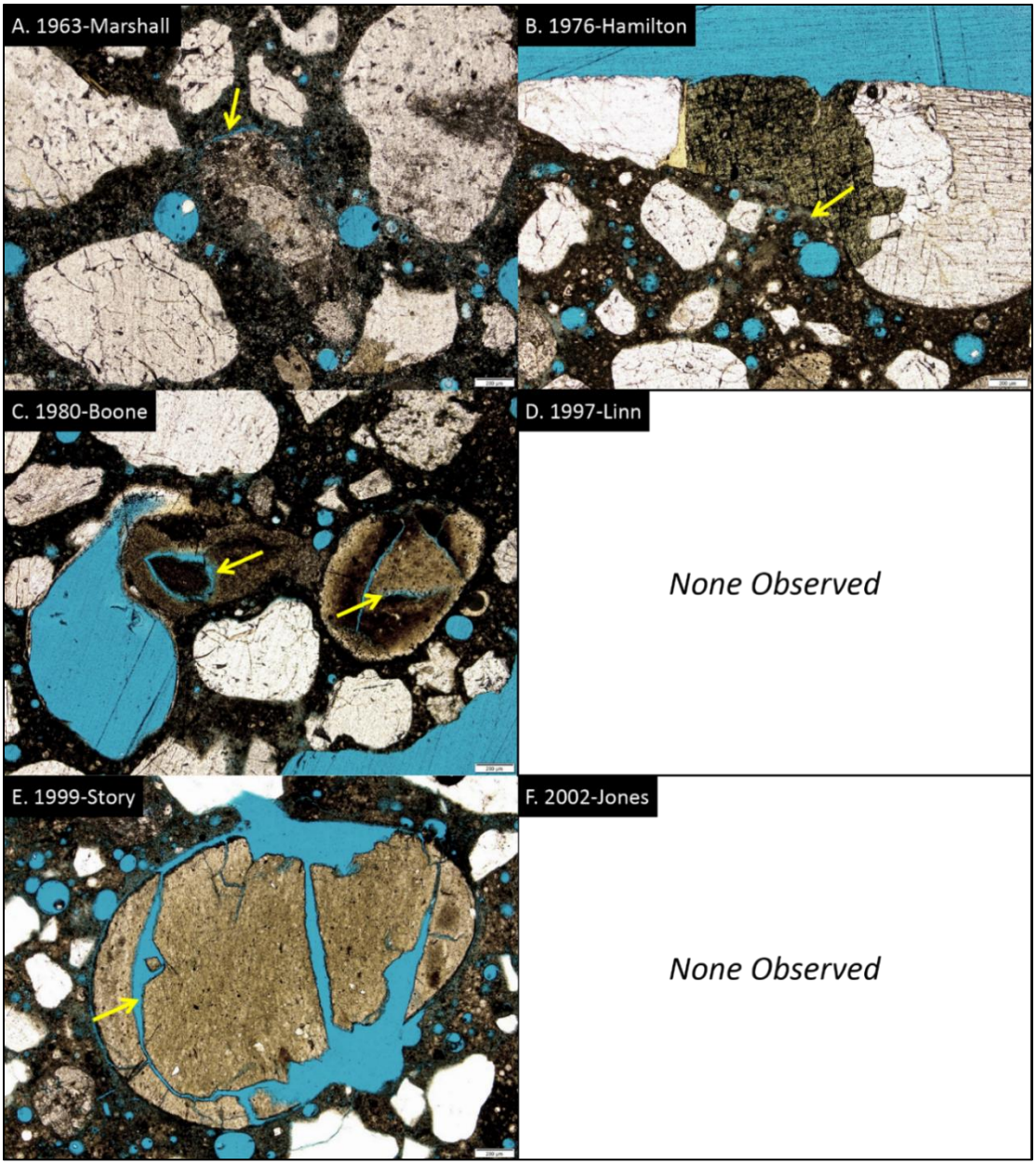

*Photomicrographs of fine aggregate deterioration (yellow arrows) from samples **after** 1960. Scale bar is 200 µm in all images.*

Figure 65. Photomicrographs of fine aggregate deterioration from samples *after* 1960

Pores with Fine Aggregate and Paste Debris

It was common to find pores containing fine aggregate and cement paste "debris" (Figures 66 and 67). This fine aggregate consists of exceedingly small particles (<200µm in diameter) that forms a mesh with the cement paste (e.g., Figures 66F, 67F). This mesh itself contains pores. When it does not occur as a mesh, the debris appears to have come into equilibrium with gravity (a "geopetal" structure such that it fills only one part of the pore) (Figures 66C, E).

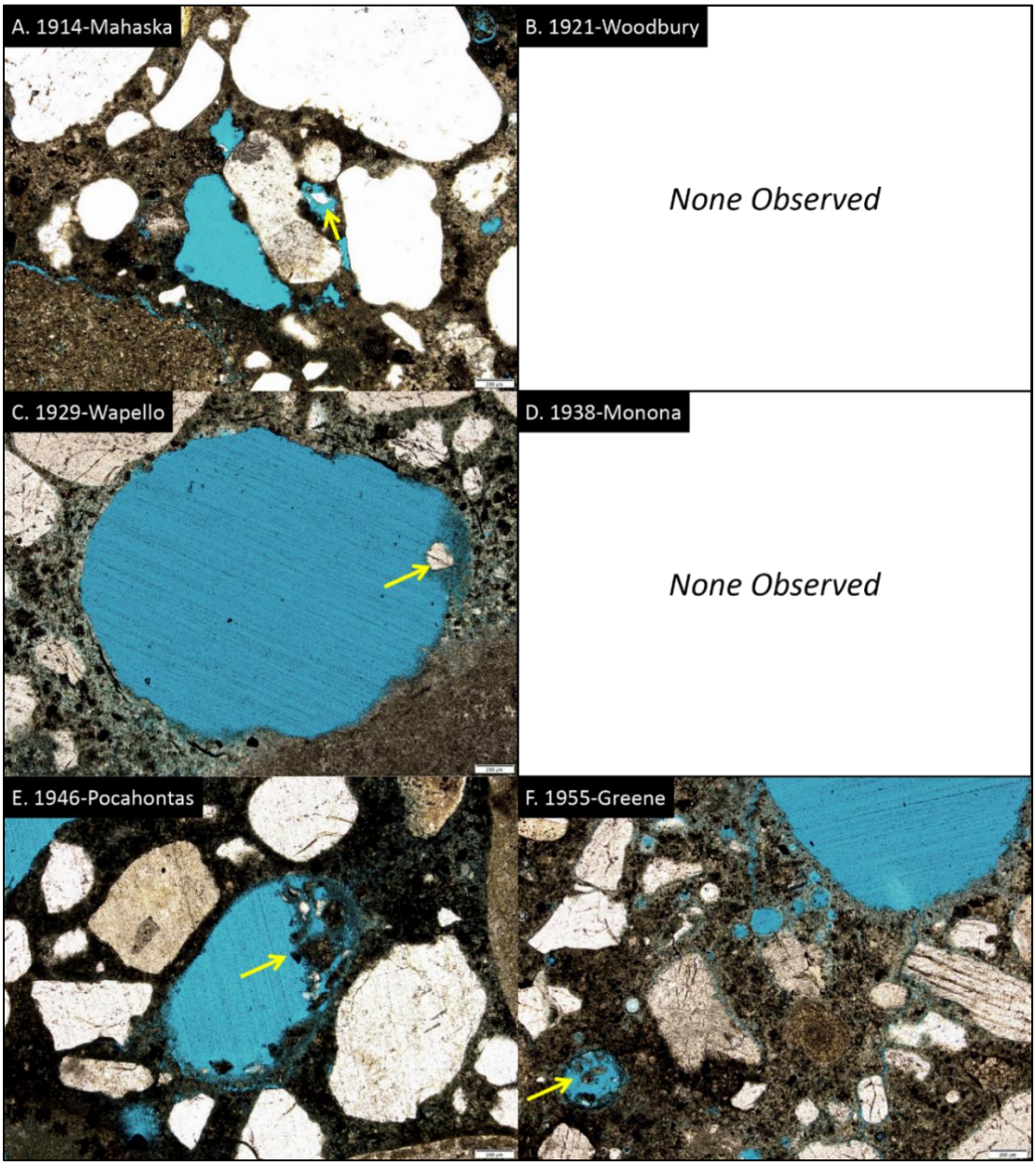

*Photomicrographs of pores with fine aggregate and paste debris (yellow arrows) from samples **before** 1960. Scale bar is 200 µm in all images.*

Figure 66. Photomicrographs of pores with fine aggregate and paste debris from samples *before* 1960

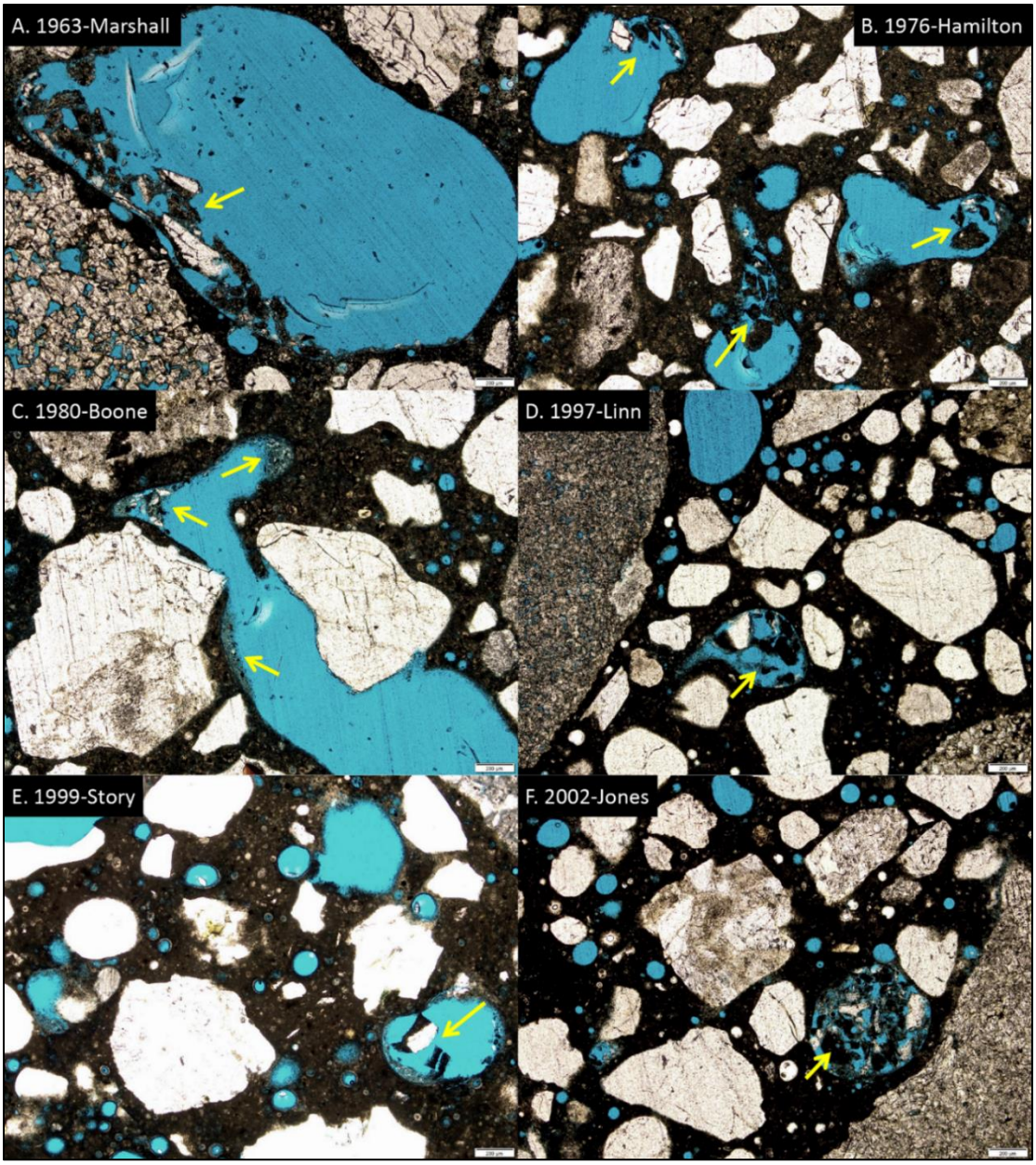

*Photomicrographs of pores with fine aggregate and paste debris (yellow arrows) from samples **after** 1960. Scale bar is 200 µm in all images.*

Figure 67. Photomicrographs of pores with fine aggregate and paste debris from samples *after* 1960

Deteriorated Paste

Cement paste across the various samples does not show a uniform character (Figures 68 and 69). The pre-1960 samples all show some variety of paste deterioration (Figure 68), which is characterized by a mottled appearance that is more microporous than the majority of the thin section. This paste deterioration is often found around specific larger pores or certain fine aggregate particles. Among the post-1960 samples, only 1999-Story shows evidence of paste deterioration and in that case it is highly localized (Figure 69E).

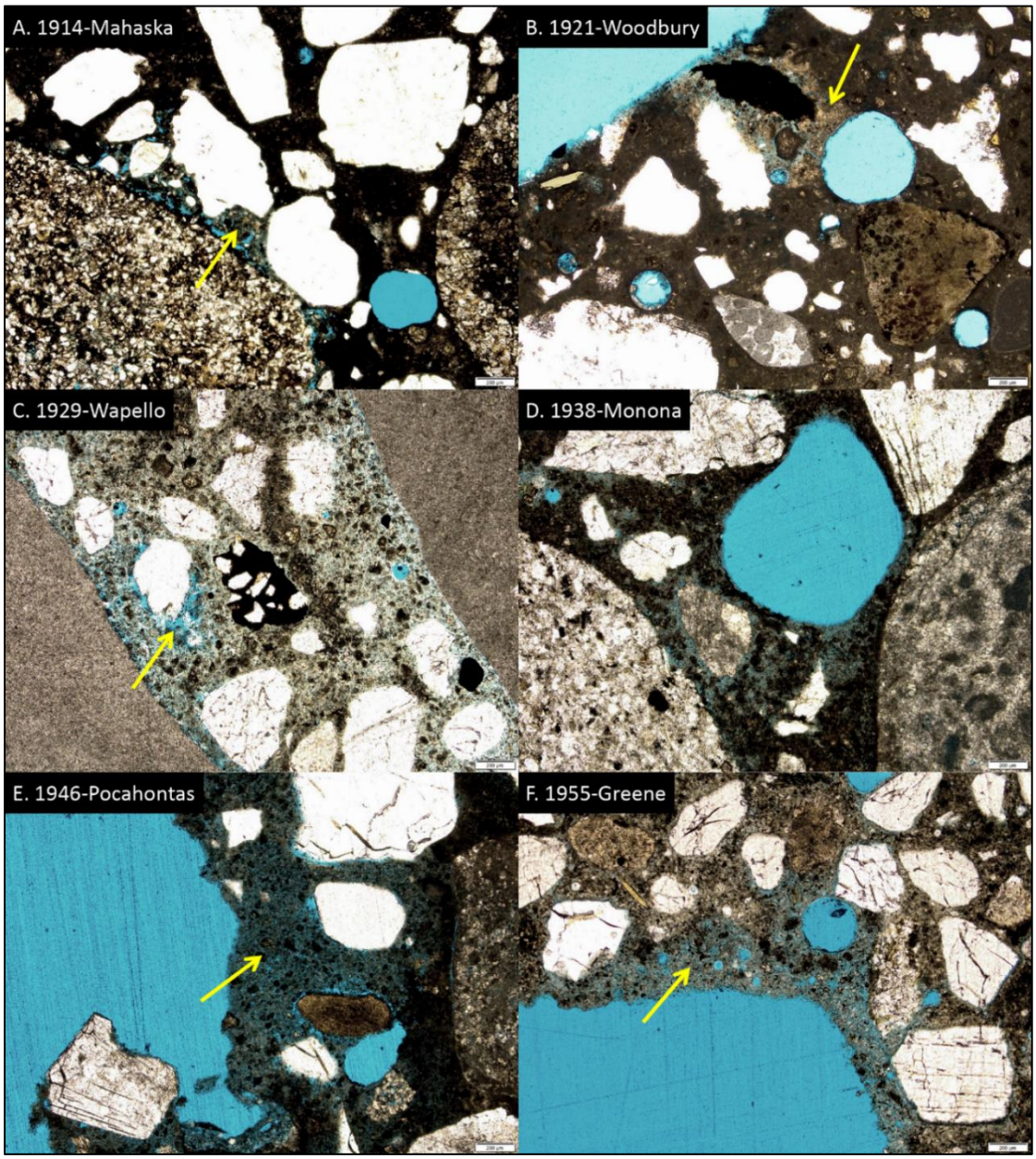

*Photomicrographs of deteriorated paste (yellow arrows) from samples **before** 1960. Scale bar is 200 µm in all images.*

Figure 68. Photomicrographs of deteriorated paste from samples *before* 1960

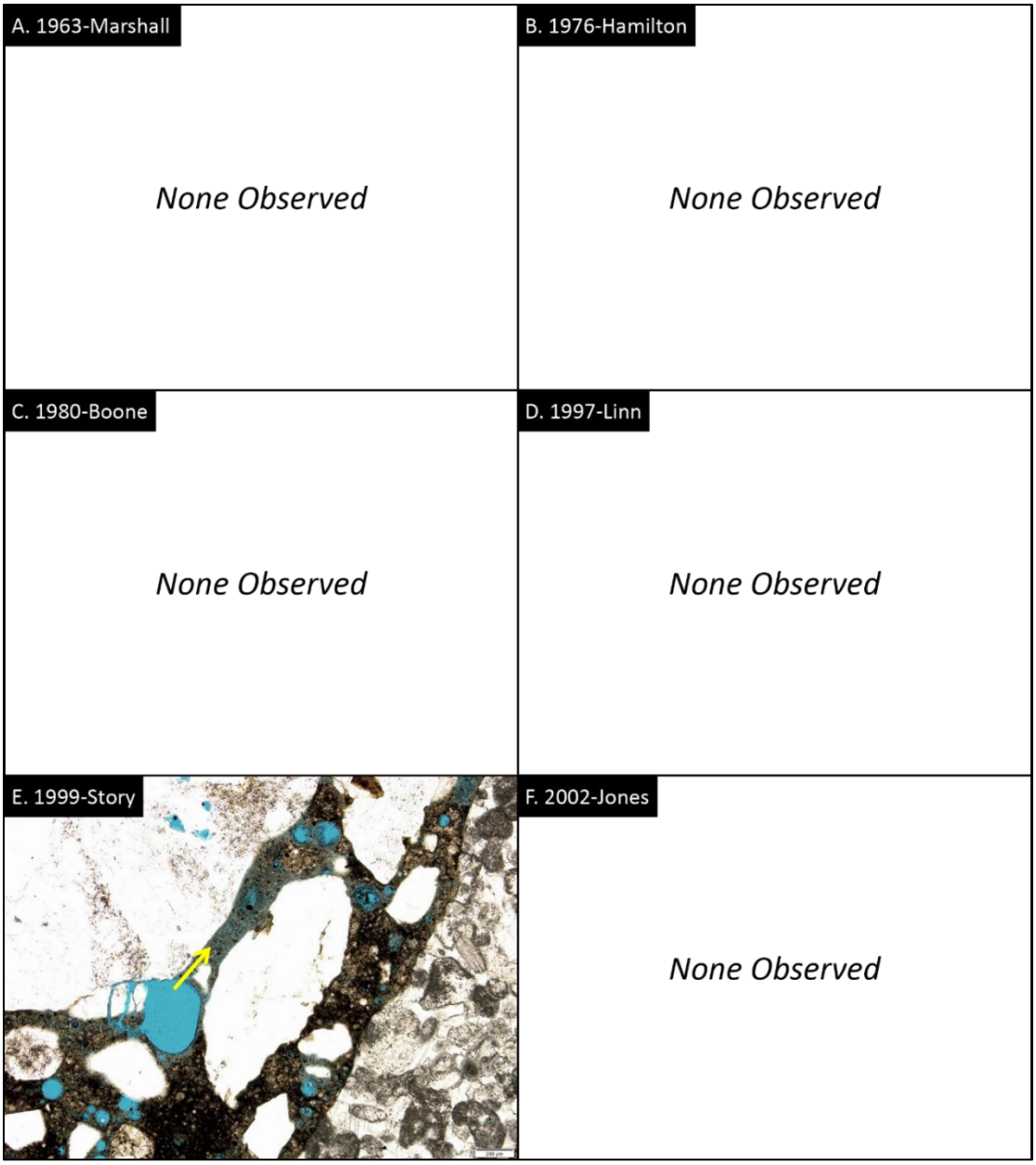

*Photomicrographs of deteriorated paste (yellow arrows) from samples **after** 1960. Scale bar is 200 µm in all images.*

Figure 69. Photomicrographs of deteriorated paste from samples *after* 1960

Fractures

Hairline fractures were found in all samples except 1938-Monona, 1955-Greene, and 1980-Boone (Figures 70 and 71). These fractures were less than 15 µm in aperture and, in the pre-1980 samples, predominantly cut across paste (e.g., Figures 70A–F and 71A–B). The post-1980 fractures were observed to continue both around and through pores within the paste (e.g., Figures 71D–F).

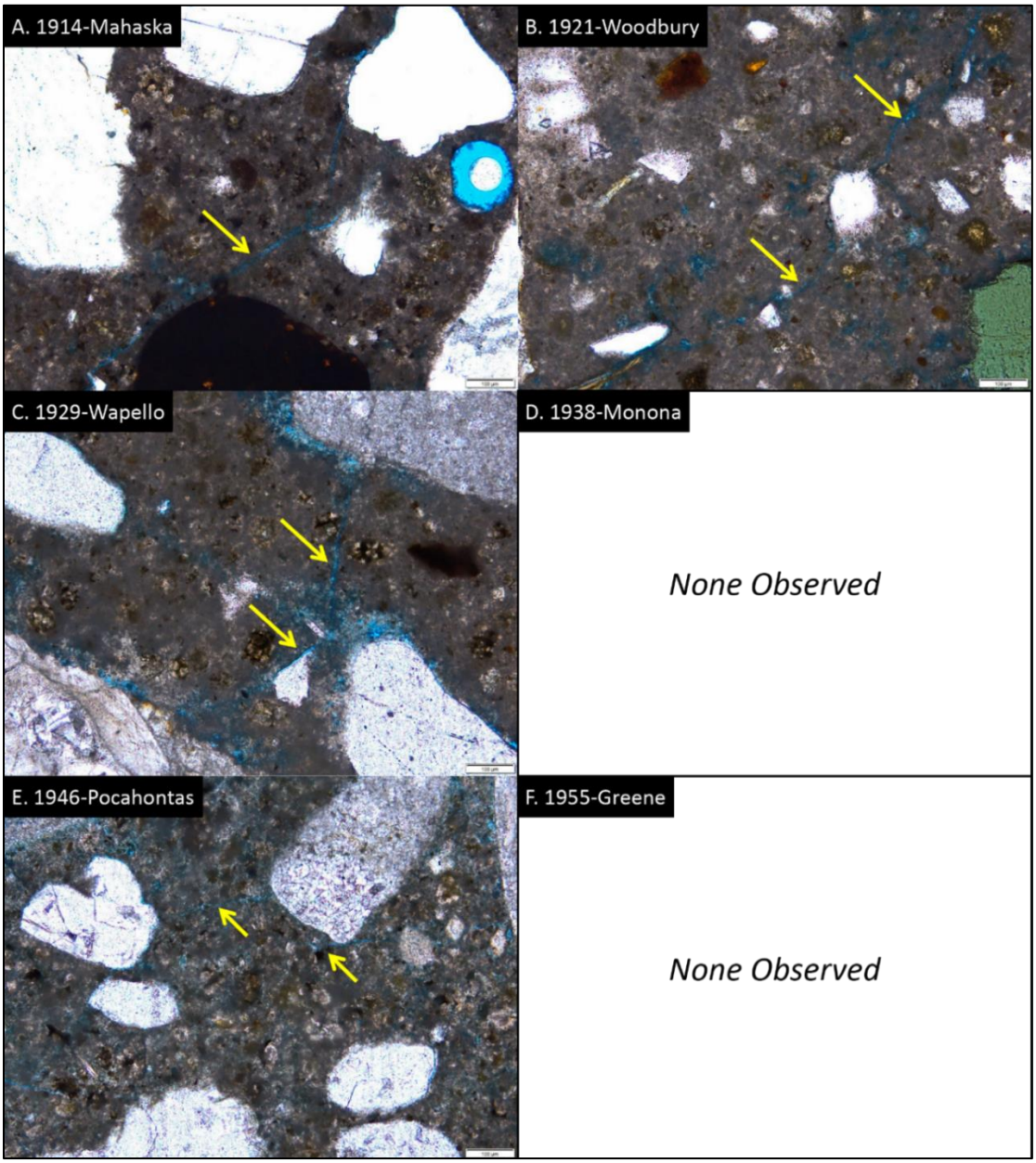

*Photomicrographs of fractures (yellow arrows) in paste from samples **before** 1960. Scale bar is 100 µm in all images.*

Figure 70. Photomicrographs of fractures in paste from samples *before* 1960

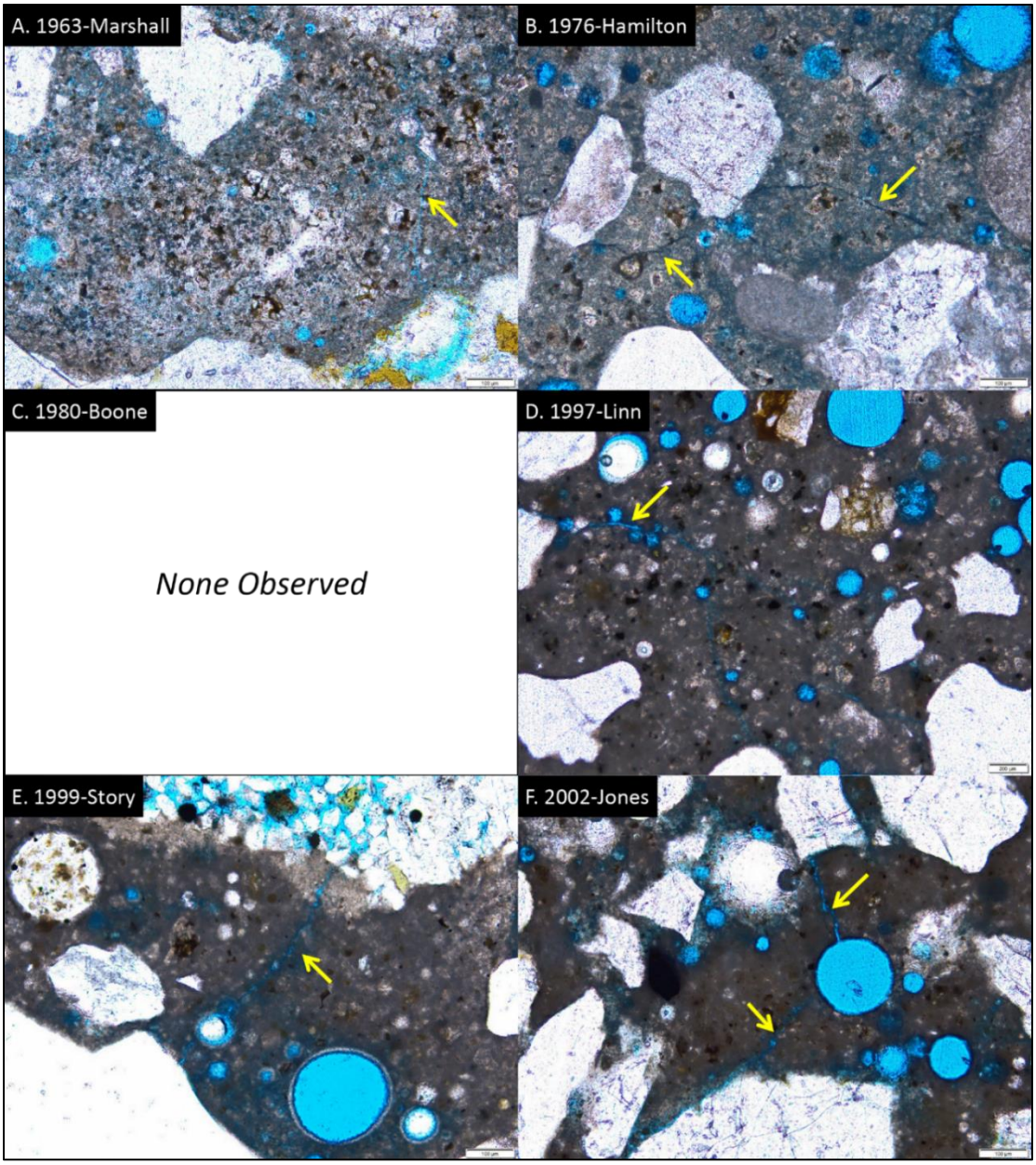

*Photomicrographs of fractures (yellow arrows) in paste from samples **after** 1960. Scale bar is 100 µm in all images.*

Figure 71. Photomicrographs of fractures in paste from samples *after* 1960

Paste Pores

The cement paste itself was observed to exhibit a wide variety of porosities from highly porous to nonporous, so representative photomicrographs from each sample documenting its least and most porous areas were recorded (Figures 72–75). Where their paste is most highly porous, most samples show dark, but slightly blue-tinted, areas (e.g., Figures 72 Aii, 75Cii). The samples from 1929–1955, however, show areas of paste that are significantly more porous, such that they show the full intensity of the blue epoxy (Figures 72Cii and 73Aii, Bii, and Cii).

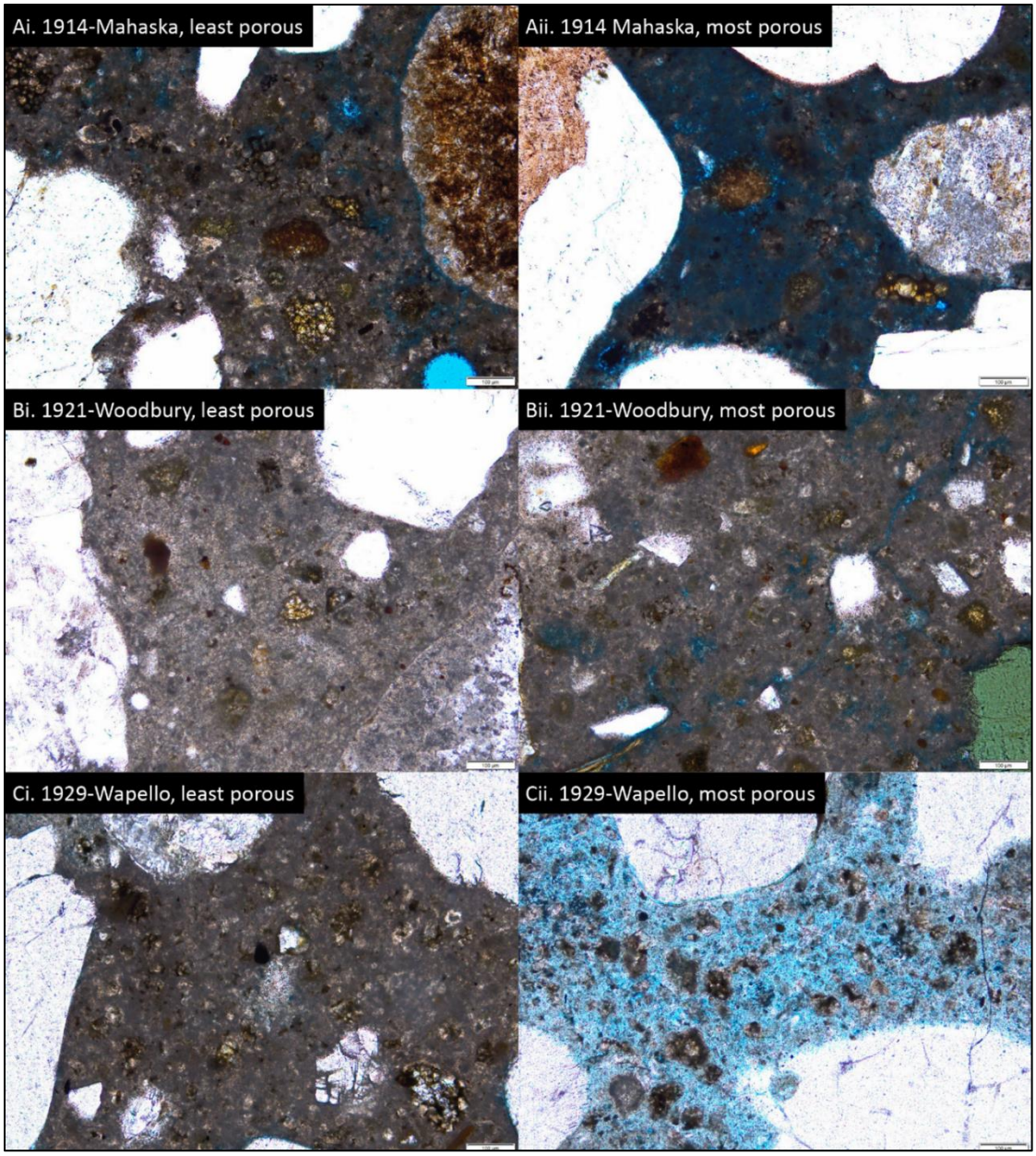

Photomicrographs showing examples of least (i) and most (ii) porous paste from samples 1914-Mahaska (A), 1921-Woodbury (B), and 1929-Wapello (C). Scale bar is 100 µm in all images.

Figure 72. Photomicrographs showing examples of least (i) and most (ii) porous paste from samples 1914-Mahaska (A), 1921-Woodbury (B), and 1929-Wapello (C)

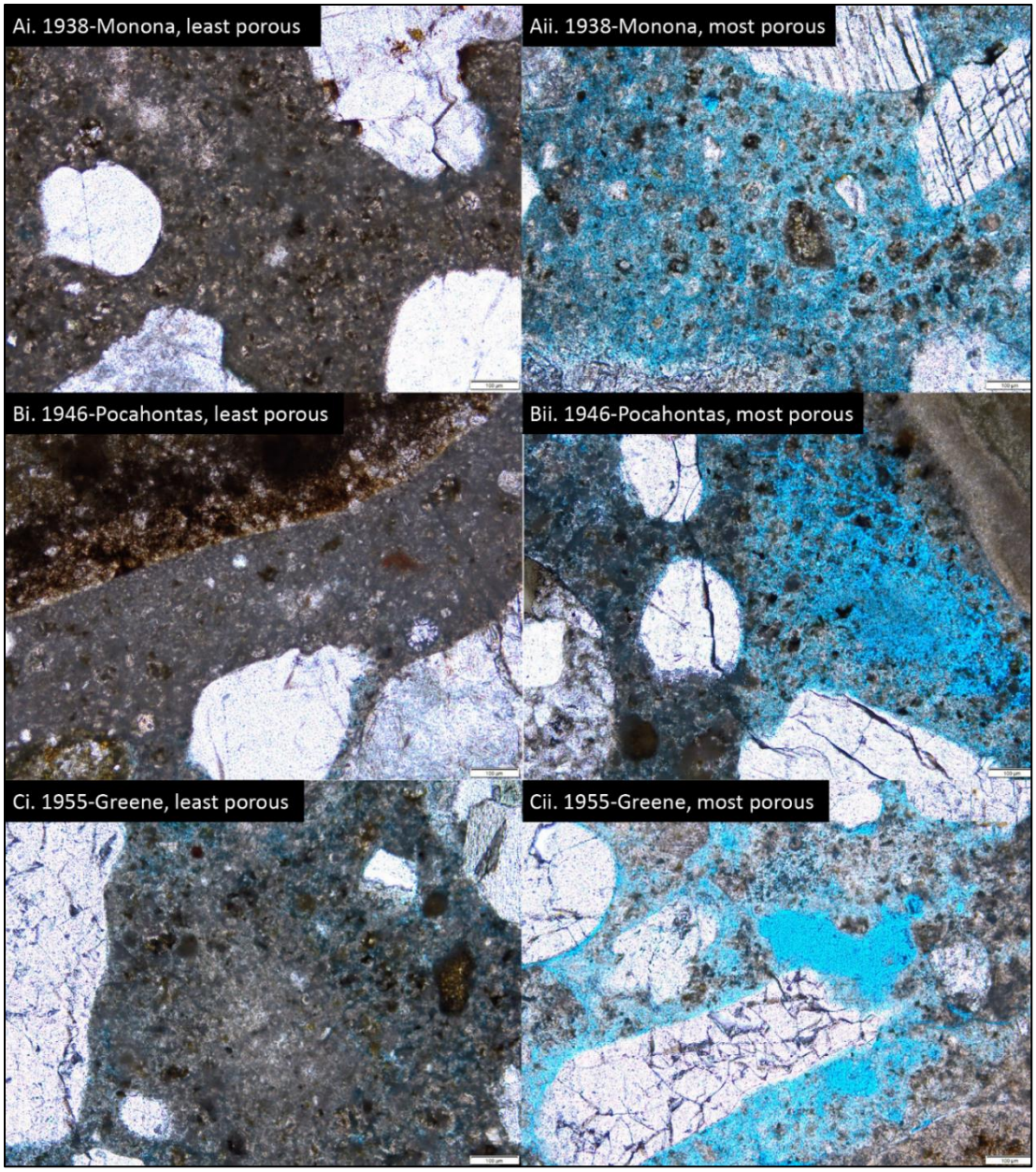

Photomicrographs showing examples of least (i) and most (ii) porous paste from samples 1938-Monona (A), 1946-Pocahontas (B), and 1955-Greene (C). Scale bar is 100 µm in all images.

Figure 73. Photomicrographs showing examples of least (i) and most (ii) porous paste from samples 1938-Monona (A), 1946-Pocahontas (B), and 1955-Greene (C)

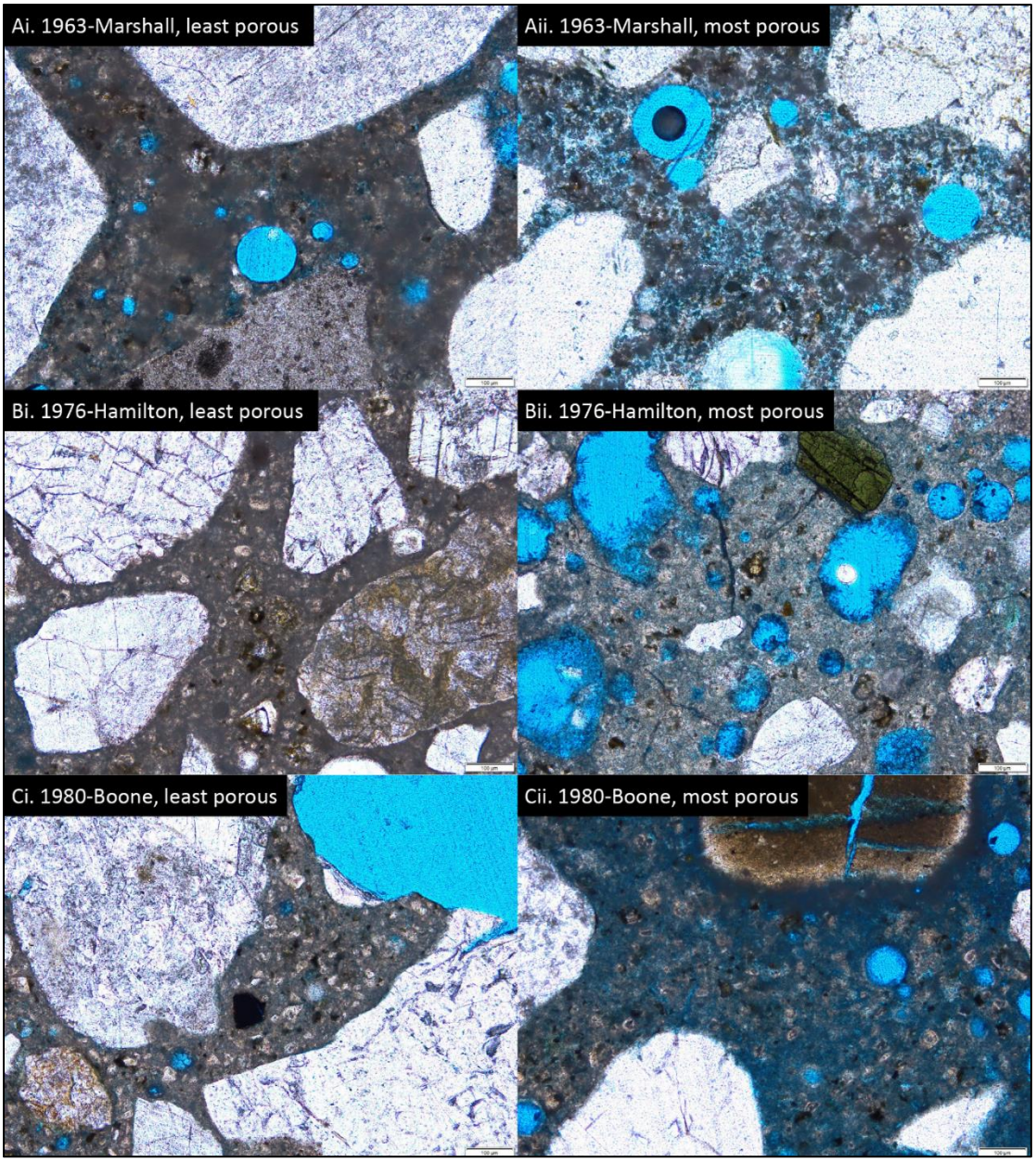

Photomicrographs showing examples of least (i) and most (ii) porous paste from samples 1963-Marshall (A), 1976-Hamilton (B), and 1980-Boone (C). Scale bar is 100 µm in all images.

Figure 74. Photomicrographs showing examples of least (i) and most (ii) porous paste from samples 1963-Marshall (A), 1976-Hamilton (B), and 1980-Boone (C)

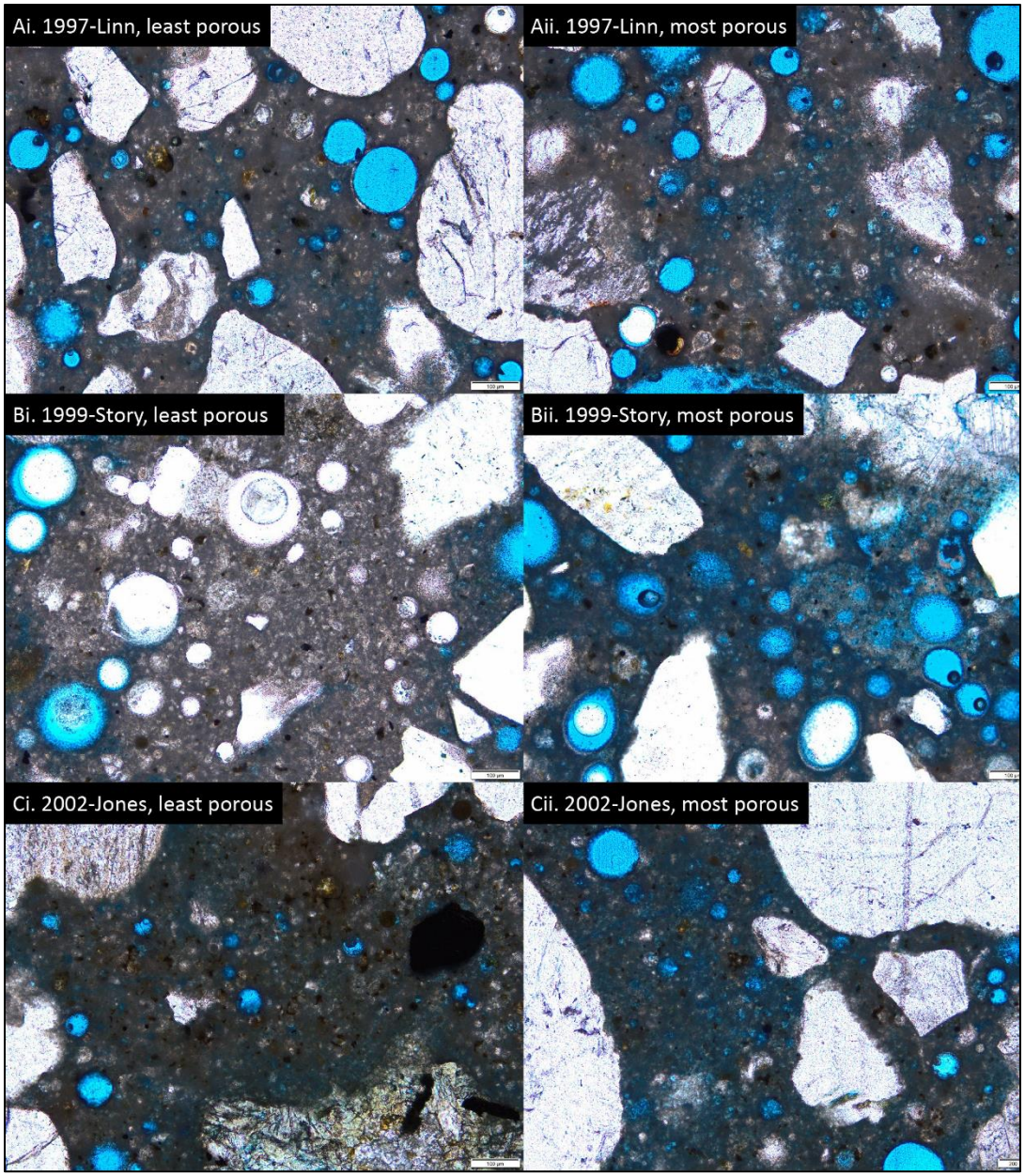

Photomicrographs showing examples of least (i) and most (ii) porous paste from samples 1997-Linn (A), 1999-Story (B), and 2002-Jones (C). Scale bar is 100 µm in all images.

Figure 75. Photomicrographs showing examples of least (i) and most (ii) porous paste from samples 1997-Linn (A), 1999-Story (B), and 2002-Jones (C)

DISCUSSION

Porosity vs. Age Correlation

One of the most striking correlations observed in this study is that between porosity (whether measured via helium, ASTM C457, or CT) and the age of the pavement (previous Figure 3): the older the pavement, the less porous it is.

This correlation is conspicuous for two reasons. First, it was thought that a step-change in PCC porosity would be observed when air entrainment was required in Iowa in 1952. Instead, we observed a predictable decrease in the helium porosity of PCC from 15–20% in the youngest three samples to 5–8% in the oldest samples. In addition, it was observed that open pores similar in size and shape to modern "air entrainment" pores were visible even in PCC manufactured pre-1950 (in addition to the larger pores observed to derive from the deterioration of CA). This suggests that either air-entraining agents were being used before they were widely acknowledged (a "secret sauce") or that the fine aggregate has deteriorated to the extent that the resulting pores mimic the function of pores introduced via air-entraining agents.

Second, in the pilot study, deterioration of CA was observed in the older samples (i.e., 1914-Mahaska, 1921-Woodbury) but not the younger 1999-Story sample. However, the more comprehensive study found CA deterioration in samples across the age range, in addition to paste deterioration and fracturing. This suggests that both mechanical and chemical deterioration processes have occurred across the life spans of these pavements.

The correlation between porosity and age suggests that some process is occluding pore space in PCC. Mineralization in large open pores was observed in numerous thin sections (e.g., previous Figures 60 and 61), but none of these was completely pore-occluding and there was no trend toward an increased abundance of mineral cements with PCC age.

One PCC property does seem to have a strong correlation with age and that is the character of the paste (e.g., Figures 54 and 55). In the oldest samples, paste crystals appear lighter in color due to no micron-sized pore space existing between the paste crystallites. In progressively younger samples, it was seen that the paste character darkens and is more blue-tinted due to there being more micron-sized pore space in the paste. This general trend was complicated by the observation that in many "middle-aged samples" (i.e., 1929-Wapello to 1955-Greene), there exist discrete patches of extreme paste deterioration.

Permeability vs. Age Correlation

The next most interesting observation was that permeability correlated with age but in a different way than porosity. That is, permeability was low both in young and old samples, but high in intermediate-age samples (previous Figure 4). Porosity and permeability are often correlated in porous media through the Kozeny-Carmen relation:

$$K = \left[\frac{\phi^3}{c(1-\phi^2)S^2}\right] \quad \textbf{(6)}$$

where:
K = permeability (millidarcies)
ϕ = porosity (void volume per unit bulk volume)
c = Kozeny constant (different for each material)
S = specific surface area (pore network surface area per unit bulk volume)

Therefore, we should expect the older PCC with lower porosities to have lower permeabilities and indeed this trend is observed for 1980-Boone and older samples. Younger samples, however, show decreasing chloride permeability.

The CT images of samples after 1980-Boone (previous Figures 14 and 22–24) lack the large deterioration pores that may be acting as high-permeability pathways to enable chloride ions to penetrate the older samples. Compositionally, these post-1980 samples were also made with fly ash (previous Table 2), a source of silica that may be acting as a dispersed insulator, impeding the flow of the electrical current that is used in the measurement of chloride ion permeability.

Aggregate Deterioration

The final step in the integrated analysis of Iowa PCC involved visual characterization of pore types, porosity, connectivity, and lithology using thin sections (previous Table 2). Numerous CT images (previous Figures 12–21) and thin sections show evidence of CA deterioration (e.g., previous Figures 32–34, 38, 44–45, and 62–63). The dominant pore type of the pre-1950 samples was moldic because the shape of these pores resembles the shape of CA grains.

In addition, larger dissolution rims are visible in the post-1950 samples. Deterioration within CA was found in 5 of the 6 pre-1960 pavements, but only in 3 of the 6 post-1960 pavements (e.g., previous Figures 62 and 63). Deterioration was observed as open fractures connecting to entrained air pores and as pore space around CA (previous Figures 70 and 71).

Intraparticle pores are more abundant in the post-1950 samples and they are connected to entrained air pores through microporosity (previous Figures 16H, J, and L). Similar to the pre-1950 samples, those PCC pavements that have limestone as a CA source show abundant interparticle porosity within grains (previous Figures 16G, H, and J). The younger samples have more heterogenous pore networks, where grains are undergoing deterioration and forming intraparticle pores and fractures. Entrained air may be connected to the total porosity of these samples through fractures and microporosity in the paste.

Mineral Growth

In addition to deterioration of CA, mineral growth in pores was evident in many samples. While mineral precipitation in pores in the post-1950 samples was less abundant (e.g., previous Figures 16K and L), these pores seem to be connected with entrained air voids through the paste.

The trend of decreasing porosity with age (previous Figure 3) can be explained by this complex air void network in the post-1950 samples and mineral growth in deterioration pores in the pre-1950 samples. While the pre-1950 and post-1950 samples have similar pore types, the deterioration mechanisms for the two groups are not similar. The pre-1950 samples have complete deterioration of the CA, resulting in the formation of large pores that allow water drain through the pavement. Overall, the post-1950 samples have an interconnected air void network through deteriorating aggregate and fractures in the paste, and mineral precipitation may have reduced the connectivity of this pore network even further.

CONCLUSIONS

An integrated petrographic and petrophysical analysis of Iowa PCC pavements was performed. Destructive and nondestructive methods were used to characterize the air void networks of PCC samples from both before and after air entrainment became a common practice.

The CT and helium analyses had good agreement with ASTM C457 image analysis on the total connected porosity for all pucks. However, the results of this study did not support the initial hypothesis that the deterioration of CA in pre-air-entrainment PCC was in some cases serving to create significant air void networks in these older pavements.

It was instead observed that the porosity of pavements showed strong correlation of decreasing porosity with increasing age. These results indicate that PCC porosity (i.e., the total percentage of air voids in a pavement) can be predicted from pavement age, at least in Iowa. Petrographic data suggest that this phenomenon is due to a reduction in pore space in the paste, with the reduction in paste porosity being more significant than the increase in porosity due to CA and fine aggregate deterioration.

The deterioration of fine aggregate and smaller CA creates pores that are largely similar in size and shape to pores created in more modern pavements through the use of air-entraining agents (though this study's CT and thin section images show that the entrained air void networks in the post-1950 samples have somewhat more regular pore shapes than pores formed due to deterioration in pre-1950 samples).

Unfortunately, the connectivity of both deteriorating coarse and fine aggregate pores and entrained air pores was not well imaged in core plugs CT-scanned at a higher resolution (35-µm voxels compared to 60-µm voxels). This voxel size (35 µm) was not sufficient to provide an adequate image of the pore network within the paste or to differentiate the paste from the fine aggregate.

Nonetheless, thin section images and mercury porosimetry enabled determination of the pore-throat size distribution to identify the paragenetic sequence of diagenetic events that these concretes have undergone during their service life. While the post-1950 pavements have smaller pore throats than the older pavement samples, the pores in the older samples are mostly connected through fractures and microporosity in the paste.

Connectivity in the post-1950 samples is visible at a larger scale (e.g., via the CT images of the plugs) where the pores created by deteriorating aggregate and entrained air connect through the paste. The trend of porosity decreasing with age can be explained by the multiscale air void network in the post-1950 samples that are connected through three pore types:

- Micropores and fractures in the paste
- Pores formed due to CA dissolution
- Intraparticle micropores formed due to fine aggregate dissolution

The trend of porosity decreasing with age likely also results from the pre-1950 samples showing mineral growth in the pores and reaction rims in the paste due to dissolution. These reaction rims may reduce the connectivity of the older samples and hence decrease their total connected porosity.

While a MATLAB script was used to extract these PCC samples' three main phases (coarse aggregate, paste, and pores) from their respective CT images, it was challenging to identify clear boundaries between the voxels pertaining to each phase (though the MATLAB code was also tested with the thin section images in order to customize the segmentation algorithms to these Iowa DOT sample types and workflows). The main issue with this study's PCC samples was the presence of voxel values that could belong to more than one phase. For example, fine aggregate can have the same voxel value as paste (indicated by the same grayscale value and the same color in the CT images).

Nonetheless, the CT images did show a clear trend across grain size and pore size distributions, where the CA size distribution coincides with the pore size distribution for all samples. Specifically, the most abundant pore sizes were formed due to the dissolution of FA and therefore their dominant sizes are similar to that of the FA grains.

The fact that these pavements have been in service for decades beyond their original design life cannot be disputed. This study shows the value of studying outliers for clues on how to design better pavements today. With the observation that some CA pebbles are currently undergoing dissolution or have completely dissolved away suggests another way of creating an air void network in concrete: the inclusion of dissolvable materials. The solubility of these materials can be tailored to specific design goals.

Future work should involve scanning-electron microscopy and geochemical analyses in order to identify the mineralogy of dissolution rims in pores and paste to track how they can change over time in ways that are not related to fracturing.

If the pore networks of PCC pavements mature over time, the authors propose that it is necessary to monitor this evolution by regular sampling and petrographic analysis of pavements. By better understanding the evolution of the air void network and coarse aggregates in PCC, Iowa DOT pavement engineers and materials geologists will be able to make more informed decisions when designing pavements to ensure maximum longevity and durability and thus reduce the life-cycle costs of pavements to Iowa taxpayers.

REFERENCES

ASCE. 2019. *First Concrete Pavement*. American Society for Civil Engineers website at: https://www.asce.org/project/first-concrete-pavement/.

Baughn, J. 2009. Drive on the Oldest Concrete Highway in Missouri. *Southeast Missourian*. https://www.semissourian.com/blogs/pavementends/entry/26736.

Blezard, R. G. 1984. A discussion of the paper "Examination of 136 Years Old Portland Cement Concrete" by G. M. Idorn and N. Thaulow. *Cement and Concrete Research,* Vol. 14, No. 1, pp. 154–156.

Boyle, R. 1662. A defence of the doctrine touching the spring and weight of the air, proposed by Mr. R. Boyle in his new physico-mechanical experiments; against the objections of Franciscvs Linvs. Wherewith the objector's funicular hypothesis is also examined. Thomas Robinson Bookseller, London.

Choi, S. H. and A. M. M. Chan. 2004. A Virtual Prototyping System for Rapid Product Development. *Computer-Aided Design,* Vol. 36, No. 5, pp. 401–412.

Davenport, B., G. Voigt, and P. Deem. 2014. *A Concrete Legacy: The Past, Present, and Future of the American Concrete Pavement Association*. American Concrete Pavement Association, Rosemont, Illinois.

Gilles, P. and A. Jasienski. 2006. A Second Youth for an Old Lady of 78: The Rehabilitation of the Lorraine Avenue in Brussels - Belgium. In *A Glance at the Belgian Experience in Concrete Pavements*, pp. 22–37.

Gonnerman, H. F. 1944. Tests of Concrete Containing Air-Entraining Portland Cements or Air-Entraining Materials Added to Batch at Mixer. *International Concrete Abstracts,* Vol. 40, pp. 477–508.

Hanson, T. D. 2007. *Air Content and Permeability of PCC Pavements: 1909 to 2006*. Iowa Department of Transportation, Ames, Iowa. Available at: http://publications.iowa.gov/19909/1/IADOT_mlr_05_02_Air_Content_Permeability_PCC_Pavements_2007.pdf.

Hanson, T. D. 2009. *100 Years of Concrete Pavements in Iowa*. Iowa Department of Transportation, Ames, Iowa. Available at: http://publications.iowa.gov/9446/1/MLR-07-01.pdf.

Hearn, N. and R. D. Hooton. 1992. Sample Mass and Dimension Effects on Mercury Intrusion Porosimetry Results. *Cement and Concrete Research,* Vol. 22, No. 5, pp. 970–980.

Hedenblad, G. 1997. The Use of Mercury Intrusion Porosimetry or Helium Porosity to Predict the Moisture Transport Properties of Hardened Cement Paste. *Advanced Cement Based Materials,* Vol. 6, No. 3–4, pp. 123–129.

Hellebois, A., A. Launoy, C. Pierre, M. De Lanève, and B. Espion. 2013. 100-Year-Old Hennebique Concrete, from Composition to Performance. *Construction and Building Materials,* Vol. 44, pp. 149–160.

Hoffbeck, S. R. 1990. Granitoid Pavement in Grand Forks, North Dakota. Public Hearing on the Nomination of Granitoid Streets in Grand Forks to the National Register of Historic Places.

Holden, J. W., A. Marston, H. C. Beard, and T. H. MacDonald. 1915. *State of Iowa 1915: Report of the State Highway Commission for the Year Ended December 1, 1915*. State Highway Commission, Ames, Iowa. Available at: https://babel.hathitrust.org/cgi/pt?id=chi.100923869&view=1up&seq=12.

Holden, J. W., A. Marston, H. C. Beard, and T. H. MacDonald. 1916. *State of Iowa 1916: Report of the State Highway Commission for the Year Ended December 1, 1916*. State Highway Commission, Ames, Iowa. Available at: https://babel.hathitrust.org/cgi/pt?id=njp.32101051127460&view=1up&seq=3.

Idorn, G. M., and N. Thaulow. 1983. Examination of 136 Years Old Portland Cement Concrete. *Cement and Concrete Research*, Vol. 13, No. 5, pp. 739–743.

Kim, K. Y., T. S. Yun, J. Choo, D. H. Kang, and H. S. Shin. 2012. Determination of Air-Void Parameters of Hardened Cement-Based Materials using X-Ray Computed Tomography. *Construction and Building Materials*, Vol. 37, pp. 93–101.

Kneer, A. 2012. Duluth's Granitoid Roads Inspired Memorial Park. *The Statesman*. http://www.theumdstatesman.com/blog/2012/10/16/duluths-granitoid-roads-inspired-memorial-park.

Koster, G. E. 1997. *A Story of Highway Development in Nebraska*. Nebraska Department of Roads, Lincoln, Nebraska. Available at: https://dot.nebraska.gov/media/1205/history-general.pdf.

Mailloux, L., K. Peterson, T. Van Dam, and K. Ellis. 2008. Lessons from Michigan's Oldest Concrete Pavement – Still Serving After 100 Years. *Proceedings of the Ninth International Conference on Concrete Pavements: The Golden Gate to Tomorrow's Concrete Pavements*, pp. 346–363.

Nebraska Concrete Paving Association. 2019. *Historic Pavements*. http://www.nebrconc.org/historic-photos/.

Obla, K. H. 2015. *Improving Concrete Quality*. CRC Press for National Ready Mixed Concrete Association, Silver Spring, Maryland.

Poole, A. B. and I. Sims. 2016. *Concrete Petrography: A Handbook of Investigative Techniques*, Second Edition. CRC Press, Taylor & Francis Group, Boca Raton, Florida.

Powers, T. C. 1954. Void Space as a Basis for Producing Air-Entrained Concrete. *International Concrete Abstracts*, Vol. 50, No. 5, pp. 741–760.

Prusinski, J. R. and D. Taubert. 2013. *Narrative History of Belknap Place Oldest Existing Concrete Road in Texas (1914), San Antonio, Texas*. State of Texas application to install historic marker. Available at: http://www.cementx.org/uploads/9/4/3/8/94386531/narrative_history_of_belknap_place__r_11-14-13_.pdf.

Rayment, D. L. 1986. The Electron Microprobe Analysis of the C-S-H Phases in a 136 Year Old Cement Paste. *Cement and Concrete Research*, Vol. 16, No. 3, pp. 341–344.

Snell, L. M. and B. G. Snell. 2002. Oldest Concrete Street in the United States. *Concrete International*, Vol. 24, No. 3, pp. 72–74.

Torrans, P. H. and D. L. Ivey. 1968. *Review of Literature on Air Entrained Concrete*. Texas Transportation Institute, Texas A&M University, College Station, Texas.

Vitton, S. J., M. A. Lehman, and T. J. Van Dam. 1999. Automated Soil Particle Specific Gravity Analysis Using Bulk Flow and Helium Pycnometry. In *Nondestructive and Automated Testing for Soil and Rock Properties*. ASTM International, West Conshohocken, Pennsylvania, pp. 3–13.

Wong, R. C. K. and K. T. Chau. 2005. Estimation of Air Void and Aggregate Spatial Distributions in Concrete under Uniaxial Compression using Computer Tomography Scanning. *Cement and Concrete Research*, Vol. 35, No. 8, pp. 1566–1576.

Yun, T. S., K. Y. Kim, J. Choo, and D. H. Kang. 2012. Quantifying the Distribution of Paste-Void Spacing of Hardened Cement Paste using X-Ray Computed Tomography. *Materials Characterization,* Vol. 73, pp. 137–143.

THE INSTITUTE FOR TRANSPORTATION IS THE FOCAL POINT FOR TRANSPORTATION AT IOWA STATE UNIVERSITY.

InTrans centers and programs perform transportation research and provide technology transfer services for government agencies and private companies;

InTrans contributes to Iowa State University and the College of Engineering's educational programs for transportation students and provides K–12 outreach; and

InTrans conducts local, regional, and national transportation services and continuing education programs.

IOWA STATE UNIVERSITY

Visit **InTrans.iastate.edu** for color pdfs of this and other research reports.